



# **An Atom Interferometer for Measuring Horizontal Accelerations**

Jimmy Stammers  
Department of Physics

A thesis submitted to Imperial College London for partial fulfillment of the  
requirements for the degree of Doctor of Philosophy

## Abstract

Matter-wave interferometry has enabled high precision measurements of inertial forces such as gravity and the Coriolis force. This is facilitated by the long-term stability of the physical properties of atoms and lasers. Recent experiments have demonstrated the operation of portable, robust sensors using atom interferometry. This has potential uses in the context of inertial navigation, where conventional devices suffer from long-term drifts due to bias instability. Furthermore, determining position via dead reckoning requires minimisation of dead time between measurements. This thesis presents the development of an atom interferometer for measuring horizontal accelerations. In this configuration, gravity induces motion across the laser wavefront, which constrains the tolerable level of wavefront distortions. Effective control of the experiment allows the interferometer to be operated at a rate of 4 Hz. A cold ensemble of  $10^6$  atoms in the same internal state is prepared in 150 ms. The interferometer operates using a sequence of three laser pulses separated by  $T = 25$  ms to achieve sensitivity to horizontal accelerations. Combining this with a classical accelerometer provides a method of correcting for vibration-induced noise, as well as determining the interferometer fringe order. After an integration time of 70 s, the sensitivity to horizontal accelerations is better than  $1 \times 10^{-6} \text{ m s}^{-2}$ . Effects which limit this sensitivity are discussed.

## Declaration

I declare that this thesis is the result of my own work. All sources used for this work have been clearly referenced in accordance with the departmental requirements.

Jimmy Stammers

The copyright of this thesis rests with the author and is made available under a Creative Commons Attribution Non-Commercial No Derivatives licence. Researchers are free to copy, distribute or transmit the thesis on the condition that they attribute it, that they do not use it for commercial purposes and that they do not alter, transform or build upon it. For any reuse or redistribution, researchers must make clear to others the licence terms of this work.

## Acknowledgements

There are many people to whom I owe a great deal of thanks.

## Preface

This thesis describes my research on various aspects of...

# Contents

<b>List of figures</b>	<b>xi</b>
<b>List of tables</b>	<b>xv</b>
<b>1. Introduction</b>	<b>1</b>
1.1. Light-Pulse Atom Interferometry . . . . .	1
1.2. Application to Inertial Navigation . . . . .	2
1.3. Aims . . . . .	3
1.4. Structure of this Thesis . . . . .	4
<b>2. Theory</b>	<b>5</b>
2.1. Chapter Overview . . . . .	5
2.2. Light-Pulse Matter-Wave Interference . . . . .	6
2.2.1. The Mach-Zehnder Scheme . . . . .	6
2.2.2. Phase Shift Contributions . . . . .	8
2.3. Raman Transitions in Rubidium-87 . . . . .	12
2.3.1. State Propagation . . . . .	14
2.3.2. Application to a Sequence of Raman Pulses . . . . .	15
2.3.3. Extending to a Real Atomic System . . . . .	17
2.4. Applications to Rubidium-87 . . . . .	17
2.4.1. Atomic Structure . . . . .	18
2.4.2. Driving Raman Transitions . . . . .	20
2.4.3. The Double Interferometer . . . . .	21
2.5. note on units . . . . .	23
2.6. Conclusion . . . . .	23
<b>3. MOTMaster</b>	<b>24</b>
3.1. Chapter Overview . . . . .	24
3.2. Motivation . . . . .	25

3.3.	Interfacing with Hardware . . . . .	26
3.3.1.	Hardware Abstraction . . . . .	27
3.3.2.	Voltage Pattern Generation . . . . .	28
3.3.3.	Timed Serial Communication . . . . .	29
3.3.4.	Voltage Acquisition . . . . .	30
3.4.	MOTMaster Sequences . . . . .	30
3.4.1.	Sequence Structure . . . . .	31
3.4.2.	Running a Sequence . . . . .	32
3.5.	Experiment Control Hardware . . . . .	34
3.6.	Experimental Sequence Overview . . . . .	35
<b>4.</b>	<b>Cooling and Trapping in a MOT</b>	<b>37</b>
4.1.	Chapter Overview . . . . .	37
4.2.	The Navigator Vacuum Chamber . . . . .	37
4.2.1.	The 2D MOT system . . . . .	40
4.2.2.	The 3D MOT system . . . . .	44
4.2.3.	CCD Imaging . . . . .	47
4.3.	Generating MOT light . . . . .	49
4.3.1.	Absolute Frequency Reference . . . . .	50
4.3.2.	Cooling and Repump Light . . . . .	53
4.3.3.	Real-Time Control . . . . .	55
4.4.	Controlling the MOTs . . . . .	55
4.4.1.	Optical Fibre Network . . . . .	56
4.4.2.	Magnetic Field Control . . . . .	56
4.5.	Characterising the MOTs . . . . .	58
4.5.1.	3D MOT Loading Rate . . . . .	60
4.6.	Conclusion . . . . .	62
<b>5.</b>	<b>Preparing Atoms for Interferometry</b>	<b>64</b>
5.1.	Chapter Overview . . . . .	64
5.2.	Cooling in Optical Molasses . . . . .	65
5.2.1.	Motivation for Launching . . . . .	65
5.2.2.	Frequency and Power Control . . . . .	66
5.2.3.	Launching in a Moving Molasses . . . . .	66
5.2.4.	Imaging the Atom Cloud over Time . . . . .	69
5.3.	State Preparation . . . . .	74
5.3.1.	Schemes for Preparation . . . . .	74

5.3.2. Optically Pumping the Atoms . . . . .	77
5.3.3. Including Microwave Transitions . . . . .	80
5.3.4. Blow-Away . . . . .	83
5.4. Conclusion . . . . .	83
<b>6. Raman Optical System</b>	<b>84</b>
6.1. Chapter Outline . . . . .	84
6.2. Wavefront Requirements . . . . .	84
6.2.1. Gradients of Intensity . . . . .	85
6.2.2. Wavefront Distortions . . . . .	86
6.3. Collimation Optics . . . . .	89
6.3.1. Component Overview . . . . .	89
6.3.2. Alignment and Collimation . . . . .	90
6.3.3. Measuring the Beam Width . . . . .	93
6.4. Retro-Reflection Assembly . . . . .	94
6.4.1. In-Situ Alignment and Optimisation . . . . .	96
6.4.2. The Mechanical Accelerometer . . . . .	99
6.5. Conclusion . . . . .	100
<b>7. Acceleration-Sensitive Interference</b>	<b>101</b>
7.1. Chapter Outline . . . . .	101
7.2. The M-Squared Laser System . . . . .	102
7.2.1. Laser System Overview . . . . .	102
7.2.2. Frequency and Phase Control . . . . .	104
7.2.3. The DCS Module . . . . .	104
7.3. Atom Detection . . . . .	105
7.3.1. Optical Setup . . . . .	106
7.3.2. Detection using $\sigma^+$ transitions . . . . .	107
7.3.3. Measuring the Occupation Probability . . . . .	112
7.4. Individual Pulse Characterisation . . . . .	115
7.4.1. Raman Transition Spectrum . . . . .	116
7.4.2. Cancelling the Differential ac Stark Shift . . . . .	118
7.4.3. Velocity-Selective Pulse . . . . .	121
7.4.4. Interferometer Pulses . . . . .	123
7.5. Sensitivity . . . . .	125
7.5.1. The Allan Variance . . . . .	125
7.5.2. Sources of Noise . . . . .	127

---

7.5.3. Detection Noise . . . . .	127
7.5.4. The Sensitivity Function . . . . .	130
7.5.5. Influence of Laser Phase Noise . . . . .	132
7.5.6. Vibrations . . . . .	135
7.6. Measuring Accelerations . . . . .	137
7.6.1. Fringe Calibration . . . . .	138
7.6.2. Correcting for Vibration Noise . . . . .	139
7.6.3. Signal Stability . . . . .	141
7.7. Conclusion . . . . .	143
<b>8. Outlook</b>	<b>144</b>
8.1. Conclusions . . . . .	144
8.2. Avenues of Further Research . . . . .	146
8.3. Concluding Remarks . . . . .	147
<b>A. <math>\mu</math>Quans Laser Serial Commands</b>	<b>149</b>
<b>Bibliography</b>	<b>151</b>
<b>Acronyms</b>	<b>161</b>

# List of figures

2.1. Mach-Zehnder atom interferometer configuration.	7
2.2. Interferometer paths under constant acceleration	10
2.3. Schematic diagram of a raman transition.	13
2.4. Rubidium-87 D2 transition hyperfine structure.	19
2.5. Raman beam configuration.	22
2.6. Interferometer paths with two oppositely directed Raman transitions.	22
3.1. Schematic diagram of MOTMaster and hardware interface.	26
3.2. Scripted pattern generation for an NI-HSDIO card	29
3.3. Timing diagram for serial communication	30
3.4. MOTMaster user interface	33
3.5. Control hardware schematic diagram	36
4.1. Magneto-optical Trap (MOT) system component diagram	39
4.2. Schematic for the 2D MOT	41
4.3. Optical components for the 2D MOT	42
4.4. Simulated field and field gradients for the 2D MOT quadrupole coils	43
4.5. MOT coil temperature rise	45
4.6. Measured magnetic field and field gradient for the 3D MOT coils	45
4.7. Simulated magnetic field for the 3D MOT quadrupole coils	46

4.8. Optical setup for CCD imaging . . . . .	47
4.9. Integrated pixel counts as a function of CCD exposure time. . . . .	49
4.10. $\mu$ Quans Laser System Diagram . . . . .	51
4.11. Saturated absorption spectroscopy of the Muquans master laser. . . . .	52
4.12. Error Signal for the $\mu$ Quans master servo. . . . .	52
4.13. Error Signal for the $\mu$ Quans Cooling laser. . . . .	53
4.14. Cooling power vs. Acousto-optic Modulator (AOM) control voltage. .	54
4.15. Network of optical fibre splitters and AOMs for MOTlight distribution	57
4.16. MOT loading timing diagram. . . . .	60
4.17. 3D MOT atom number vs dispenser current with and without a push beam. . . . .	63
5.1. Molasses stage timing diagram . . . . .	67
5.2. Beam configuration for a moving molasses . . . . .	68
5.3. Atom cloud position after launching in a moving molasses . . . . .	69
5.4. Integrated pixel counts during ballistic expansion. . . . .	71
5.5. Temperature measurement using ballistic expansion . . . . .	72
5.6. Atom cloud centre-of-mass over time . . . . .	73
5.7. State preparation pulse sequence . . . . .	76
5.8. State selection timing schematic . . . . .	76
5.9. Ground state distribution during $ F = 2\rangle \rightarrow  F' = 2\rangle$ pumping . . . . .	78
5.10. $m_F$ populations before and after $ F = 1\rangle \rightarrow  F' = 0\rangle$ pumping . . . . .	79
5.11. $ 1, m_F\rangle$ populations for increasing $ F = 1\rangle \rightarrow  F' = 0\rangle$ pumping time. . . . .	80
5.12. Setup for Microwaves . . . . .	81
5.13. Microwave Rabi oscillation between $ 1, 0\rangle$ and $ 2, 0\rangle$ . . . . .	82
5.14. Microwave transition spectrum . . . . .	82

6.1. Simulated fringe contrast vs beam waist size . . . . .	87
6.2. Expected fringe contrast as a function of random phase contributions.	88
6.3. Drawings of the components used in the Raman optics assemblies . . . . .	91
6.4. Simulated wavefront distortion for longitudinal and transverse fibre misalignment . . . . .	92
6.5. Measured Raman beam waist . . . . .	94
6.6. Quarter-wave plate thickness variation. . . . .	95
6.7. Automatic mirror alignment using the Nelder-Mead simplex algorithm.	98
6.8. Innalabs accelerometer cross-section . . . . .	100
7.1. M-Squared Laser System Schematic . . . . .	103
7.2. DCS Module User interface . . . . .	105
7.3. Optical setup for Photodiode Detection . . . . .	106
7.4. Scheme to invert beam polarisation. . . . .	108
7.5. State detection sequence timing . . . . .	109
7.6. Photodiode output voltage for increasing detection beam intensity. . .	111
7.7. Photodiode voltage for varying detection times. . . . .	112
7.8. Interferometer contrast for an increasing residual atoms ratio . . . . .	115
7.9. Raman transition spectrum . . . . .	117
7.10. $\Delta m = 0$ transition spectrum. . . . .	118
7.11. Differential ac Stark shift as a function of two-photon detuning and Raman beam intensities. . . . .	120
7.12. Raman transition spectrum after cancelling the differential ac Stark shift.	121
7.13. Simulated velocity distribution after a Raman $\pi$ pulse. . . . .	123
7.14. $ F = 2\rangle$ population after a velocity-selective Raman $\pi$ pulse. . . . .	124
7.15. Rabi oscillations between the $ 1, 0\rangle$ and $ 2, 0\rangle$ states. . . . .	125

7.16. Photodiode power spectral density . . . . .	130
7.17. Allan variance of the Photodiode voltage. . . . .	131
7.18. Transfer function for laser phase noise. . . . .	134
7.19. Allan deviation of the Raman laser phase difference. . . . .	135
7.20. Acceleration noise transfer function. . . . .	137
7.21. Acceleration noise power spectral density. . . . .	138
7.22. Interference fringe for $T = 25$ ms. . . . .	139
7.23. Comparison of MEMS/Interferometer correlation in a high and low vibration environments. . . . .	141
7.24. Histogram of acceleration noise. . . . .	142
7.25. Comparison of Allan deviation in a high and low vibration environment.	143

# List of tables

4.1. Table of parameters for each 3D MOT bias coil. . . . .	47
4.2. Typical optical and magnetic parameters for the Magneto-optical Traps (MOTs). . . . .	59
7.1. Raman transition polarisation configurations . . . . .	117
7.2. Allowed polarisation configurations between each hyperfine ground state Zeeman sub-levels. . . . .	117
7.3. Comparison of known noise sources. . . . .	127

*“I may not have gone where I intended to go, but I think I have ended up where I needed to be”*

— Douglas Adams



# **Chapter 1.**

## **Introduction**

### **1.1. Light-Pulse Atom Interferometry**

The development of quantum theory to explain the wave-like behaviour of matter has enabled significant advances in science and technology. An early example of this is the atomic clock [1], which makes use of the interference between two atomic internal states to precisely measure their transition frequency. This technology has led to a re-definition of the second in terms of physical constants, as well as a globally-adopted standard for timekeeping [2] that supports many aspects of modern society. Early interferometers relied on driving microwave frequency transitions because the contemporary laser technology did not have the frequency stability or linewidths necessary to maintain coherence between the atomic states. It was later suggested by Christian Bordé [3] that using the larger momentum recoil of optical frequency transitions would enable measurements of rotation or acceleration using the resulting phase shift between the two paths of the interferometer.

Kasevich and Chu demonstrated inertial force sensing using atom interferometry with a measurement of gravitational acceleration [4, 5]. Subsequent work showed that atom interferometers were also able to measure rotations [6]. As inertial sensors, these experiments showed comparable short-term sensitivities to their classical counterparts. By contrast, their long-term stability was noteworthy. This is due to the frequency-stability of the atomic transition and in the lasers used to stimulate it. Again, this is analogous to atomic clock systems which are able to reach very low fractional uncertainties by integrating over long timescales.

## 1.2. Application to Inertial Navigation

This long-term stability is of great practical interest for inertial navigation systems. These are systems which measure the position of a moving body using successive measurements of its acceleration and rotation, known as dead reckoning. The accuracy of this method depends on the intrinsic noise of each sensor, as well as their bias. If the noise is known *a priori*, then a statistical method such as a Kalman filter [7] can be used to produce a more accurate estimate of the position. However, the error from a bias tends to dominate over long timescales. For instance, the position error from a constant acceleration bias grows quadratically with time. This problem is compounded by the fact that the bias in an inertial sensor drifts over time due to physical effects such as temperature variation and mechanical strain. This bias instability means that inertial navigation systems require regular re-calibration and an external method of correcting for the position error such as Global Navigation Satellite System (**GNSS**).

One drawback of atom interferometers is the interrogation time needed between each laser pulse. This leads to a sensitivity bandwidth of the order of 10 Hz. It should be noted that acceleration bandwidths as high as 60 Hz [8] and even 10 kHz [9]

using short, high-power pulses have been reported, but these are at the cost of a reduction in sensitivity. A further issue is the measurement dead time as a result of the time required to prepare a cold ensemble of atoms. During this preparation time, the system does not respond to any acceleration or rotation acting on the atoms. It has been suggested that this shortcoming can be counteracted using a conventional mechanical accelerometer [10] or by interleaving multiple cold atom interferometers. The latter of these has been recently demonstrated in a gyroscope [11].

Hybridising an atom interferometer with a classical sensor results in a composite system which aims for both long-term stability and high bandwidth. Indeed, a secondary measurement is needed to determine the interferometer fringe order and hence obtain an absolute value of acceleration. This is of particular importance for inertial navigation, where the range of acceleration is far greater than the fringe period [12]. This auxillary sensor can also improve the sensitivity of the interferometer in high vibration environments [13], which is a significant source of phase noise. Measuring these vibrations provides a method of filtering their effect from the interferometer signal.

### 1.3. Aims

This aim of this project was to investigate the use of atom interferometry in the context of inertial navigation by measuring horizontal accelerations. Gravitational acceleration induces motion transverse to the laser wavefront. Together with the requirements of high acceleration sensitivity and minimal dead-time, this influenced the technical aspects of this experiment.

## 1.4. Structure of this Thesis

This thesis is structured as follows:

- **Chapter 2** presents a theoretical introduction to matter-wave interferometry and the relevant atomic structure of Rubidium-87.
- **Chapter 3** describes the software used to control the experiment and acquire data.
- **Chapter 4** outlines the preliminary cooling and trapping of Rubidium-87 in a **MOT**.
- **Chapter 5** discusses the techniques used to further cool the atoms and prepare an ensemble in the same internal state,
- **Chapter 6** gives a detailed description of the in-vacuum optical system for driving Raman transitions.
- **Chapter 7** characterises the interferometer's sensitivity to accelerations.
- **Chapter 8** summarises the conclusions of this thesis and outlines further work towards improving the experiment

# **Chapter 2.**

## **Theory**

### **2.1. Chapter Overview**

This chapter presents a theoretical discussion of the interaction between light and matter that forms the basis of atom interferometry. It begins with a review of the theory of matter-wave interference and its application to measuring inertial forces such as accelerations in Section 2.2. This is followed by a derivation of the equations of motion for a Raman transition in a simplified three-level atom in Section 2.3. Finally, this chapter concludes with a discussion of the atomic structure of Rubidium-87 ( $^{87}\text{Rb}$ ), focusing on the aspects relevant to the previously mentioned phenomena.

This chapter assumes some prior understanding of light-matter interactions on the part of the reader. A comprehensive description of the semi-classical approximation to atom-light interactions can be found in [14]. Theories on laser cooling and magneto-optical trapping are of interest to some experimental aspects of these thesis. Details of these can be found in [15]. For an exact derivation of the two-level approximation to the Raman transition, the reader is referred to [16].

## 2.2. Light-Pulse Matter-Wave Interference

A cornerstone of quantum mechanics is the wave-like evolution of quantum states as described by the Schrödinger equation. As a consequence of this, it is possible to create superpositions of states that evolve coherently. Furthermore, these states can interfere with each other if their wavefunctions overlap. The interference pattern, which depends on the difference in phase between the two paths.

In this section, the theory of matter-wave interference using pulses of laser light is presented. It begins with a description of the  $\pi/2 - \pi - \pi/2$  pulse sequence that forms an analogue of the Mach-Zehnder interferometer in Section 2.2.1. This is followed by a derivation of the interferometer phase in Section 2.2.2. In particular, it is shown that this depends upon the acceleration of the atom during the interferometer.

### 2.2.1. The Mach-Zehnder Scheme

One method for realising matter-wave interference is the Ramsey-Bordé interferometer. This requires an ensemble of atoms that can be driven between two states using an interaction with a laser field. The absorption and stimulated emission of photons exchanges momentum between the atom and the light such that the state of the atom is defined as a product of its internal states and momentum eigenstates, labelled as  $|1, \mathbf{p}\rangle$  and  $|2, \mathbf{p} + \hbar\mathbf{k}\rangle$ . When compared with conventional optical interferometry, it is the light which alters the trajectory of the matter, rather than the other way around. Indeed, laser pulses with pulse areas of  $\pi/2$  and  $\pi$  are analogous to beam-splitters and mirrors in optical systems.

A three pulse interferometer is the simplest configuration for which the two trajectories can overlap after separation. Schematically, this is shown in Figure 2.1. An atom in

$|1, \mathbf{p}\rangle$  is driven into a superposition of two states using a  $\pi/2$  pulse. The wavepacket in  $|2, \mathbf{p} + \hbar\mathbf{k}\rangle$  has a different momentum, so the two become spatially separated. After a time  $T$ , a  $\pi$  pulse inverts the state along each path, so that after another duration of  $T$  the two wavepackets overlap. These are recombined by a final  $\pi/2$  pulse. The interference between the two states is manifested in their population, which depends on the phase difference between the two paths. This phase difference  $\Delta\Phi$  is expressed as follows

$$\Delta\Phi = \Delta\Phi_{\text{prop}} + \Delta\Phi_{\text{int}} + \Delta\Phi_{\text{laser}} \quad (2.1)$$

where  $\Delta\Phi_{\text{prop}}$  is the phase difference due to propagation along each path,  $\Delta\Phi_{\text{int}}$  is the phase difference due to evolution of the internal state and  $\Delta\Phi_{\text{laser}}$  is the phase difference caused by interactions with the laser field.

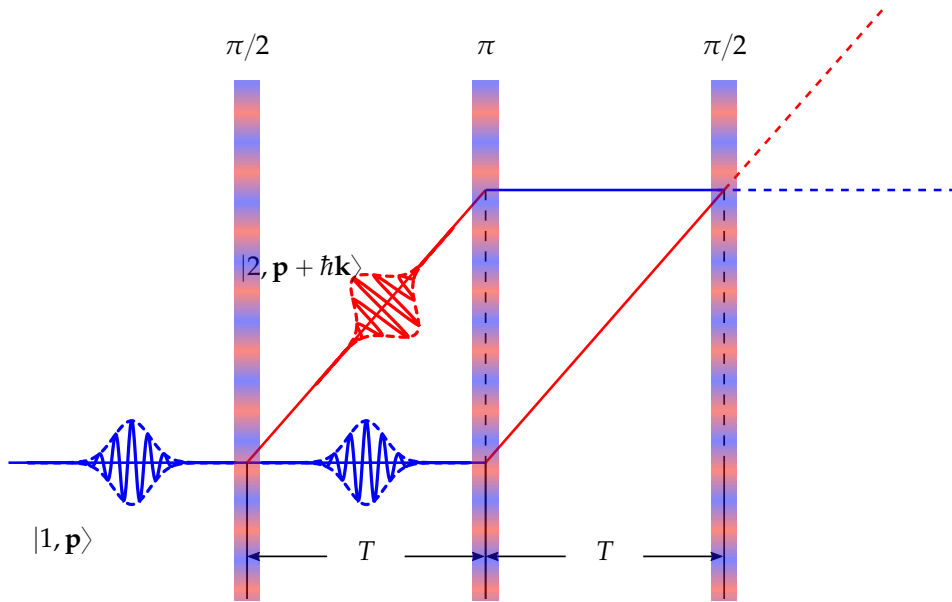


**Figure 2.1.:** Mach-Zehnder atom interferometer configuration. A sequence of laser pulses are used to drive an atom into a superposition of two states. When the two paths overlap at the final  $\pi/2$  pulse, they interfere with each other. The final occupation probability is proportional to the phase difference between the two paths.

### 2.2.2. Phase Shift Contributions

#### Propagation Phase

The propagation phase can be evaluated using the path integral approach to quantum mechanics. The trajectory of a quantum state is obtained by integrating over all possible paths. The total amplitude for arriving at position  $x_b$  at  $t_b$ , starting from  $x_a$  at  $t_a$  is given by the following propagator

$$K(t_b, x_b, t_a, x_a) = \int_{x_a}^{x_b} e^{iS/\hbar} dx(t) \quad (2.2)$$

where  $x_b \equiv x(t_b)$  and similarly for  $x_a$ . The action  $S$  along a path is defined using the Lagrangian of the system

$$S = \int_{t_a}^{t_b} L(x, \dot{x}) dt \quad (2.3)$$

and the classical limit is recovered when the action  $S_{\text{cl}} \gg \hbar$ . In this case, most paths destructively interfere as their phases oscillate rapidly. Along the classical path, the action is minimised. Paths close to this lead to constructive interference, so the trajectory of the system is well-described using the Euler-Lagrange equations. Under this condition, it can be shown [17] that for a plane wave, the propagation phase is proportional to the action along the classical path

$$\Delta\Phi_{\text{prop}} = \frac{i}{\hbar} S_{\text{cl}}(t_b, x_b, t_a, x_a) \quad (2.4)$$

This is indeed the case for an atom interferometer. When considering a single atom under a constant acceleration, the Lagrangian is given by

$$L = \frac{1}{2}m\dot{x}^2 + max \quad (2.5)$$

so that its position and velocity are given by

$$x(t) = x_a + v_a(t - t_a) + \frac{1}{2}a(t - t_a)^2 \quad (2.6a)$$

$$v(t) = v_a + a(t - t_a) \quad (2.6b)$$

for initial values of position ( $x_a$ ), velocity ( $v_a$ ) and time ( $t_a$ ). Using equation (2.3), the action is given by

$$S(t_b, x_b, t_a, x_a) = \frac{m(x_b - x_a)^2}{2(t_b - t_a)} + \frac{ma(x_b + x_a)(t_b - t_a)}{2} - \frac{ma^2(t_b - t_a)^3}{24} \quad (2.7)$$

The trajectories along each interferometer path under acceleration is shown in Figure 2.2. Denoting  $S_{ac} \equiv S(T, x_c, 0, x_a)$  and likewise for the other co-ordinates, the difference in the action along the upper and lower paths is

$$\begin{aligned} S_{ac} + S_{cd} - (S_{ab} + S_{bd}) &= -\frac{m(x_b - x_c)(aT^2 - x_a + x_b + x_c - x_d)}{T} \\ &= -\frac{m(x'_b - x'_c)((x'_c - x'_a) + (x'_d - x'_b))}{T} \end{aligned} \quad (2.8)$$

where the second expression is obtained using  $x_b - x'_b = x_c - x'_c = \frac{1}{2}aT^2$  and  $x_d - x'_d = 2aT^2$ . When there is zero acceleration, the area enclosed by the interferometer forms a parallelogram and the action along each path is equal. It follows from equation (2.4) that  $\Delta\Phi_{\text{prop}} = 0$  when there is a constant acceleration of the atom.

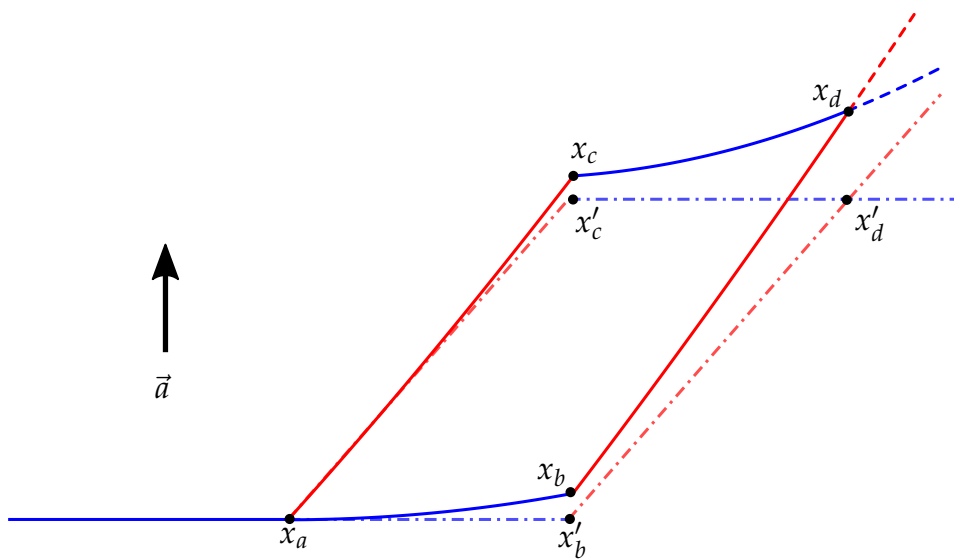


**Figure 2.2.:** Interferometer paths under a constant acceleration. The dashed lines indicate the trajectories under zero acceleration.

### Internal State Evolution

Between each laser pulse, the atom evolves freely. Therefore, the phase due to this evolution is given by

$$\phi^{(j)}(t_a, t_b) = \int_{t_a}^{t_b} i\omega_j t \, dt \quad (2.9)$$

where  $\omega_j$  depends on the state of the atom along that trajectory. The phase difference due to the internal state evolution is

$$\Delta\Phi_{\text{int}} = \phi^{(2)}(t_1, t_2) + \phi^{(1)}(t_2, t_3) - (\phi^{(1)}(t_1, t_2) + \phi^{(2)}(t_2, t_3)) \quad (2.10)$$

which is zero if the time between successive pulses is the same and the energy of each state does not vary. The latter case is important when considering the effects of the ac Stark shift and is addressed subsequently in Section 7.4.2.

## Laser Phase

Finally, there is the contribution from the laser phase. During each transition, the phase of the laser modifies the state of the atom. The propagator that describes this transition for arbitrary Rabi frequencies and detuning is derived below, in Section 2.3. For now, it is sufficient to focus on the ideal case of perfect pulse areas and zero detuning. The laser interaction modifies the two states as follows

$$U_L(\phi) |1\rangle = e^{-i\phi} |2\rangle \quad (2.11a)$$

$$U_L(\phi) |2\rangle = e^{i\phi} |1\rangle \quad (2.11b)$$

where  $\phi = \mathbf{k} \cdot \mathbf{x} - \omega_L t + \phi_j$  is the phase of the light driving the transition. If the time between each pulse is constant the  $\omega_L t$  term can be omitted, so that the phase of the atom along each path depends on its position and the phase of the laser. If the acceleration is along the same axis as the light's wavevector ( $\mathbf{k} \cdot \mathbf{x} \equiv kx$ ), the phase along the upper and lower paths are

$$\phi_l = i(kx_b + \phi_2) \quad (2.12a)$$

$$\phi_u = i(k(x_a - x_c + x_d) + \phi_1 - \phi_2 + \phi_3) \quad (2.12b)$$

Following the same argument used in equation (2.8), this can be simplified so that the phase difference due to the laser interaction ( $\phi_u - \phi_l$ ), and hence the total phase difference, is

$$\Delta\Phi = \Delta\Phi_{\text{laser}} = \mathbf{k} \cdot \mathbf{a} T^2 + \phi_1 - 2\phi_2 + \phi_3 \quad (2.13)$$

## 2.3. Raman Transitions in Rubidium-87

In this section, an analysis of the dynamics of the stimulated Raman transition is presented. This is modeled as an effective transition between two ground states  $|1\rangle$  and  $|2\rangle$ . These two states are coupled via an intermediate state  $|i\rangle$  which can be adiabatically eliminated when the two light fields are sufficiently detuned from resonance. An explicit derivation of this process can be found elsewhere [18, 19]. The key results, which aid the discussion of the performance of the interferometer in subsequent chapters, are summarised below. Following this, a propagator is derived which describes the evolution of the atomic state during a Raman transition. This is used to derive the final state after the interferometer pulse sequence. Modeling the atomic system in this way makes it possible to consider the effects of finite pulse duration, detuning and intensity on the final state.

The energy level scheme for a Raman transition is shown in Figure 2.3. Each ground state is coupled to the intermediate state  $|i\rangle$  by an interaction with an electric field  $\mathbf{E}_j = \mathbf{E}_{0,j} \cos(\omega_j^l t - \mathbf{k}_j \cdot \mathbf{x} + \phi_j)$ . The strength of this interaction is defined by the Rabi frequency

$$\Omega_j = \frac{1}{\hbar} \langle j | -\mathbf{d} \cdot \mathbf{E}_{0,j} | i \rangle e^{i\phi_j} \quad (2.14)$$

where  $\mathbf{d}$  is the dipole operator. The frequency of each field is detuned from resonance to give a two-photon detuning  $\Delta$ . It is assumed that the hyperfine splitting  $\omega_{\text{hfs}}$  is much larger than this, so that each field only drives transitions from one of the ground states. When  $\Delta$  is sufficiently larger than the natural transition linewidth, the population of the intermediate state remains constant and can be adiabatically eliminated. The interference of the two fields means that the transition can be represented by an

interaction with an effective field with the following parameters

$$\omega_{\text{eff}} = \omega_1^l - \omega_l^2 \quad (2.15a)$$

$$\phi_{\text{eff}} = \phi_1 - \phi_2 \quad (2.15b)$$

$$\mathbf{k}_{\text{eff}} = \mathbf{k}_1 - \mathbf{k}_2 \quad (2.15c)$$

$\approx 2\mathbf{k}_1$  (when counter-propagating)

The resonance condition for the Raman transition is given by

$$\delta = \omega_{\text{eff}} - \left[ \omega_{\text{hfs}} + \mathbf{k}_{\text{eff}} \cdot \mathbf{v} + \frac{\hbar |\mathbf{k}_{\text{eff}}|^2}{2m} \right] \quad (2.16)$$

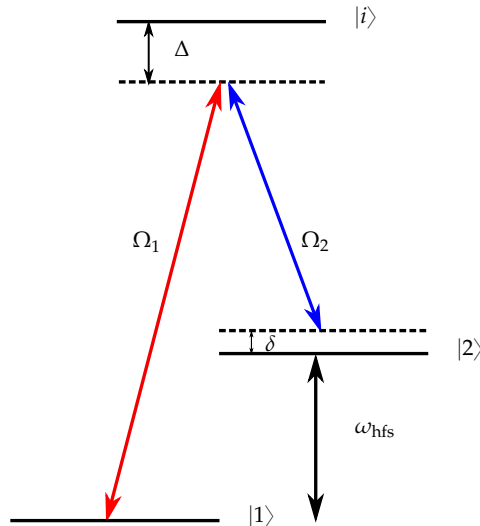


**Figure 2.3.:** Schematic diagram of a raman transition. Two states,  $|1\rangle$  and  $|2\rangle$ , are coupled to each other via transitions to an intermediate state  $|i\rangle$ . When the frequencies of the light fields are far-detuned from resonance, then  $|i\rangle$  can be adiabatically eliminated, resulting in an effective two-level system.

### 2.3.1. State Propagation

To describe the dynamics of the Raman transition, it is convenient to express the system in the interaction picture. This allows the Hamiltonian to be represented in a time-independent form. An analytic solution to the equations of motion can then be obtained, which describes the evolution of the atomic state during a Raman transition. After adiabatically eliminating the intermediate state [19], the state of the atom in a rotating frame is given by

$$|\psi\rangle = c_1 e^{-i\omega_1 t} |1\rangle + c_2 e^{-i(\omega_2 + \delta)t} |2\rangle \quad (2.17)$$

The Hamiltonian can be simplified by making the rotating wave approximation, which neglects the rapidly oscillating terms. After this, the Schrödinger equation becomes

$$i \begin{pmatrix} \dot{c}_1 \\ \dot{c}_2 \end{pmatrix} = \frac{1}{2} \begin{pmatrix} -\Omega_1^{\text{ac}} & \Omega_{\text{eff}} \\ \Omega_{\text{eff}}^* & -2\delta - \Omega_2^{\text{ac}} \end{pmatrix} \begin{pmatrix} c_1 \\ c_2 \end{pmatrix} \quad (2.18)$$

Where in terms of the single-photon Rabi frequencies  $\Omega_1$  and  $\Omega_2$ , the ac Stark shifts  $\Omega_j^{\text{ac}}$  and effective Rabi frequency  $\Omega_{\text{eff}}$  are given by

$$\Omega_j^{\text{ac}} = -\frac{|\Omega_j|^2}{2\Delta} \quad (2.19a)$$

$$\Omega_{\text{eff}} = \frac{e^{i\phi_{\text{eff}}} |\Omega_1| |\Omega_2|}{2\Delta} \quad (2.19b)$$

Under an appropriate choice of intensities and two-photon detuning, it is possible to cancel the differential ac Stark shift  $\Omega_1^{\text{ac}} - \Omega_2^{\text{ac}}$  (see Section 7.4.2 for further details on this). Therefore, they can be omitted from equation (2.18) so that after solving the

Schrödinger equation, the coefficients  $c_1, c_2$  evolve according to

$$\begin{pmatrix} c_1(t) \\ c_2(t) \end{pmatrix} = U \begin{pmatrix} c_1(0) \\ c_2(0) \end{pmatrix} \quad (2.20)$$

where the propagator  $U$  is

$$U = e^{\frac{1}{2}i\delta t} \begin{pmatrix} \cos\left(\frac{\Omega' t}{2}\right) - i\frac{\delta}{\Omega'} \sin\left(\frac{\Omega' t}{2}\right) & -ie^{i\phi_{\text{eff}}}\frac{\Omega_{\text{eff}}}{\Omega'} \sin\left(\frac{\Omega' t}{2}\right) \\ -ie^{-i\phi_{\text{eff}}}\frac{\Omega_{\text{eff}}}{\Omega'} \sin\left(\frac{\Omega' t}{2}\right) & \cos\left(\frac{\Omega' t}{2}\right) + i\frac{\delta}{\Omega'} \sin\left(\frac{\Omega' t}{2}\right) \end{pmatrix} \quad (2.21)$$

and  $\Omega' = \sqrt{\delta^2 + \Omega_{\text{eff}}^2}$  is the generalised Rabi frequency. After transforming back into the stationary frame, equation (2.21) becomes

$$U = \begin{pmatrix} e^{\frac{i(\omega_{\text{eff}}-\delta_R)t}{2}} \left( \cos\left(\frac{\Omega' t}{2}\right) - i\frac{\delta}{\Omega'} \sin\left(\frac{\Omega' t}{2}\right) \right) & -ie^{\frac{i(\omega_{\text{eff}}-\delta_R)t}{2}} e^{i\phi_{\text{eff}}}\frac{\Omega_{\text{eff}}}{\Omega'} \sin\left(\frac{\Omega' t}{2}\right) \\ -ie^{\frac{-i(\omega_{\text{eff}}-\delta_R)t}{2}} e^{-i\phi_{\text{eff}}}\frac{\Omega_{\text{eff}}}{\Omega'} \sin\left(\frac{\Omega' t}{2}\right) & e^{-\frac{i(\omega_{\text{eff}}-\delta_R)t}{2}} \left( \cos\left(\frac{\Omega' t}{2}\right) + i\frac{\delta}{\Omega'} \sin\left(\frac{\Omega' t}{2}\right) \right) \end{pmatrix} \quad (2.22)$$

where  $\delta_R = \mathbf{k}_{\text{eff}} \cdot \mathbf{v} + \hbar |\mathbf{k}_{\text{eff}}|^2 / 2m$  is the Raman detuning from equation (2.16).

### 2.3.2. Application to a Sequence of Raman Pulses

Now, this propagator can be used to determine the state of the atom after a sequence of Raman pulses. The propagator was derived using an initial state at  $t = 0$ . This can be generalised to an arbitrary time by replacing  $t \rightarrow t - t_0$  and  $\phi_{\text{eff}} \rightarrow \phi_{\text{eff}} + \omega_{\text{eff}}t_0$ . Between successive Raman pulses, there is a period of free evolution for a time  $T$ .

During this, the state evolves according to

$$F(T) = \begin{pmatrix} e^{-i\frac{\omega_{\text{hfs}}T}{2}} & 0 \\ 0 & e^{i\frac{\omega_{\text{hfs}}T}{2}} \end{pmatrix} \quad (2.23)$$

Treating the Rabi frequency, phase, detuning and pulse duration as free parameters denoted by an index  $j = 1, 2, 3$ , the state after three arbitrary pulses separated in time is given by

$$|\psi\rangle = U(\Omega_3, \phi_3, \delta_3, \tau_3)F(T_2)U(\Omega_2, \phi_2, \delta_2, \tau_2)F(T_1)U(\Omega_1, \phi_1, \delta_1, \tau_1)|\psi_0\rangle \quad (2.24)$$

for an initial state  $|\psi_0\rangle$ . This expression is valid for arbitrary pulses and is useful when considering a distribution of intensities and Doppler detunings across an atomic ensemble. For instance, the occupation probability for  $|2\rangle$  is given by

$$P_{|2\rangle} = |\langle 2|\psi\rangle|^2 \quad (2.25)$$

It is also useful to define the fringe contrast – the difference between the maximum and minimum of  $P_{|2\rangle}$

$$c = \max_{\Delta\Phi} P_{|2\rangle} - \min_{\Delta\Phi} P_{|2\rangle} \quad (2.26)$$

which ranges between 0 and 1. This fringe contrast implicitly depends on the pulse area and detuning of each pulse. In the case of perfect pulse areas and zero detuning with the initial state  $|\psi_0\rangle = |1\rangle$ , equation (2.25) yields the following

$$\begin{aligned} P'_{|2\rangle} &= \sin\left(\frac{1}{2}(\phi_1 - 2\phi_2 + \phi_3)\right)^2 \\ &= \sin\left(\frac{\Delta\Phi}{2}\right) \end{aligned} \quad (2.27)$$

Where  $\Delta\Phi$ , defined in equation (2.13), is recovered by substituting  $\phi_j \rightarrow \phi_j^{(l)} + \mathbf{k} \cdot \mathbf{x}$  and using the position of the centre-of-mass at each pulse for  $\mathbf{x}$ .

### 2.3.3. Extending to a Real Atomic System

In a real atomic system, there are many intermediate states which couple to the two ground states. This theory can be extended to consider the additional intermediate states using their individual Rabi frequencies. In this case, the effective Rabi frequency is given by the following sum

$$\Omega_{\text{eff}} = e^{i\phi_{\text{eff}}} \sum_k \frac{|\Omega_{1k}| |\Omega_{2k}|}{2\Delta_k} \quad (2.28)$$

where the index  $k$  labels the intermediate states which couple to both  $|1\rangle$  and  $|2\rangle$ . A similar expression can be obtained for the ac Stark shift terms. The effective Rabi frequency in equation (2.28) implicitly depends on the polarisation of the light. The individual Rabi frequencies  $\Omega_{jk}$  are calculated using the Clebsch-Gordan coefficients that describe the coupling of angular momentum states. Further detail on calculating transition matrix elements of tensor operators can be found in [20].

## 2.4. Applications to Rubidium-87

This final section places what has been discussed thus far into the context of Rubidium-87, the atomic species used in this experiment. It begins with a presentation of the atomic structure of the D2 transition in Section 2.4.1. Transitions between different hyperfine levels are used throughout this experiment. Most importantly, these are used for cooling and trapping, as well as driving Raman transitions. This is followed by an overview of the techniques used to drive counter-propagating Raman transi-

tions in Section 2.4.2. In particular, this motivates the choice of polarisation used for the two Raman beams. Finally, this section concludes with a discussion of the two interferometer paths in Section 2.4.3.

### 2.4.1. Atomic Structure

Rubidium-87 has a hyperfine structure that is well-suited for a wide range of experiments. For instance, the energy splitting in the  $5P^{3/2}$  level is large enough that it can be efficiently laser cooled using one laser to cool and another to prevent dark state population build-up.

In addition to this, the existence of two hyperfine levels in its ground state presents suitable choices of states for interferometry. Neither the  $|F = 1\rangle$  nor  $|F = 2\rangle$  levels will spontaneously decay, which helps to preserve their coherence during the interferometer. Particular pairs of Zeeman sub-levels can be identified which are coupled via a Raman transition. When the two laser fields are counter-propagating, this imparts much more momentum than the equivalent microwave transition. This is desirable for acceleration sensing, since the sensitivity is directly proportional to the recoil momentum.

The D2 transition between the  $5S^{1/2}$  ground state and  $5P^{3/2}$  excited state is shown in Figure 2.4. The key transitions used in this experiment are also indicated. The Zeeman sub-levels (which range from  $-F, -F + 1, \dots, F$ ) are not shown explicitly but can be inferred from the Landé  $g$ -factor. The energy difference of two Zeeman sub-levels is  $E_m - E'_m = g_F B(m - m')$ . The values listed are taken from [21]. Further quantities, such as relative transition strengths and physical properties of Rubidium-87 are contained therein.

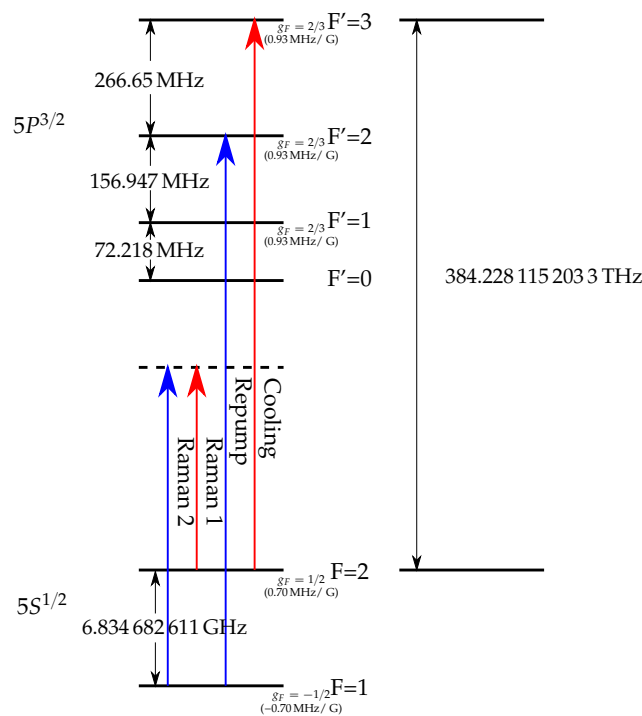


**Figure 2.4.:  $^{87}\text{Rb}$  D2 transition hyperfine structure.** The absolute energy difference of the  $|F = 2\rangle$  and  $|F' = 3\rangle$  levels is shown as an equivalent frequency. The energy of the other levels are shown relative to this. The approximate g-factors for each hyperfine level and Zeeman shifts are also indicated. The main transitions used in this experiment are indicated by red and blue arrows. The values are taken from [21].

### 2.4.2. Driving Raman Transitions

Within the Rubidium-87 ground state, there are multiple pairs of states that can be coherently coupled using a Raman transition. A natural choice is the  $m_F = 0$  sub-levels<sup>1</sup>. These are magnetically-insensitive; their transition frequency has at most a second-order Zeeman shift. Consequently, this transition is least affected by magnetic field variations from field gradients or environment noise.

The polarisation of the two light fields is crucial to ensuring that the  $\Delta m_F = 0$  transition is driven. The  $|1, 0\rangle \rightarrow |2, 0\rangle$  transition does not change the magnetic quantum number, i.e. the projection of angular momentum along the given quantisation axis. However, the total angular momentum quantum number increases by 1, which means that the Raman transition is described by a vector operator proportional to the product of two dipole operators. This can occur when the two electric field are orthogonally linearly polarised ( $\text{lin} \perp \text{lin}$ ) to each other and to the quantisation axis.

For circular polarisation, it can be shown that the two fields must have the same handedness. The electric field of a right-handed circularly polarised beam is  $\mathbf{E} = E_+ e^{-i\omega t} + E_- e^{i\omega t}$ , so the product  $\mathbf{d} \cdot \mathbf{E}$  can be written as

$$r_j = (d_+^{(j)} E_+^{(j)} e^{-i\omega_j t} + d_-^{(j)} E_-^{(j)} e^{i\omega_j t}) \quad (2.29)$$

where  $d_+^{(j)}$  and  $d_-^{(j)}$  are the components of the dipole operator which increase and decrease  $m_F$ , respectively. The index  $j$  labels the  $|j, 0\rangle$  state. The product  $r_1 \times r_2$  is expanded to give

$$r_1 \times r_2 = (d_+^{(1)} E_+^{(1)} d_-^{(2)} E_-^{(2)} e^{-i(\omega_1 - \omega_2)t} + d_-^{(1)} E_-^{(1)} d_+^{(2)} E_+^{(2)} e^{i(\omega_1 - \omega_2)t}) \quad (2.30)$$

---

<sup>1</sup>In what follows, the states  $|1\rangle$  and  $|2\rangle$  will be used as alternative notation for  $|F = 1, m_F = 0\rangle$  and  $|F = 2, m_F = 0\rangle$  in instances where the explicit quantum numbers are not required

where the first term corresponds to the component which drives  $|1, 0\rangle \rightarrow |2, 0\rangle$  and the second to  $|2, 0\rangle \rightarrow |1, 0\rangle$ . The terms proportional to  $(\omega_1 + \omega_2)$  have been neglected as they are off-resonant. A similar argument follows in the case of two left-handed circular polarised fields  $\mathbf{E} = E_+e^{-i\omega t} - E_-e^{i\omega t}$ . Conversely, a pair of left- and right-handed beams will not drive transitions. The product of the dipole operators results in components of the form  $d_+^{(1)}d_+^{(2)}$ , which change the magnetic quantum number by  $\pm 2$ .

### 2.4.3. The Double Interferometer

The two frequencies for driving the Raman transition are sent into the experiment along the fast and slow axis of a Polarisation-Maintaining (**PM**) fibre. To produce the necessary counter-propagating beams, a Quarter-wave Plate (**QWP**) and mirror retro-reflect and invert the polarisation of each beam. This results in the beam configuration shown in Figure 2.5. With a magnetic field aligned parallel to the light's wavevector, each beam drives  $\sigma^\pm$  transitions. The  $\Delta m_F = 2$  transitions corresponding to the  $\sigma^+ - \sigma^-$  combinations are forbidden, leaving the two combinations which drive counter-propagating  $\Delta m = 0$  transitions. These have effective wavevectors in opposite directions, which means that an atom resonant with both pairs is driven into a superposition of  $|1, \mathbf{p}\rangle$ ,  $|2, \mathbf{p} + \hbar\mathbf{k}\rangle$  and  $|2, \mathbf{p} - \hbar\mathbf{k}\rangle$ . The  $\pi/2 - \pi - \pi/2$  pulse sequence results in a trajectory shown schematically in Figure 2.6. Two sets of paths recombine to form an interferometer which have oppositely signed phase shifts. The fact that there is no longer a single momentum eigenstate associated with  $|2\rangle$  means that not every trajectory will overlap. Consequently, this results in a loss of coherence between the two states. Fortunately, these Raman transitions have Doppler shifts of opposite sign. Therefore, by appropriately detuning the light from resonance, an atom with a non-zero velocity will be shifted closer to resonance with one pair and further out from the other. Indeed, if the difference between their resonances  $2|\mathbf{k}_{\text{eff}} \cdot \mathbf{v}|$  is larger

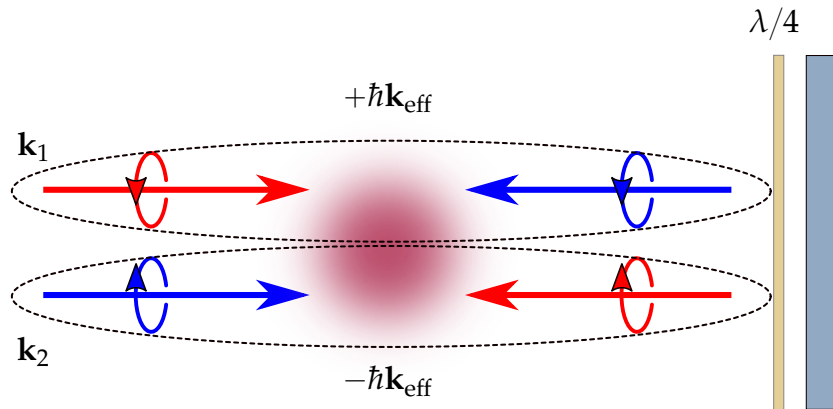


**Figure 2.5.:** Raman beam configuration. The two incoming beams are orthogonally circularly polarised. The reflected beams pass through a QWP to invert their handedness. The selection rules of the Raman transition result in two pairs of beams that drive transitions with oppositely directed effective wavevectors.

than the transition linewidth, only one pair of beams drives the transition. The moving molasses method used to launch the atoms and lift this degeneracy is discussed later, in Section 5.2.3; a characterisation of the Raman transition spectrum in the experiment is presented in Section 7.4.1

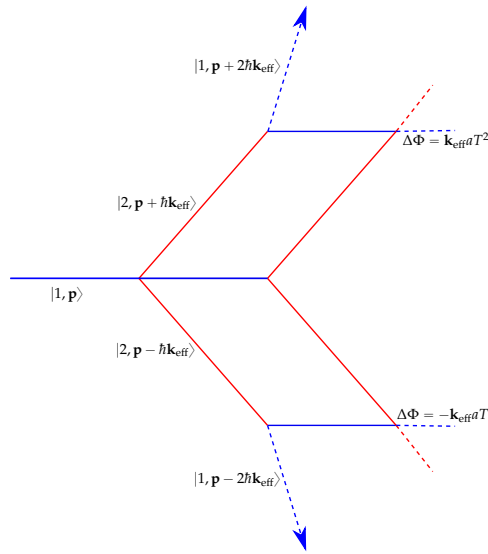


**Figure 2.6.:** Interferometer paths with two oppositely directed Raman transitions. If the atom is resonant with both transitions, its momentum changes by  $\pm \hbar \mathbf{k}_{\text{eff}}$ . This results in two interferometers with oppositely signed phase differences. The dashed directed lines indicate trajectories which will not interfere, leading to a loss of coherence.

## 2.5. note on units

in subsequent chapters of this thesis, various non-si units are used for convenience.

Their values are defined here:

- 1 Gauss (G) =  $1 \times 10^{-4}$  T
- $g = 9.806\,65\text{ m s}^{-2}$  (as defined in [22])

## 2.6. Conclusion

This chapter has presented a theoretical overview of matter-wave interferometry and motivated the use of a  $\pi/2 - \pi - \pi/2$  sequence of laser pulses to measure the acceleration of an atom. Furthermore, it was shown how this can be implemented using a Raman transition between two ground states in  $^{87}\text{Rb}$ . This induces a larger momentum recoil when compared to a microwave transition and thus, a greater sensitivity to accelerations. The effect of rotation on the interferometer phase has not been discussed. For further details on an atom interferometer gyroscope, the reader is referred to [23].

# **Chapter 3.**

## **MOTMaster**

### **3.1. Chapter Overview**

The aim of this chapter is to provide a description of the MOTMaster software, which was developed from a pre-existing version during my PhD. The design of MOTMaster assumes very little about the particular experiment it is being used for, so much of the discussion in this chapter will be kept general. This chapter begins with a motivating the need to extend MOTMaster by developing a graphical interface to simplify the creation of experimental sequences, as well as implementing new methods of controlling hardware. This is followed by a description of how input and output channels are controlled using MOTMaster in Section 3.3. The structure of a MOTMaster sequence, along with how it runs an experiment is then presented in Section 3.4. Finally, the specific hardware used in this experiment and an overview of each major step of the experiment is given in Section 3.5.

## 3.2. Motivation

In the initial stages of my PhD, I decided to use Cicero Word Generator [25] to control the hardware for the experiment. This is a graphical-based control system developed by Wolfgang Ketterle's group at MIT, which was designed for controlling atomic physics experiments using National Instruments hardware. Over time, as the experiment became more complex, it started to become apparent that Cicero was not suited to meet all of our requirements for control software. This was most evident in the control of the M-Squared Raman laser system. Cicero also takes an appreciable amount of time (around 300 ms) to re-calculate the experiment sequence between each shot. Since the design of Cicero was aimed at controlling experiments that take many seconds per cycle, this dead time between each cycle is not significant on those time scales. In contrast, each cycle of this experiment takes around 250 ms. This unnecessary dead time needed to be addressed if we hoped to improve the repetition rate.

After it became clear that a potentially large amount of work would be needed to improve Cicero, I decided that it was worth moving to a new control system. A collection of programs, named EDMSuite, has been developed by people in Centre for Cold Matter (CCM) to control a range of experiments within the group. One application, MOTMaster, was designed to control and acquire data from experiments investigating cold atoms trapped in a MOT. However, its method of structuring experimental sequences was inconvenient, as it lacked an intuitive graphical user interface. During the process of switching to using MOTMaster to control the experiment, I designed a graphical method of structuring sequences, which functioned identically on a device level to the original method of defining sequences. In addition to this, I included an interface to the M Squared laser system, so that it could be controlled using MOTMaster. A schematic of the structure of MOTMaster and how it interfaces with hardware

is shown in Figure 3.1. It is designed so that experiments can be controlled without requiring specific details about the hardware in use.

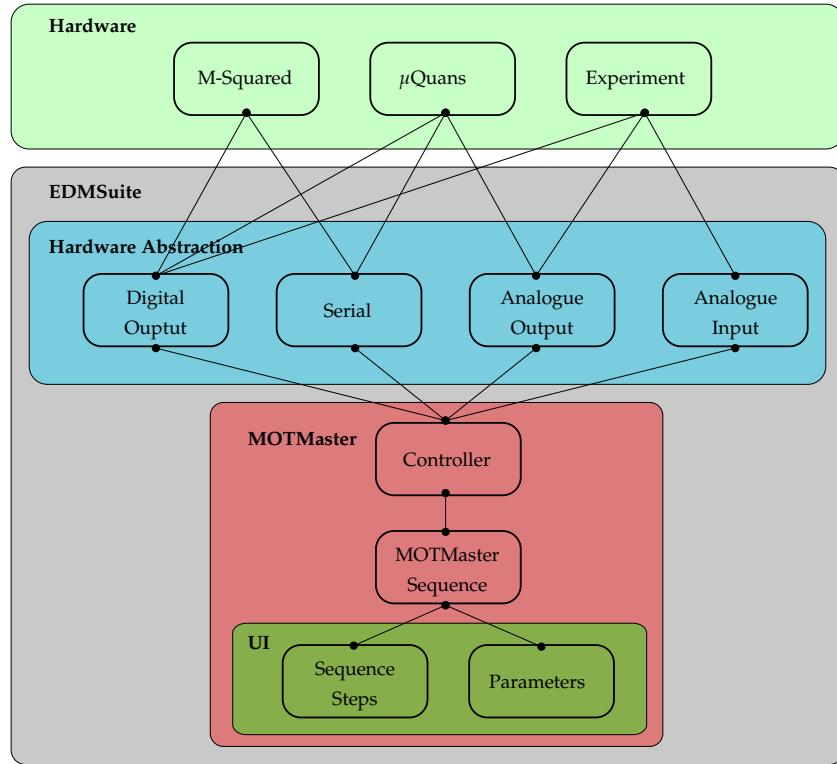


**Figure 3.1.:** Schematic diagram of MOTMaster and the hardware it controls. A sequence is built using the user interface, which then uses separate modules to communicate to the hardware. In this way, an experiment can be controlled without requiring specific knowledge of the hardware.

### 3.3. Interfacing with Hardware

The majority of the experimental hardware is controlled using analogue and digital voltages that are generated by Data Acquisition (**DAQ**) cards manufactured by National Instruments. MOTMaster is compatible with cards that use either the NI-DAQmx or NI-HSDIO device drivers. These are used to configure the generation or acquisition of digital or analogue voltage waveforms. By design, they are capable of precisely timing and synchronising their I/O across multiple devices. Most

components in the experiment rely on this precise timing to function correctly. Other devices, where timing accuracy is less critical, are controlled by sending or receiving data using serial communication. This has the advantage of allowing more structured command beyond analogue or digital voltages, but the communication speed of the serial channel limits the accuracy of the execution time.

The following section describes the low-level interface between MOTMaster and the experimental hardware. It begins by introducing the concept of hardware abstraction in Section 3.3.1. This is followed by a more detailed discussion of how each type of control is implemented. Section 3.3.2 describes how analogue and digital output waveforms are generated. Section 3.3.3 outlines serial communication, along with a method for triggering this communication during an experiment. Finally, this section concludes with a discussion on acquiring analogue input data, which is given in Section 3.3.4.

### 3.3.1. Hardware Abstraction

When designing software, it is often useful to structure a program in such a way that modules which make use of other components do not need to know about their specific implementation in order to use them. This approach means that the submodule can be modified without harming the compatibility of these two components. In the context of experimental hardware, this is equivalent to requiring that changing specific components, for example the Voltage-Controlled Oscillator (**VCO**) that generates the RF power for an **AOM**, will not stop the experiment from working. This is done using abstract representations of the hardware, in the form of input and output channels that are used to communicate to each device.

### 3.3.2. Voltage Pattern Generation

#### Analogue Outputs

All the analogue outputs controlled using MOTMaster are done using the NI-DAQmx software. Each output uses a Digital-to-Analogue Converter (**DAC**) to convert a floating-point number into an analogue voltage. To generate a sequence of voltages across multiple channels, the NI-DAQmx driver allocates a block of memory on the **DAQ** card for each output channel. This memory acts as a first-in first-out (FIFO) buffer for data streamed to it from a computer. The output of each channel is synchronised to a clock signal, so that every time a rising edge occurs on the clock, the voltage at each output transitions to the value corresponding to the next value in its corresponding buffer. Channels across multiple **DAQ** cards can be synchronised by sharing a clock signal, which can be done using the bus that connects cards in a PXI-e chassis. Additional cards can also be configured to trigger the start of their output at the moment they receive the first clock pulse, rather than waiting for a software trigger from the computer.

#### Digital Outputs

Digital outputs from NI-DAQmx cards are generated in much the same way as analogue voltages, except for the fact that they only take two values corresponding to either a low (0 V) or high (3.3/5 V) level. Additionally, **DAQ** cards which use the NI-HSDIO driver can be used. These cards can be sampled at much higher rates than NI-DAQmx ones. For instance, the NI-HSDIO PXI-6541 card can generate digital voltages at sample rates up to 50 MHz. Rather than writing the pattern as an array of values at each clock cycle, the sequence is segmented into smaller patterns during which the state of each channel is constant, as illustrated in Figure 3.2. NI-HSDIO

cards can be scripted to generate each of these patterns for the appropriate number of clock cycles.

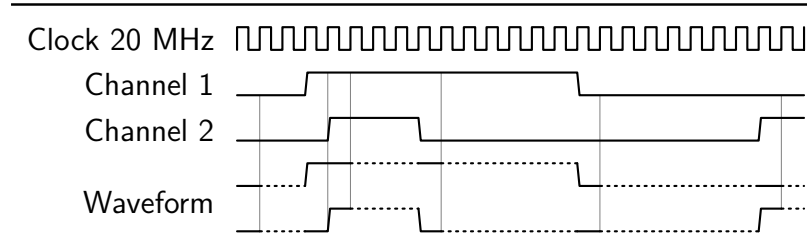


**Figure 3.2:** Scripted pattern generation for an NI-HSDIO digital output card. A pattern is split into segments which correspond to a duration for which all the channels output a constant value. Each of these smaller waveforms are written to the on-board memory, along with a script that instructs the card to output each pattern for the required number of times to reconstruct the original sequence. By reducing the amount of memory required to define the sequence, a faster clock frequency and hence timing resolution can be used to output digital control signals.

### 3.3.3. Timed Serial Communication

Serial communication is used to control devices which require more complex control than is possible using analogue or digital voltages. This increase in complexity comes at the cost of slower response times, because it takes longer to communicate an array of bytes than to change the voltage across an output terminal. Using the NI-VISA driver, the output of serial data can only be timed using a software clock on a computer, which is more prone to jitter than a hardware clock. One way to improve the synchronisation between serial data and hardware timed outputs is to use extra hardware to trigger the transmission of serial data. If the trigger is timed using the same clock as other outputs and the transmission delay is accounted for, then serial data can be output more synchronously. The scheme for timing serial messages is shown in Figure 3.3. Serial messages are stored as strings on the computer and a counter channel is configured so that every time it detects a rising edge, the computer outputs the next message. This counter is connected to a digital output channel, so that it acts as a trigger for the serial

data output. Using this method, multiple serial messages can be sent to one device during a sequence even for devices which have no means of storing commands.

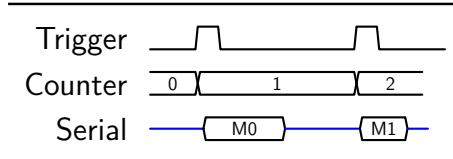


**Figure 3.3.:** Timing diagram for serial communication. A counter channel is configured to count edges from a digital output channel. Every time it sees a rising edge, it triggers the output of the next message on each serial channel from the computer. Multiple messages can be communicated during a single sequence without the need for software timing.

### 3.3.4. Voltage Acquisition

Analogue input channels are configured in a similar way to analogue output channels. A block of memory is allocated on the DAQ card for each input channel. Once the card is triggered to start acquiring, an Analogue-to-Digital Converter (ADC) converts the voltage across the input into a digital value at every rising edge of the clock signal. Once the sequence has finished, or the buffer has been filled, the card streams this data to the computer.

## 3.4. MOTMaster Sequences

In addition to interfacing with control hardware, MOTMaster is used to define the structure of experimental sequences. In earlier versions of MOTMaster, sequences were defined using functions within a C# source file. To run an experiment, MOTMaster compiled this file to build the voltage patterns and wrote them to the hardware. Whilst this had little overhead in resources needed to build and run a sequence, modifying and debugging sequences was much more time consuming. Taking inspiration from

Cicero, the user interface of MOTMaster was redesigned so that sequences could be expressed graphically. They are then built using the same functions as before, so that from the point of view of the hardware, the two methods of control are equivalent.

### 3.4.1. Sequence Structure

A MOTMaster sequence is composed of a list of sequence steps, which define the state of the control hardware over a discrete amount of time. Each step contains the following properties:

- Name: A descriptive name for the step.
- Duration: duration of the step, which must be an integer multiple of the timebase (e.g. 10 µs for a 100 kHz sample clock frequency).
- Serial Channel: A serial message encoded as a string of text.
- Digital Output Channel: High (3.3 V) or Low (0 V)
- Analogue Output Channel: Single value, step or ramp the output from a start to end value, or output an arithmetic function over time.

where each individual output channel has its own property.

A sequence step is useful to represent a single action, so that each stage of the experiment, for example the initial MOT loading phase, is composed of multiple steps. Numerical values, such as analogue voltages or times, can be represented by named parameters. The value of a parameter can be updated between each cycle of the experiment, so that MOTMaster can implement a scan by iterating a parameter through a range of values. The sequence steps are also used to define when to acquire from the analogue inputs. A specific digital channel, named acquisitionTrigger, is reserved as a start trigger for the acquisition. This channel is also used to define the length of

time over which to acquire data. Analogue data acquisition is triggered at the start of the step where this channel goes high and stops when it goes low.

### 3.4.2. Running a Sequence

MOTMaster is designed to run in two modes, referred to as repeat and scan. The distinction between these is that the repeat mode does not need to recreate a sequence between each cycle. Before MOTMaster starts controlling the experiment, the sequence is built once and the output hardware is configured to regenerate their patterns. This reduces the delay between each cycle, which is largely a result of the time needed to process acquired data and reconfigure the control hardware. In contrast, scan mode varies a parameter during each cycle, so additional time is required to rebuild the sequence and write to each **DAQ** card. Aside from this, these modes operate equivalently.

At the start of an experiment cycle, the hardware is initialised and timing properties, such as the trigger and sample clock for each **DAQ** card is set. An example of a sequence as represented in the user interface is shown in Figure 3.4. This is converted into the analogue and digital voltage patterns for each **DAQ** card. The required buffer for the analogue input data is calculated based on the state of the `acquisitionTrigger` channel. If any serial commands are used, the timing properties of the counter channel are configured, similarly to the rest of the **DAQ** hardware. The sequence is started by sending a software trigger to one output card, which is configured to export its start trigger to the other cards. This ensures that start of the output of each card is synchronised.

After the sequence has finished, any acquired data from the analogue input channels is streamed to the computer. The data per channel are segmented into arrays that were

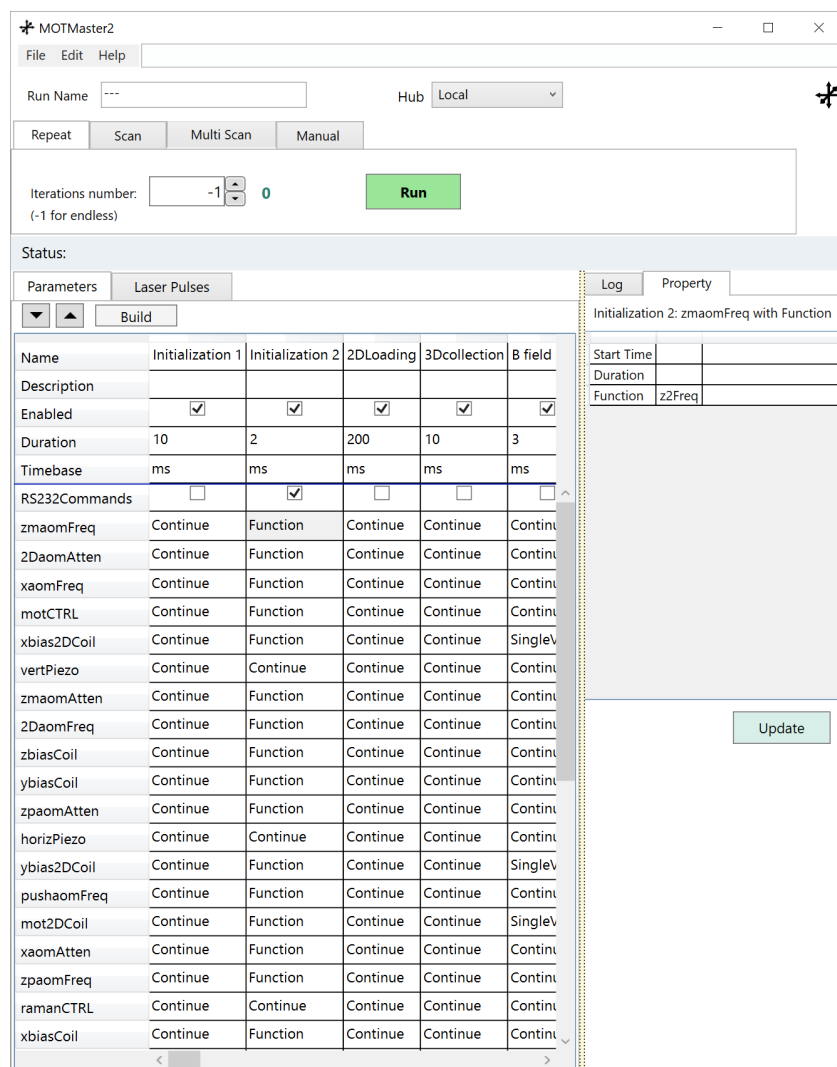


**Figure 3.4.:** A sequence as represented in the MOTMaster user interface. Each step defines a duration and properties for each output channel. The sequence can either be run repeatedly, or configured to iterate through values of a chosen parameter.

acquired during each sequence step, before additional post-processing if required. Finally, the hardware is reset to its initial state, before starting the next experiment cycle.

### 3.5. Experiment Control Hardware

In the preceding sections, the discussion of MOTMaster has been presented without referring to specific hardware used in this experiment. Subsequent chapters will introduce components of the experiment that are controlled by a computer, but it is worth introducing the hardware used to implement this control. A diagram of the control hardware is shown in Figure 3.5. All of the **DAQ** cards are housed on a PXIe-1073 chassis, so that timing signals such as start triggers and sample clocks can be shared on the PXI backplane. The analogue output signals are generated on a PXI-6723 card. This contains 32 analogue output channels and the output of each is generated using a 13 bit **DAC**. Over the maximum voltage range of  $\pm 10\text{ V}$ , this corresponds to an output quantisation of  $2.44\text{ mV}$ , which did not limit the precision of any analogue control in the experiment. The analogue output pattern is sampled at a frequency of  $100\text{ kHz}$ , which gives a minimum resolution of  $10\text{ }\mu\text{s}$ . Any jitter on this sample clock did not produce any noticeable effects during the experiment.

Two cards on the chassis are able to acquire data from analogue inputs. The first is a PXIe-6341, which has 16 input channels, each with a 16-bit **ADC**. In addition to this, a counter channel on this card was used to trigger the output of serial messages. During the preliminary stages of the experiment, this bit-depth was sufficiently large to prevent quantisation effects becoming significant. However the AI-Q-2010 MEMS accelerometer used in the experiment, discussed further in Section 6.4.2, has an equivalent voltage noise below this quantisation level. Therefore, a PXI-4462 card, which

contains 4 24-bit analogue input channels, was added. This card is used to acquire data from devices where the higher voltage resolution is desirable — namely, the MEMS accelerometer and the photodiode used to detect the population of atoms in each state after interference.

Digital output signals are generated using a PXI-6541 card. Unlike the others, this card is controlled using the NI-HSDIO driver. With a maximum sampling frequency of 50 MHz, this card is capable of generating digital signals at a much higher rate than the PXIE-6341, which also contains digital output channels. However, the PXIE-6341 card only contains 8 digital channels that can be timed using a hardware clock, fewer than required to control the entire experiment.

Two components of the experiment are controlled during the experiment using serial communication. The first of these is an interface to the Direct Digital Synthesiser (DDS) on the  $\mu$ Quans laser which control the frequency of the cooling and repump lasers and is controlled in real-time during the experiment. This communication protocol is described in further detail in Section 4.3.3. Finally, MOTMaster is configured to remotely connect to the M Squared laser, so that it can control all the parameters necessary to drive Raman transitions during the experiment. This is done by sending structured JSON messages that contain commands to implement this control. More detail on how this is used in the experiment is given in Section 7.2.2.

## 3.6. Experimental Sequence Overview

The experiment can be broken down into the following stages:

- Loading: Atoms are loaded from the 2D MOT into the 3D MOT.

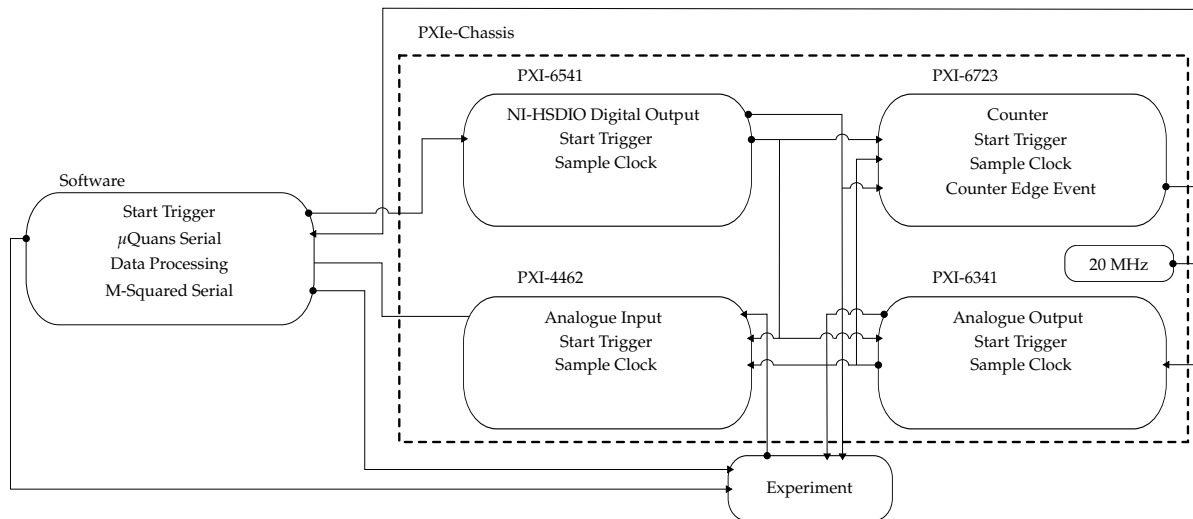


**Figure 3.5.:** Schematic diagram of the control hardware. The PXle chassis contains the DAQ cards which generate the analogue and digital waveforms used to control other devices. Signals are routed between the cards to synchronise their operation. Serial communication to the  $\mu$ Quans laser (Section 4.3), the M-Squared laser (Section 7.2) and the CCD camera (Section 4.2.3) are used for their control.

- Molasses: Atoms are released from the trap and cooled further in an optical molasses.
- State Preparation: A sequence of optical and microwave pulses are used to prepare atoms with a narrow velocity spread in the  $|1, 0\rangle$  state.
- Interferometry: A  $\pi/2 - \pi - \pi/2$  sequence of laser pulses drive Raman transitions between the atoms.
- Detection: Two laser pulses are used to measure the number of atoms in  $|F = 2\rangle$  and the total number, respectively. From these measurements, the interferometer phase difference can be inferred.

# **Chapter 4.**

## **Cooling and Trapping in a MOT**

### **4.1. Chapter Overview**

This chapter presents a description of the components of the experiment which are used to trap and cool atoms in a MOT. An outline of the hardware used to create both the 2D and 3D MOTs is presented in Section 4.2. Following this is a description of the  $\mu$ Quans laser system, in Section 4.3, which generates the light used to cool and trap atoms. The hardware used to control the frequency and power of each MOT beam, as well as the required magnetic fields, is given in Section 4.4. Finally, this chapter concludes with a characterisation of the 3D MOT loading rate in Section 4.5

### **4.2. The Navigator Vacuum Chamber**

The vacuum chamber, along with the components mounted to it, make up the majority of the hardware used in the preliminary trapping and cooling stages of the experiment. Figure 4.1 shows a diagram of the vacuum chamber and the main MOT components.

The chamber is made of 316L stainless steel, which has a low magnetic permeability to reduce stray magnetic fields on the atoms. It contains 16 DN40 ConFlat ports arranged on the edges of three octagons, one in each Cartesian coordinate plane. Six of these ports provide optical access for the 3D MOT. Another port connects the 2D MOT system to the main chamber. One port provides optical access for either a CCD camera or photodiode. Opposite this is a microwave horn for driving microwave transitions between the two  $^{87}\text{Rb}$  hyperfine ground states. The remaining ports are not used for optical access since they do not have a direct line of sight to the atoms. Instead, these are used to mount a pressure gauge, gate valve, a Non-evaporative Getter (NEG) pump and electrical feedthroughs for the MOT coils.

Two oppositely-facing DN63 ports are used to mount the optics for driving Raman transitions<sup>1</sup>. This is the axis along which the atom interferometer is sensitive to accelerations, subsequently referred to as the Raman axis.

The chamber is pumped down to a pressure of around  $5 \times 10^{-10}$ mbar using a NexTorr D100-5 pump. This is a composite system consisting of NEG and an ion pump. The NEG is a porous sintered zirconium (St 172) element, which reacts with chemicals such as hydrogen, water, nitrogen, oxygen and hydrocarbons. Most of these were removed during the initial baking and roughing pump stages. Under Ultra-high Vacuum (UHV) conditions, the largest contributor to the pressure is hydrogen which the NEG can pump at a speed of  $100\text{ l s}^{-1}$ . Any species that are not absorbed by the NEG, in particular Rubidium, are pumped by the  $5\text{ l s}^{-1}$  ion pump.

---

<sup>1</sup>For more information about the Raman optical system, refer to Chapter 6

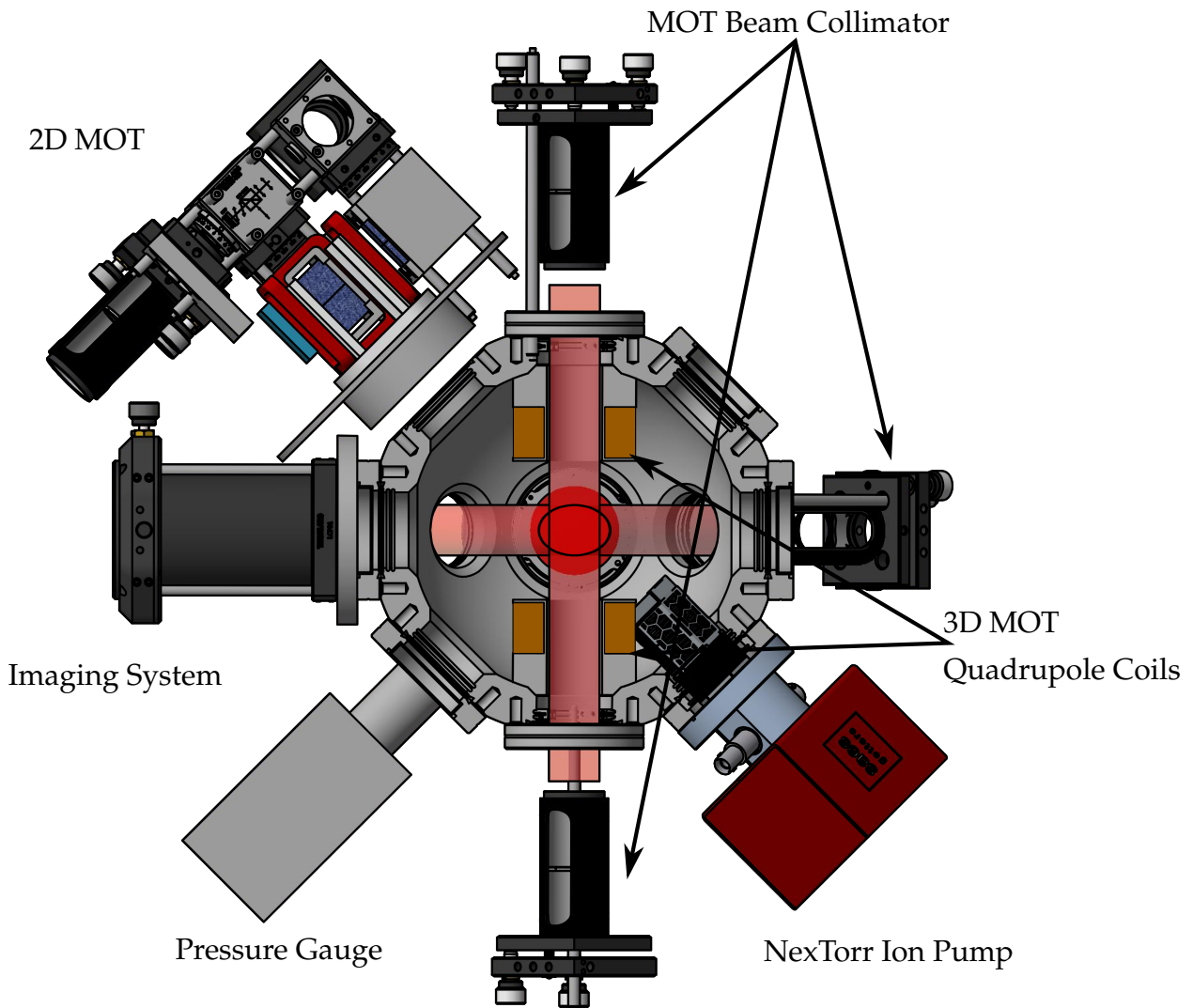


**Figure 4.1.:** A diagram of the main components on the vacuum chamber used for the MOT systems. Rubidium atoms are dispensed and loaded into the 2D MOT before being pushed into the main chamber and collected in the 3D MOT. A set of 6 beam collimators provide the light to slow and cool atoms. A spherical quadrupole field traps atoms at the centre of the chamber. Not shown are additional bias coils along each MOT beam axis to null stray fields at the centre of the chamber.

### 4.2.1. The 2D MOT system

At room temperature, a large fraction of atoms have velocities greater than typical MOT capture velocities, so a very high partial pressure of Rubidium is needed to achieve a fast loading rate from a background vapour. This also contributes to a high background atom number, which reduces the interferometer fringe visibility. Loading from a 2D MOT [26] system both increases the loading rate and decreases the pressure inside the main chamber.

A diagram of the light and magnetic fields required to produce a 2D MOT is presented in Figure 4.2. It is similar to the 3D MOT, with the main exception being that only 4 beams are used to cool the atoms along 2 orthogonal axes. It is designed to produce a large flux of cold atoms which can be subsequently loaded into a 3D MOT. The cooling beams are collimated to a large waist size and the magnetic field coils produce a cylindrical quadrupole field with a line of zero magnetic field along the axis of symmetry. Along this axis, the atoms are free to move, resulting in an atomic beam. This beam is collimated using a larger radial field gradient than is typically found in 3D MOT systems. This increases the radial confinement of atoms.

A pinhole is placed at the exit of the cell to prevent atoms with a high radial velocity from exiting. This pinhole also greatly reduces the conductance between the 2D MOT cell and the main chamber, which means that a high rubidium partial pressure can be maintained in the 2D MOT cell, without greatly increasing the pressure in the main chamber. The pinhole is drilled into a silicon plate, which partially reflects the beam that propagates along the central axis. This creates an unbalanced molasses that cools atoms along the axial direction. The scattering rate from each beam is not equal, so the net force on the atoms pushes them through the pinhole. By slowing a larger proportion of atoms to within the capture velocity of the 3D MOT, this configuration, referred to as a 2D+ MOT, loads a 3D MOT faster than the 4-beam counterpart.

Figure 4.3 shows a schematic of the optical components used to generate the light

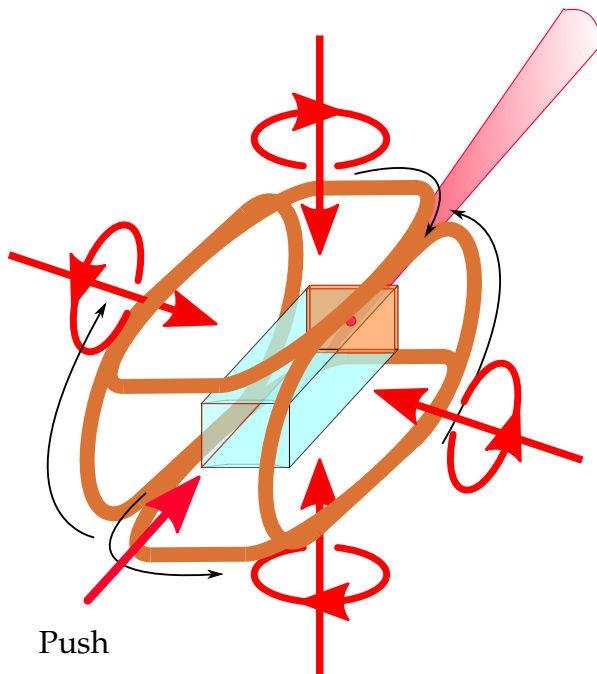


**Figure 4.2.: Schematic diagram for the 2D MOT.**  $^{87}\text{Rb}$  atoms are trapped and cooled along the 2 axes orthogonal to the long axis of the source cell. The black arrows indicate the direction of the current through each coil. Each circularly polarised beam drives  $\sigma^-$  transitions for an atom moving in the opposite direction. A linearly polarised push beam propagates along the longitudinal axis and is partially reflected by the silicon wafer at the opposite end. This provides a small amount of axial cooling and the imbalance of radiation pressure pushes atoms out of the cell. The pinhole at the other end prevents atoms with a high transverse velocity from leaving the cell.

for the 2D MOT. The cooling light enters from a single fibre, which is collimated to a beam waist of 9.5 mm using two aspheric lenses. This is linearly polarised and divided into two beams of equal power using a Half-wave Plate (HWP), one for each cooling axis. Each beam passes through a beam-splitter and a prism mirror, to increase the volume covered by the 2D MOT beams. A QWP circularly polarises the beam before it enters the ar-coated glass cell. On the opposing side of the cell, a 25 mm  $\times$  35 mm mirror retro-reflects the beam. This is coated with a layer of quartz to form a QWP, so that the reflected beam has the same polarisation handedness as the incoming.

The push beam enters from a second fibre input. A fixed focus collimator collimates the beam to a waist of 1.5 mm. This is mounted onto a 1 in kinematic mount to align the push beam to the 0.7 mm pinhole at the other end of the cell. The push beam is linearly polarised by a Polarising beam-splitter (PBS) to reduce the effect of polarisation drift on the axial cooling of the 2D MOT.

The cell, manufactured by ColdQuanta, has dimensions of 30 mm × 30 mm × 44 mm and is specifically designed for creating a 2D MOT. It contains two rubidium dispensers composed of rubidium chromate ( $\text{RbCrO}_4$ ) and a reducing agent. These were activated by passing a large current through them to remove a thin oxidation layer. To produce rubidium, a current of around 2.8 A is passed through the dispenser to trigger an electro-chemical reduction reaction, so that pure rubidium sublimates.

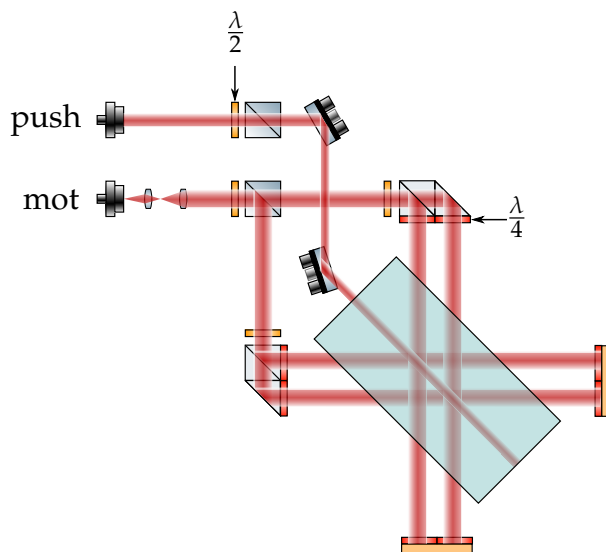


**Figure 4.3.:** Optical components for the 2D MOT. The light for the MOT is split into two equal portions using a HWP and PBS. Along each axis, the beam passes through a PBS and a prism mirror to increase its spatial extent. The beam is circularly polarised before entering the cell and retro-reflected by a mirror coated with a QWP. The push beam is collimated from another fibre input and linearly polarised before entering the cell along the longitudinal axis.

The cylindrical quadrupole field is generated by a set of coils that are manufactured by ColdQuanta. They are mounted so that the axis of zero magnetic field coincides with

the central longitudinal axis of the source cell. These produce a radial field gradient per current of  $20 \text{ G cm}^{-1} \text{ A}^{-1}$ . Figure 4.4 shows a simulation of the field gradient along each axis and the magnetic field in each plane of symmetry. Across the centre of the cell, the field gradient is very uniform. The equilibrium position where the MOT forms is adjusted using Helmholtz coil pairs along each MOT axis. These coils produce a field per current of  $1 \text{ G A}^{-1}$ .

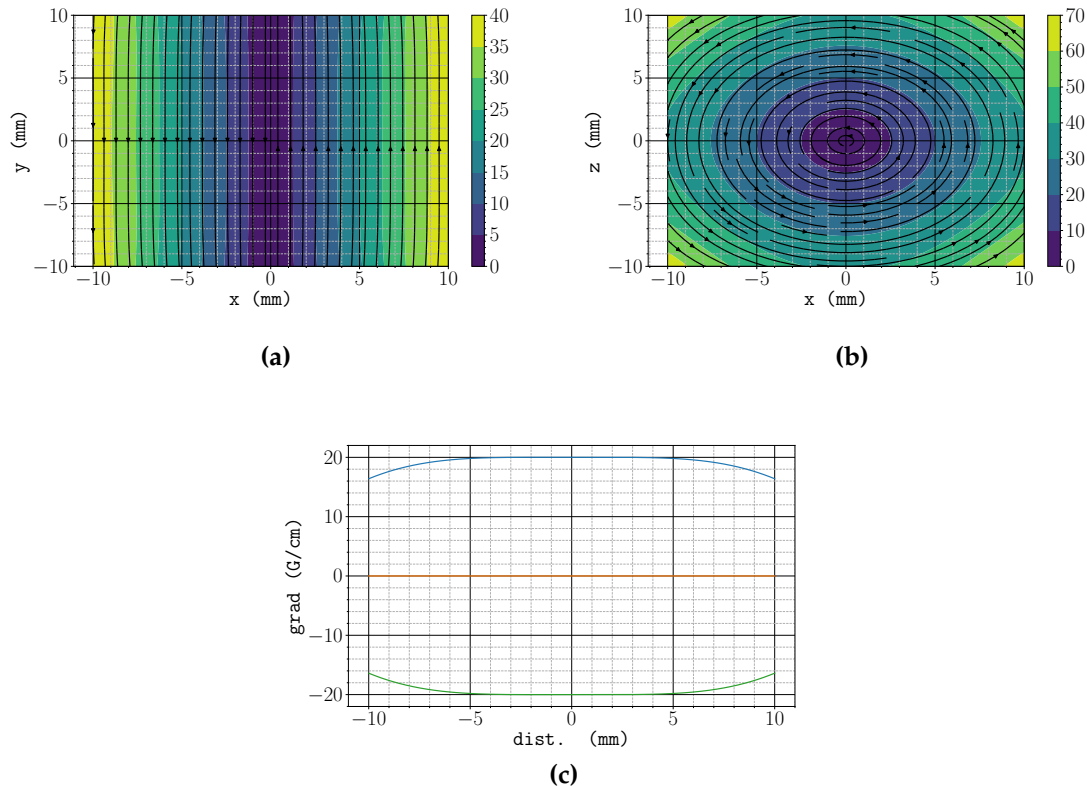


**Figure 4.4.**: Simulated field and field gradients for the 2D MOT quadrupole coils. In this coordinate system, the 2D MOT cools and traps atoms in the  $\vec{x}$  and  $\vec{z}$  directions. The simulation was performed using a nominal current of 1 A, which corresponds to a current density in each coil of  $7.78 \text{ A mm}^{-2}$ . The magnitude of the magnetic field (in units of G) and its direction in the axial and radial planes of symmetry are shown in (a) and (b), respectively. (c) shows the field gradient components  $\partial_x B_x$  (blue),  $\partial_y B_y$  (orange) and  $\partial_z B_z$  (green) along their corresponding axes.

### 4.2.2. The 3D MOT system

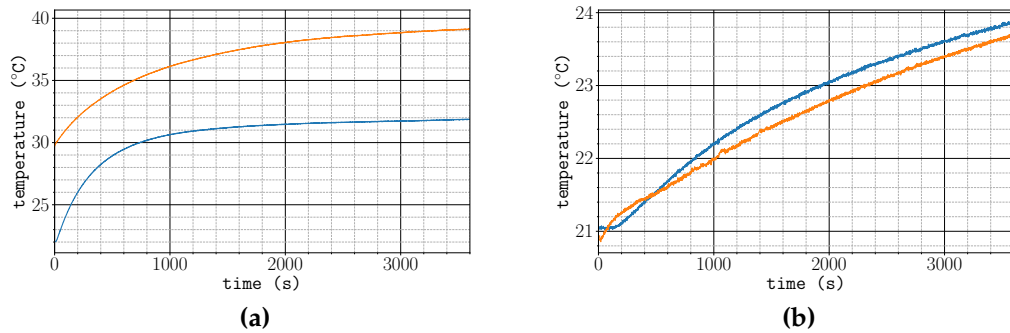
The main chamber contains the apparatus that is used to make a 3D MOT. Each MOT beam originates from a PM fibre and is collimated using a lens with a nominal focal length of 75 mm to a waist size of 7.5 mm. At the output of each collimator is a QWP, with its slow axis oriented at a  $45^\circ$  angle to either the fast or slow axis of the fibre, to produce either left- or right-handed circularly polarised light. The MOT beams along the axial direction of the quadrupole field (i.e. the  $\vec{z}$  direction) are orthogonally polarised to the others along the  $\vec{x}$  and  $\vec{y}$  directions. The MOT beams are aligned so that their intensities at the centre of the chamber are equal, so that the MOT forms where the magnetic field is zero.

#### Spherical quadrupole magnetic field

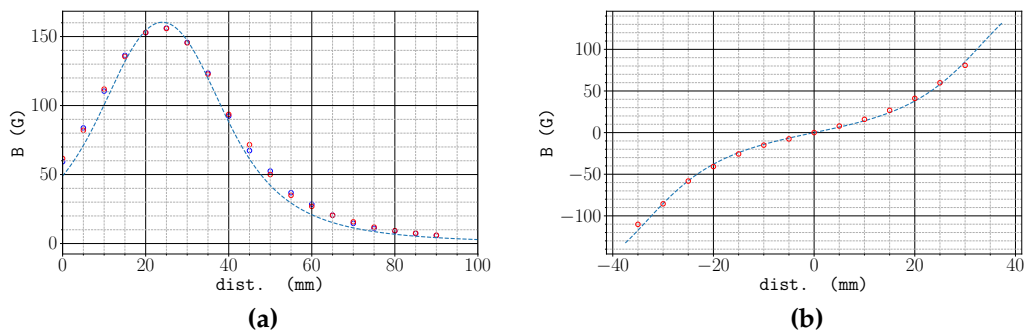
The magnetic field for the 3D MOT is created by a pair of coils in an anti-Helmholtz configuration. Each coil is wound using rectangular wire coated in a  $35\ \mu\text{m}$  thick layer of Pyre-M.L, a UHV-compatible polyamide which provides a layer of insulation between each loop. The wire has a cross-section of dimensions  $1.1\ \text{mm} \times 1.1\ \text{mm}$ , with 20 axial loops and 12 radial loops. The inner diameter of the coil is 25.4 mm, to allow for optical access of the  $\vec{z}$ -axis MOT beams, and the maximum diameter is 59.2 mm – small enough that the coil could be inserted into the chamber through the DN63 CF ports. The coils are mounted to the chamber using groove grabbers which clamp into grooves inside the wall of the DN40 ports. The coil formers increase the surface area in contact with the chamber, increasing the rate of heat dissipation from the coils.

Figure 4.5 shows the temperature rise during operation of the coils both at atmospheric pressure and inside the chamber. At a pressure of around  $1 \times 10^{-2}\ \text{mbar}$ , the temperature of the coils inside the chamber does not exceed  $40^\circ\text{C}$ . Once mounted, the distance

between the innermost loops is 70 mm. Figure ?? shows the magnetic field, measured using a Hall probe, along the axis of symmetry for each of the coils with a current of 2.53 A. Figure ?? shows the axial field measured when the coils are in anti-Helmholtz configuration. These are in close agreement with a simulation of the magnetic field. The simulated field in the axial and radial planes of symmetry are shown in Figure 4.7a and Figure 4.7b, respectively.



**Figure 4.5.:** Temperature rise due to the MOT coils over 1 hour of operation. The blue curves were measured when the coils were at atmosphere and the orange were measured under a rough vacuum around  $1 \times 10^{-2}$  mbar. (a) shows the temperature of the coils and (b) is the temperature of the exterior of the chamber.



**Figure 4.6.:** Measured magnetic field and field gradient for the 3D MOT coils. (a) shows the axial magnetic field for the two coils as measured using a Hall probe. (b) shows the field close to the centre when the coils are in an anti-Helmholtz configuration. The dashed lines indicate the axial field as calculated from the simulation shown in Figure 4.7.

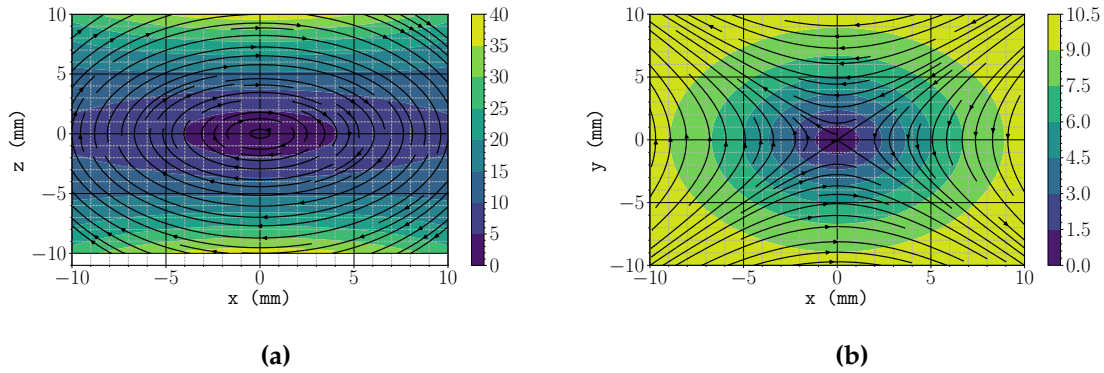


**Figure 4.7.:** Simulated magnetic field for the 3D MOT quadrupole coils. In this coordinate system, the axial direction is defined as the  $\vec{z}$  axis. The simulation was performed using a nominal current of 2.53 A, which corresponds to a current density in each coil of  $1.33 \text{ A mm}^{-2}$ . The magnitude of the magnetic field (in units of G) and its direction in the axial and radial planes of symmetry are shown in (a) and (b), respectively.

## Bias Coils

Three orthogonally arranged pairs of Helmholtz coils are used during the experiment to provide a homogeneous magnetic field close to the centre of the chamber. In the initial loading and molasses stages, these are used to zero the magnetic field at the centre of the chamber. This is required for effective sub-Doppler cooling . In subsequent stages, these coils provide a bias field along the appropriate axes during state preparation, interferometry and state detection. Each coil was wound using 1 mm thick wire and consisted of 5 axial and 10 radial turns. For a pair of coils in Helmholtz configuration, the magnetic field gradient at the centre is minimised when the axial separation  $a$  is equal to the coil radius  $r$ , but the geometry of the vacuum chamber meant that it was not possible to satisfy this condition. The radii and axial separations of each coil pair is presented in Table 4.1.

Axis	$a$ (mm)	$r_i$ (mm)	$r_o$ (mm)
$\vec{x}$	88	105	115
$\vec{y}$	132	178	188
$\vec{z}$	116	123	133

**Table 4.1.:** Table of parameters for each 3D MOT bias coil.  $a$  denotes the axial separation between each coil,  $r_i$  and  $r_o$  are the inner and outer radii.

### 4.2.3. CCD Imaging

During the experiment, atoms are imaged using a CCD camera to spatially resolve the cloud. This was done to measure the temperature using a ballistic expansion method and the trajectory of the cloud (see Section 5.2.4). Figure 4.8 shows a diagram of the apparatus used for imaging. A pair of 125 mm and 50 mm focal length lenses are used to image the cloud onto a Pike F505-B CCD camera. The camera has a maximum resolution of  $2452 \times 2054$  pixels. A measurement of the magnification of a ruler gave a calibration factor of 7.065(70) pixel/mm. To reduce the level of background light on the CCD, a bandpass filter is placed in front of the sensor. This transmits 780 nm light at an efficiency of 60%.

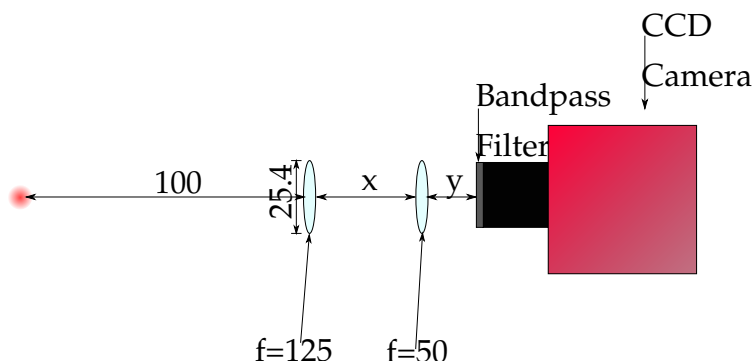


**Figure 4.8.:** Optical setup for CCD imaging. Two lenses are used to magnify the image of the atom cloud on the CCD. A bandpass filter is placed in front of the sensor to block out background light at wavelengths other than 780 nm. All lengths are given in millimetres.

## Incident Optical Power Calibration

Measuring the incident optical power is useful for estimating the number of atoms  $N_a$  by measuring the amount of light emitted during resonance fluorescence. However, typical number densities in a MOT mean that incident light is strongly absorbed by atoms close to the surface. Consequently, the assumption of a constant scattering rate per atom is not valid and leads to an under-estimate of the atom number. More accurate techniques such as absorption imaging can be used, but for the purposes of this experiment, it was sufficient to use fluorescence imaging as a rough estimate of the number of atoms in the MOT. In subsequent stages of the experiment, a sensitive photodiode with a high bandwidth was used to detect the atoms in each hyperfine ground state. Details on this setup can be found in Section 7.3.2.

Under the assumption that the power radiated per atom is constant, the power incident on the CCD  $P_{\text{ccd}}$  can be related to the scattering rate per atom as follows

$$P_{\text{ccd}} = \frac{\Omega}{4\pi} t R_{\text{sc}} \hbar \omega N_a \quad (4.1)$$

where  $\Omega/4\pi = 1.8 \times 10^{-3}$  is the fractional solid angle subtended by the imaging optics,  $t$  is the transmission of the bandpass filter and  $\hbar \omega = 1.6 \text{ eV}$  is the emitted photon energy. For a two-level system, the scattering rate  $R_{\text{sc}}$  is

$$R_{\text{sc}} = \frac{\Gamma}{2} \frac{s}{1 + s + \left(\frac{2\delta}{\Gamma}\right)^2} \quad (4.2)$$

where  $\Gamma$  is the natural linewidth of the transition,  $\delta$  is the frequency detuning and  $s = I/I_{\text{sat}}$  is the saturation parameter. This incident power is then related to the

integrated number of pixel counts  $C_{\text{int}}$  by

$$C_{\text{int}} = \alpha \tau_{\text{exp}} \eta P_{\text{ccd}} \quad (4.3)$$

where  $\tau_{\text{exp}}$  is the exposure time,  $\eta = 0.14$  is the quantum efficiency of the CCD and  $\alpha$  is a scaling factor that relates the total charge collected to the total number of pixel counts. By varying the exposure time used to image a collimated beam with a total power of  $0.17 \mu\text{W}$ , the total number of counts recorded by the camera as a function of exposure time is plotted in Figure 4.9. This gives a count scaling factor of  $\alpha = 2.2 \times 10^5 \text{ counts } \mu\text{s}^{-1} \mu\text{W}^{-1}$ .

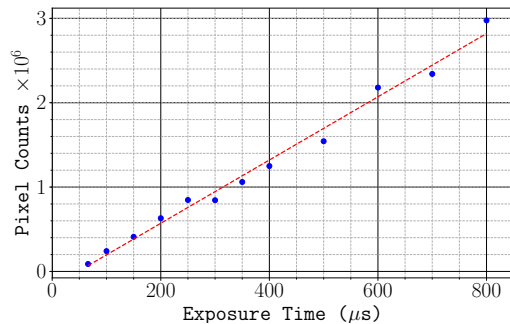


**Figure 4.9.:** Integrated pixel counts as a function of CCD exposure time for an incident optical power of  $0.17 \mu\text{W}$ . The dashed line indicates a linear regression which gives a scaling factor of  $\alpha = 2.2 \times 10^5 \text{ counts } \mu\text{s}^{-1} \mu\text{W}^{-1}$ .

### 4.3. Generating MOT light

All the MOT light in this experiment was generated by the  $\mu$ Quans laser [28].  $\mu$ Quans is a French laser company that is a spin-off from the Institut d'Optique and Observatoire de Paris. A schematic of this laser system is shown in Figure 4.10. The light is fibre-coupled to minimise the number of free-space optical components. This makes the system more stable in the presence of vibrations and temperature variations. The

$\mu$ Quans laser is comprised of four 1560 nm External-Cavity Diode Lasers (ECDLs) which are frequency-doubled to produce light at 780 nm. The first acts as a master laser which is locked to the  $|F = 3\rangle \rightarrow |F' = 3, 4\rangle$  crossover point in **rb85!** (**rb85!**) to serve as an absolute frequency reference. The other three slave lasers are used for output. The first one provides light for cooling  $^{87}\text{Rb}$  using the  $|F = 2\rangle \rightarrow |F' = 3\rangle$  transition. Light for the  $|F = 1\rangle \rightarrow |F' = 2\rangle$  repump transition is created by phase modulating this laser using an Electro-optic Modulator (**EOM**). The other two make up a pair of lasers for driving Raman transitions. One laser is frequency-offset locked to the master and the other is phase-locked to the first. This Raman laser was not used in this experiment, so will not be discussed in further detail. The power in each of these slave lasers is amplified using an Erbium-Doped Fibre Amplifier (**EDFA**). The frequency is doubled to around 780 nm using a Periodically-Poled Lithium Niobate (**PPLN**). The output power is controlled using an **AOM**.

#### 4.3.1. Absolute Frequency Reference

The master laser provides an absolute frequency to which the slave lasers are offset-locked. The reference frequency is created using saturated absorption spectroscopy inside a Rubidium vapour cell. The sub-Doppler features in this spectrum are insensitive to temperature changes, and under have linewidths closer to the natural linewidth of Rubidium ( $\Gamma \sim 2\pi \times 6$  MHz). Figure 4.11 shows the saturated absorption spectrum using the  $\mu$ Quans master laser. The frequency is varied by finely adjusting the temperature of the master **ECDL**. The master laser is set to lock to the crossover resonance between the  $F = 3 \rightarrow F' = 3$  and  $F = 3 \rightarrow F' = 4$  transitions in **rb85!** (indicated as **(b)**), which is the strongest feature in the spectrum. This absorption feature is around 1.1 GHz below the cooling transition in  $^{87}\text{Rb}$  (indicated as **(a)**). The frequency of the laser is modulated by modulating the current to the **ECDL**. This

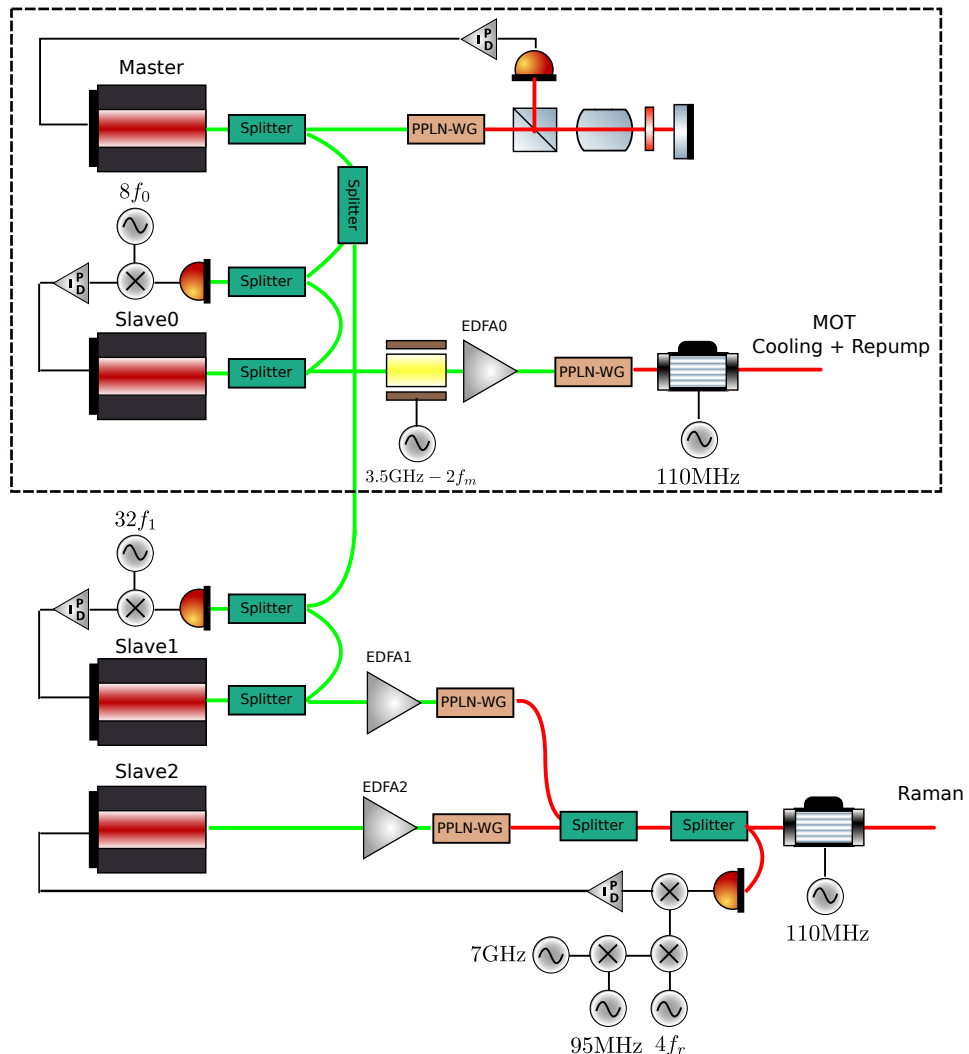


**Figure 4.10.:** Schematic of the  $\mu$ Quans laser system. Each output laser is derived from a 1560 nm ECDL (shown in green) which is amplified using an EDFA and then frequency-doubled to 780 nm using a PPLN crystal. A master laser is locked to the 3,4 crossover in rb85! and the output lasers are offset-locked to their corresponding frequencies. The dashed region indicates the components used for generating light for the MOTs, which was the only function of this laser for this experiment.

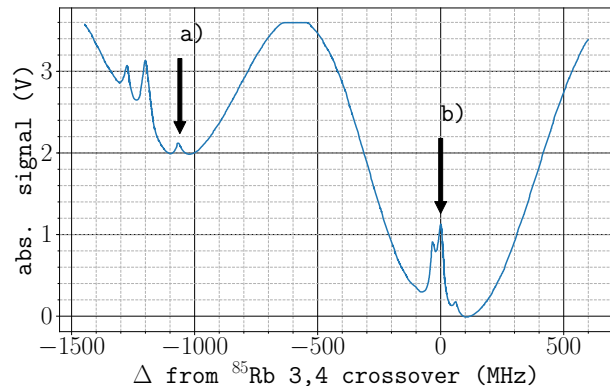


**Figure 4.11.:** Saturated absorption spectroscopy using the Rubidium vapour cell in the  $\mu$ Quans laser. The absorption features indicated are *a*: the  $F = 2 \rightarrow F' = 3$  transition in  $^{87}\text{Rb}$  and *b*: the crossover resonance between the  $F = 3 \rightarrow F' = 3$  and  $F = 3 \rightarrow F' = 4$  transitions in  $\text{rb85}!$  which is used to lock the frequency of the master laser.

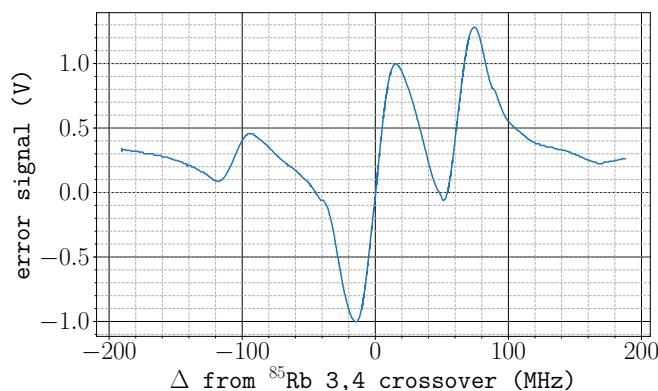


**Figure 4.12.:** Error signal obtained by modulating the laser current. Close to the lock point, the signal is approximately linear. This signal is used in a feed-back loop to correct for frequency changes of the master laser.

produces a signal that is proportional to the frequency difference from the lock point. The error signal shown in Figure 4.12 is obtained by demodulating the absorption signal using a lock-in amplifier. The servo that controls the master laser frequency also contains an integrator to compensate for long-term drifts arising from temperature variations.

### 4.3.2. Cooling and Repump Light

The first of the slave lasers provides light to address the cooling transition. This is frequency-offset locked to the master by comparing their beat frequency to a reference from a DDS. A plot of the error signal used to lock this offset frequency is shown in Figure 4.13.

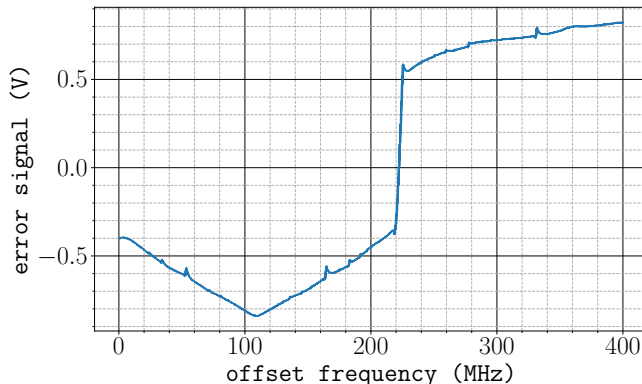


**Figure 4.13.:** Error signal for the  $\mu$ Quans cooling laser, plotted as a frequency difference from the start of the scan. This is obtained by comparing the beat frequency between the master and slave lasers to a reference frequency generated by a DDS. A servo loop feeds-back onto the frequency of the slave laser to keep this difference close to zero.

An EOM modulates the phase of the cooling laser to produce light for the  $|F = 1\rangle \rightarrow |F' = 2\rangle$  repump transition. This modulation creates frequency sidebands separated by integer multiples of the modulation frequency  $f_m$ . If the amplitude of the modulation is small, only the first positive and negative sidebands are present. A separate DDS

provides the reference for the modulation frequency, so that the frequency of the cooling and repump light can be independently ramped during the experiment (see Section 4.3.3). This is amplified, doubled and subtracted from a 3.5 GHz reference signal so that the positive frequency sideband is approximately 6.6 GHz above that of the cooling light, to address the repump transition. The modulation power is externally controlled using a Voltage-Controlled Attenuator (**VCA**) to control the ratio of repump power to cooling power. An RF switch turns the repump on and off by blocking the reference frequency.

The total output power is controlled using an **AOM** that has a fixed modulation frequency of 110 MHz. Figure 4.14 shows the combined power of the cooling light for the 3D **MOT** as a function of the control voltage to the **AOM** RF power. The hardware used to divide the light from the laser to the separate beams is described in Section 4.4.1.

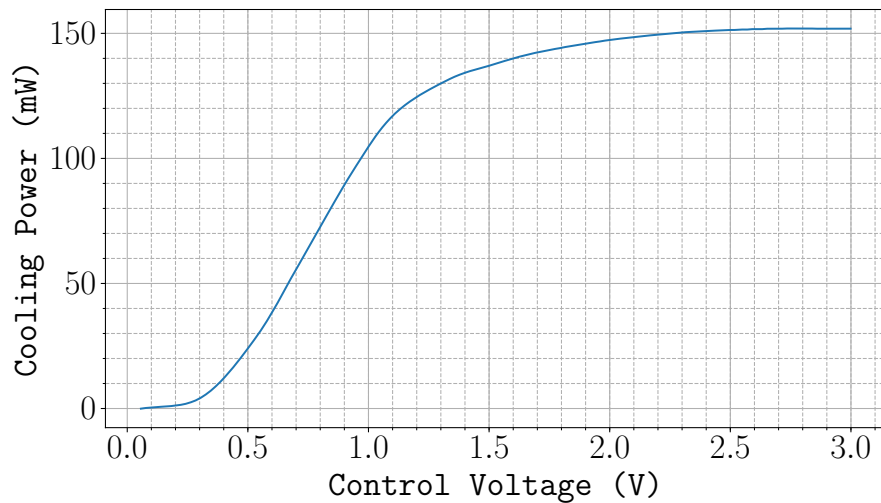


**Figure 4.14.:** Combined 3D **MOT** cooling power as a function of control voltage for the RF power that drives the  $\mu$ Quans output **AOM**.

### 4.3.3. Real-Time Control

During the experiment, it is necessary to vary the frequency and power of both the cooling and repump light. Analogue and digital signals control the RF sources for the output **AOM** and **EOM**. A **DDS** generates each RF frequency, so that they can be updated in real-time. These are also programmed to ramp the output frequency for a specified duration and ramp rate. This is done by sending serial messages to an application which interprets the message and synchronously communicates the command to the **DDS** using Serial Programming Interface (**SPI**). A glossary of the messages and their function is given in Appendix [A](#). The command is stored in memory on-board the **DDS** and is triggered to start using a digital pulse. This means that time at which the frequency of the light changes is synchronised with the rest of the experiment.

## 4.4. Controlling the MOTs

Effective trapping and cooling of Rubidium requires careful control of the light and magnetic fields used to create the **MOT**. A well-balanced **MOT** requires circularly polarised beams with equal intensities so that there is no net force from scattering light. Otherwise, the **MOT** forms at a position where the magnetic field is not zero [29]. Equivalently, the **MOT** requires good control of the magnetic field inside the chamber. What follows is a description of the hardware used to implement this control. Section [4.4.1](#) describes the network of optical fibres used to control the frequency and power in each **MOT** beam. The electrical circuits used to control the strength of each bias field, as well as switching off the quadrupole coils, are described in Section [4.4.2](#).

#### 4.4.1. Optical Fibre Network

A network of fibre-based beam-splitters and AOMs distributes the light from the  $\mu$ Quans fibre to each of the beams for the 2D and 3D MOTs. This provides independent control of the power and frequency of the light at each output of the fibre network. A diagram of this setup is shown in Figure 4.15. The  $\mu$ Quans fibre output is polarised using a polarising beam-splitter before a HWP aligns it with the slow axis of a PM fibre. The light is first divided on a 1:2 beam-splitter, with 66% exiting one port, used for the 3D MOT. The 34% on the other port is split again using another 1:2 beam-splitter so that 95% and 5% of the power exits each port, for the 2D MOT and push beam, respectively. Independent control each output is done using a *Gooch and Housego* fibre AOMs with a central modulation frequency of 135 MHz. The junctions between components are spliced together to minimise insertion loss. The slow axes of each fibre are aligned so that the polarisation of the input light is maintained.

The light for the 3D MOT is split using a 1:3 splitter into pairs of outputs for the light along the  $\vec{x}$ ,  $\vec{y}$  and  $\vec{z}$  axes. Unlike the outputs along the other axes, the ones used for light along the  $\vec{z}$  axis have separate AOMs. This is done so that during the experiment, a single beam along the  $\vec{z}$  axis can be used to blow away background atoms (see Section 5.3.4 for more details).

#### 4.4.2. Magnetic Field Control

The current through each set of bias coils (3 for the 3D MOT and 2 for the 2D MOT) is controlled using a voltage-controlled current source. The control voltage is an input at the non-inverting terminal of an OPA549 op-amp. The coils are placed in series with a sense resistor of resistance  $R_s$  at the output. The circuit is configured so that the voltage at the inverting terminal is  $V_- = iR_s$ . This forms a negative feed-back loop to

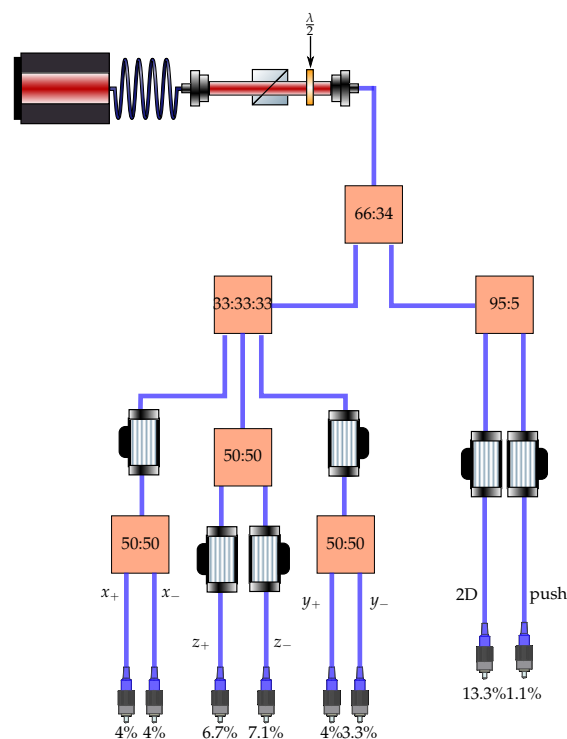


**Figure 4.15.:** Fibre splitter and AOMs for MOT light distribution. The polarisation of the cooling and repump light from the  $\mu$ Quans laser is aligned to the fibre network using a PBS and HWP. Apart from the outputs for the  $\vec{x}$  and  $\vec{y}$  3D MOT beams, which have a single AOM per axis, the power and frequency at each output can be controlled independently. The percentages shown are the relative power at each output, accounting for insertion loss and driving each AOM with the optimum RF power.

keep the output current constant if the load resistance changes. The bias coils can be supplied with up to 2 A using a control voltage of 10 V.

This same circuit is used to control the 3D MOT coils, except for the fact that their larger resistance necessitates a larger gain to achieve the current necessary to produce a strong field gradient. During the experiment, the 3D MOT coils need to be switched off rapidly, to allow for effective sub-Doppler cooling of the atoms. The coils are an inductive load, so the time taken for the current to decay is determined by the time constant  $\tau = L/R$ . With a negative voltage across them, the stored energy (and hence, magnetic field) dissipates at a faster rate. A flux-gate magnetometer was used to measure the time taken to switch off the coils. With an applied voltage of 0 V, the characteristic decay time is  $\tau = 2.5 \text{ ms}$ . Under the maximum available back-EMF of  $-24 \text{ V}$ , the field can be completely switched off in  $800 \mu\text{s}$ .

The quadrupole coils for the 2D MOT are switched off in much the same way. An IGBT cuts the flow of current when the gate voltage drops below a threshold value. To prevent damage to the transistor, a diode and  $10 \Omega$  power resistor are placed in parallel with the coils. This allows the current generated by the back-EMF to dissipate without damaging the IGBT. These fields from these coils can be switched off in less than 1 ms.

## 4.5. Characterising the MOTs

This section discusses the performance of the 2D and 3D MOTs for trapping and cooling  $^{87}\text{Rb}$ . The main goal of this stage of the experiment is to quickly produce an ensemble of trapped, cold atoms in the 3D MOT. For this reason, the loading rate of the 3D MOT is a useful figure-of-merit. As further cooling in an optical molasses is

necessary to achieve a sufficiently cold ensemble for interferometry (see Section 5.2), the temperature of atoms in the MOT will not be discussed in detail.

At the start of the experiment, the light and magnetic fields to produce the 2D and 3D MOTs are switched on. Table 4.2 shows typical values for the cooling and repump power, as well as the field gradients and bias fields used. The cooling light is detuned by  $-2\Gamma$  from the  $|F = 2\rangle \rightarrow |F' = 3\rangle$  transition for the 2D MOT and by  $-2.5\Gamma$  for the 3D MOT. The push beam is at resonance. A timing diagram of the loading sequence is given in Figure 4.16. The light and magnetic fields for the 2D MOT are switched off after 100 ms and the 3D MOT is kept on for a further 50 ms to allow for the transit of the remaining atoms from the 2D MOT to the 3D MOT. After a sufficient number of atoms are loaded, the experiment proceeds by switching off the 3D quadrupole field prior to cooling in an optical molasses.

2D MOT			3D MOT				
Laser Power		Magnetic Field	Laser Power		Magnetic Field		
Cooling	60 mW	$d\vec{B}/d\rho$	18 G cm $^{-1}$	Cooling	130 mW	$d\vec{B}/dz$	15 G cm $^{-1}$
Repump	6 mW	$B_x$	0.48 G	Repump	13 mW	$B_x$	1 G
Push	500 $\mu$ W	$B_y$	-0.46 G			$B_y$	-0.5 G
						$B_z$	0.22 G

**Table 4.2.:** Typical optical and magnetic parameters used for the 2D and 3D MOTs. The optical powers listed are the total used for each MOT, which is divided into separate beams. The bias field strengths are the values used during the preliminary trapping stage of the experiment. The specified field gradients are given along the radial direction and the symmetry axis of the quadrupole coils for the 2D and 3D MOTs, respectively.

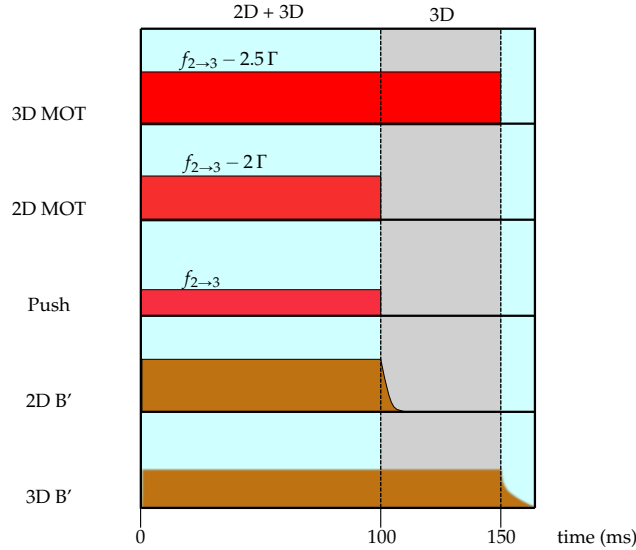


**Figure 4.16.:** Timing diagram for the loading stage of the experiment. The 2D MOT is switched on for 100 ms and is switched off earlier than the 3D MOT.

#### 4.5.1. 3D MOT Loading Rate

The loading rate of the 3D MOT from a beam of atoms originating from the 2D MOT can be understood using the following rate equation

$$\frac{dN}{dt} = R\phi_{rb} - (\alpha\phi_{rb} + \beta n_{bg}) N - \gamma N^2 \quad (4.4)$$

where  $\phi_{rb}$  is the flux of rubidium through 3D MOT capture volume and  $R$  describes the rate at which rubidium is cooled and trapped such that  $R\phi_{rb}$  is the loading rate of the 3D MOT. The second term describes a loss rate due to collisions between trapped atoms and untrapped rubidium and background atoms. These loss rates are parameterised by  $\alpha$  and  $\beta$ , respectively. The final term describes the loss of atoms from the trap due to intra-trap collisions [30] which depends on the density of atoms in the trap. In the case of a large flux of atoms from the 2D MOT the first two terms

dominate, leading to a simple solution for the number of atoms in the 3D MOT

$$N(t) = \frac{R\phi_{rb} \left(1 - e^{-t(\beta n_{bg} + \alpha\phi_{rb})}\right)}{\beta n_{bg} + \alpha\phi_{rb}} \quad (4.5)$$

which has a steady-state atom number given by

$$N_\infty = \frac{R\phi_{rb}}{\beta n_{bg} + \alpha\phi_{rb}} \quad (4.6)$$

Under a small atomic flux, both the loading rate and steady-state atom number increase as the flux of atoms from the 2D MOT increases. Once this flux is great enough, the loss due to background atom collisions is small compared to the loss due to rubidium collisions and the final number is independent of  $\phi_{rb}$ .

The flux of atoms from the 2D MOT depends on the 2D MOT loading rate, which in turn depends on the capture volume and rubidium number density inside the cell. Without any longitudinal cooling, a significant fraction of atoms leaving the cell will have a velocity greater than the 3D MOT capture velocity [31].

The effect of varying the partial pressure of rubidium inside the source cell is shown in Figure 4.17. The number of atoms in the 3D MOT was measured over time for a range of dispenser currents. At low partial pressures, the loading rate increases due to the increase in the flux from the 2D MOT. As the pressure increases, the increasing flux gives a larger steady-state number of atoms, up until the background pressure becomes negligible. Figure 4.17a and Figure 4.17b compare the loading curves observed with and without the push beam. Below a threshold pressure, the push beam greatly improves the loading rate since a greater fraction of the atoms can be captured in the 3D MOT.

Figure 4.17c shows the fitted loading rate for each scenario. There is a clear optimum pressure, where the loading rate is  $2.4 \times 10^9 \text{ s}^{-1}$ . The steady-state atom number is independent of the flux from the 2D MOT. Above this pressure, the loading rate is sharply reduced. The increased collision rate between cold atoms from the 2D MOT and hot untrapped ones reduces the atomic flux. This also increases the mean velocity of atoms in the beam, since faster ones are less likely to collide with a background atom before exiting the cell. At very high pressures, the mean velocity is so great that only a small fraction of atoms can be captured and the push beam has little effect on the loading rate.

## 4.6. Conclusion

This chapter has introduced the components of the experiment that were used to trap and cool atoms in a MOT. This is used to prepare an ensemble of cold atoms in a pure quantum state, suitable for interferometry. An optimisation of the loading rate of the 3D MOT was carried out to reduce the dead time between consecutive experiment cycles.

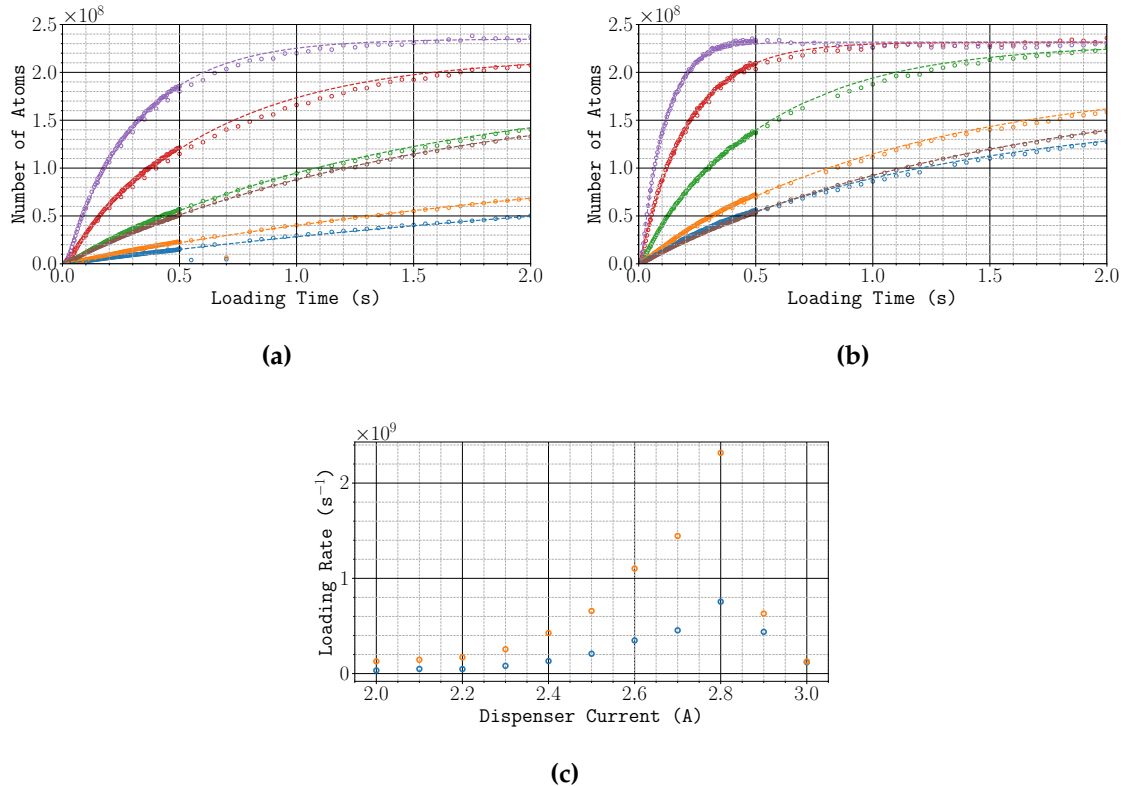


**Figure 4.17.**: Number of atoms in the 3D MOT over time for a range of dispenser currents. For clarity, only the loading curves for dispenser currents of 2 A (blue), 2.2 A (orange), 2.4 A (green), 2.6 A (red), 2.8 A (purple) and 3 A (brown) are shown in (a) and (b), which present the number of atoms over time without and with a push beam, respectively. The loading rate ( $R \phi_{\text{rb}}$  in equation (4.4)) in both instances is shown in (c). As the partial pressure of rubidium increases, the flux of atoms from the source cell increases. By longitudinally cooling the atoms, the push beam enhances the loading rate of the 3D MOT. Above a dispenser current of 2.8 A, the collision rate with hot untrapped atoms greatly reduces the atom flux, reducing both the loading rate and steady-state atom number.

# Chapter 5.

## Preparing Atoms for Interferometry

### 5.1. Chapter Overview

This chapter presents the stages of the experiment which prepare an ensemble of atoms for interferometry, after they are loaded into the 3D MOT. After being released from the trap, the atoms are cooled and launched using a moving molasses, as described in Section 5.2. Following this, a sequence of optical and microwaves pulses are used to increase the population in the  $|1,0\rangle$  ground state and end with an ensemble which has a narrow velocity spread along the Raman axis. A characterisation of this is given in Section 5.3.

Some sections of this chapter refer to parts of the experiment which have yet to be introduced. Details on the Raman laser and the velocity-selective Raman pulse can be found in Section 7.2 and Section 7.4.3, respectively. A description of the detection scheme, used to measure the population of atoms in  $|F = 1\rangle$  and  $|F = 2\rangle$  is presented in Section 7.3.

## 5.2. Cooling in Optical Molasses

**Introduce motivation here** A low thermal velocity means that the atoms can be interrogated for a longer time and in the case of atom interferometry, leads to a more sensitive measurement of acceleration. In addition, the thermal expansion of the ensemble leads to greater systematic phase shifts due to effects such as magnetic field gradients and laser wavefront distortions. The temperature of atoms inside the MOT is greater than desired, so further cooling is required before a strong interferometer signal can be achieved. Temperatures well below that of the Doppler limit ( $146 \mu\text{K}$  for  $^{87}\text{Rb}$ ) can be reached using the dissipative force that acts on an atom travelling through a spatially varying electric field.

This section describes the work towards to cooling and launching the atoms in a moving optical molasses. It starts with a motivation for launching the atoms in Section 5.2.1. The following section discusses the control of the intensity and frequency of the light during the molasses stage of the experiment. A description of the techniques needed to cool the atoms in a moving molasses is then given in Section 5.2.3. Finally, this section concludes in Section 5.2.4 with measurements of both the temperature and trajectory of the atom cloud which were measured using a ballistic expansion method.

### 5.2.1. Motivation for Launching

As previously discussed in Section 2.4.3, there are two pairs of counter-propagating beams which can drive Raman transitions between the two hyperfine ground states. If an atom can be stimulated by both pairs, then the additional trajectories this introduces do not interfere, resulting in a reduction in the fringe visibility. This problem can be avoided by using the fact that the Raman transition is Doppler-sensitive to ensure that the atoms are only driven by one pair of beams. Each pair has an opposite

Doppler shift  $\pm\omega_D = \pm\mathbf{k}_{\text{eff}} \cdot \mathbf{v}$  and so their transition frequencies are separated by  $2\omega_D$ . Therefore, the atoms are launched so that their centre-of-mass velocity along the Raman axis is large enough to lift the degeneracy of the two Raman transitions.

### 5.2.2. Frequency and Power Control

A timing diagram illustrating the power and frequency during this stage of the experiment is shown in Figure 5.1. After the atoms are loaded into the MOT, they are released by switching off the quadrupole field. Once this field has decayed away, the frequency and intensity of the cooling light are ramped adiabatically. The frequency of the cooling light is ramped to  $-25\Gamma$  over 1.4 ms. Since the repump light is generated using an EOM, the modulation frequency is simultaneously ramped up to keep this light resonant with the  $|F = 1\rangle \rightarrow |F' = 2\rangle$  transition. Additionally, the relative detuning of counter-propagating MOT beams is varied so that the atoms are cooled into a moving molasses (see Section 5.2.3). After this, the intensity of the light is reduced over 5 ms. The response of the output AOM on the  $\mu$ Quans laser was calibrated so that we could apply a voltage ramp that gives an approximately linear intensity ramp.

### 5.2.3. Launching in a Moving Molasses

The configuration for launching atoms along the Raman axis is shown in Figure 5.2. The forward-propagating beams are blue-detuned by  $+\delta_l$  and the backward-propagating ones are red-detuned by  $-\delta_l$ , so that atoms with a velocity along the beam axis of  $\vec{v} = \delta_l \lambda$  are+ resonant with both beams. The frequency of each beam is ramped from the initial value by varying the modulation frequency of its AOM. This ramp occurs slowly to ensure the atoms are adiabatically accelerated to the resonant velocity, minimising excess heating of the atoms. As there is no pair of MOT beams along the axis

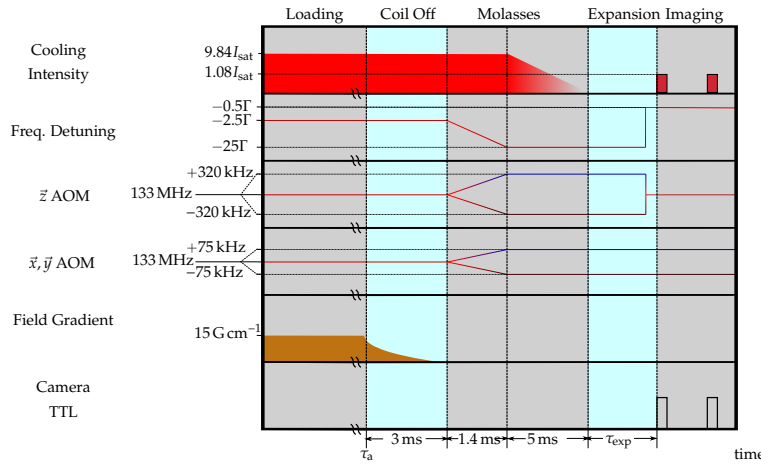


**Figure 5.1.:** Timing diagram for the molasses stage of the experiment. After a time  $\tau_a = 100$  ms, the atoms are released from the MOT. The molasses sequence begins 3 ms later, once the magnetic field from the MOT coils has decayed away. First, the frequency of the cooling light is ramped to  $-25\Gamma$  over 1.4 ms. The relative frequencies of counter-propagating MOT beams are detuned so that the atoms are cooled in a moving frame, launching them along a parabolic path (see Section 5.2.3). Next, the intensity of the MOT light is reduced linearly over 5 ms. To measure the temperature, the atoms are left to expand for a duration of  $\tau_{\text{exp}}$  ms, after which they are imaged using the camera.

of the Raman beams, the  $\vec{x}$  and  $\vec{y}$  MOT beams, whose axes are nominally at  $45^\circ$  to the Raman axis, are used to launch the atoms. By controlling the power and alignment of each beam, the net velocity on the atoms will be along the Raman axis. If the detuning of both pairs of beams is the same, then the velocity along the Raman axis is given by  $\vec{v}_r = \sqrt{2}\delta_l\lambda$ .

As well as launching the atoms horizontally, the atoms are launched vertically so that they do not fall as far under gravity. Since the atoms remain close to the centre of the beam, where the intensity across the cloud is more uniform, longer pulse separation times can be used before the intensity gradient causes a significant dephasing. This launch is carried out using the MOT beams that lie along the vertical  $\vec{z}$  axis.

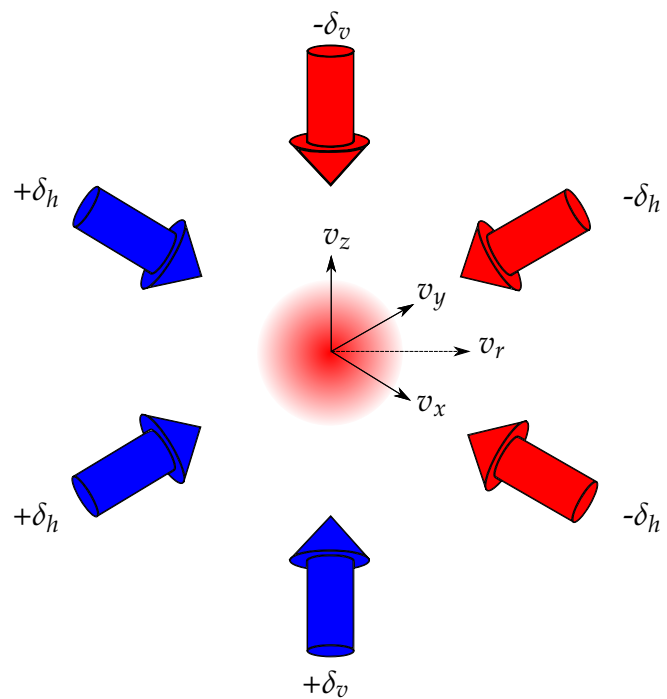


**Figure 5.2.:** Beam configuration for a moving molasses. When counter-propagating beams are detuned from each other, the atoms are slowed to a velocity which balances the frequency of each beam. Along the vertical axis, the beams are detuned by  $\delta_v$  so that the cloud is launched upwards with a velocity  $v_z = \delta_v \lambda$ . In the horizontal plane, the  $\vec{x}$  and  $\vec{y}$  beams are detuned by  $\delta_h$  so that the resultant velocity is along the Raman axis  $v_r = \sqrt{2} \delta_h \lambda$ .

### 5.2.4. Imaging the Atom Cloud over Time

Once released from the trap, the atom cloud is free to expand. Provided that there are no external forces on the atoms from electric or magnetic fields, the expansion of the cloud is determined by its thermal velocity distribution. In addition to this, the centre-of-mass moves due to its initial velocity and acceleration due to gravity. For the purposes of this discussion, it is worthwhile to consider the motion of atoms within the ensemble separately to the centre-of-mass motion as these provide a means of measuring the temperature and launch velocity, respectively. These were measured by imaging the distribution of atoms after allowing the cloud to expand in the dark for a range of expansion times. A typical atom cloud trajectory is shown in Figure 5.3, in which the cloud was imaged up to 76 ms after being released from the trap.

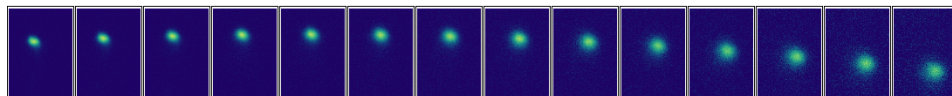


**Figure 5.3.:** A series of images showing the trajectory of the atom cloud after being cooled in a moving molasses. The first image was taken 7 ms after initiating the molasses and a subsequent one every 5 ms. Each image represents a region of interest of dimensions  $1150 \times 1650$  pixels that covers the spatial extent of the atom cloud during the launch.

### Measuring the Temperature

In thermal equilibrium, the velocity distribution of the atoms is described by a Maxwell-Boltzmann distribution

$$f(v_x, v_y, v_z) = \left( \frac{m}{2\pi k_B} \right)^{3/2} e^{-\frac{m(v_x^2 + v_y^2 + v_z^2)}{2k_B T}} \quad (5.1)$$

where  $v'_i = v_i - \langle v_i \rangle$  is the difference from the average velocity. Along a single axis, the velocity distribution is obtained by integrating over the other velocity components. For the sake of notation, the following discussion uses  $x$  and  $v_x$  as labels for position

and velocity, but these are interchangeable with the equivalent components along the other axes. As equation (5.1) is a product of velocity distributions along each axis, the velocity distribution along one axis is

$$f(v_x) = \left( \frac{m}{2\pi k_B} \right)^{1/2} e^{-\frac{m(v_x - \langle v_x \rangle)^2}{2k_B T}} \quad (5.2)$$

Suppose that there are initially  $n_0(x)dx$  atoms within the region  $(x, x + dx)$ , where  $n_0(x) = n(x, t = t_0)$  is the initial atomic density along one axis. During ballistic expansion, the atoms redistribute themselves according to their velocity. After a time  $t$  of free expansion, the position of an atom initially at  $x$  is  $x + v_x t$ . Assuming that the number density is initially a Gaussian, with a peak number density  $n_0(x_0)$  at the centre-of-mass, the number density at later times is given by a convolution with equation (5.2)

$$n(x, t) = \int n_0(x_0) \left( \frac{m}{2\pi k_B} \right)^{1/2} e^{-\frac{m(v_x - \langle v_x \rangle)^2}{2k_B T}} e^{-\frac{(x + v_x t - x_0)^2}{2\sigma_0^2}} dv_x \quad (5.3)$$

where  $\sigma_0$  is the  $1/e^2$  initial width of the cloud. As a convolution of two Gaussians, equation (5.3) is also a Gaussian, with a  $1/e^2$  width given by

$$\sigma(t)^2 = \sigma_0^2 + \frac{k_B T}{m} t^2 \quad (5.4)$$

Figure 5.4 shows a typical density profile along each axis, obtained by imaging the cloud on a camera, as previously described in Section 4.2.3. The width along each axis is estimated using a non-linear least squares fit to equation (5.3). Figure 5.5 shows the measured cloud width over a range of expansion times. For the purposes of measuring the temperature, the total atom number and the initial cloud size are not important, so no attempt was made to estimate these. The initial measurement was made 7 ms after the end of the molasses to allow for enough time to re-lock the laser to  $-0.5\Gamma$

below the  $|F = 2\rangle \rightarrow |F' = 3\rangle$  transition and align the bias field to the  $\vec{z}$  axis so that the atoms could be optically pumped into the  $|2, 2\rangle$  state. The width of the cloud along each axis is estimated using a non-linear least squares fit to equation (5.3). Then, a least squares linear fit estimates the temperature along each axis from the gradient, as per equation (5.4). The measured temperature along the horizontal and vertical axes of the camera was  $T_x = 6.38(11) \mu\text{K}$  and  $T_y = 6.38(9) \mu\text{K}$ , respectively.

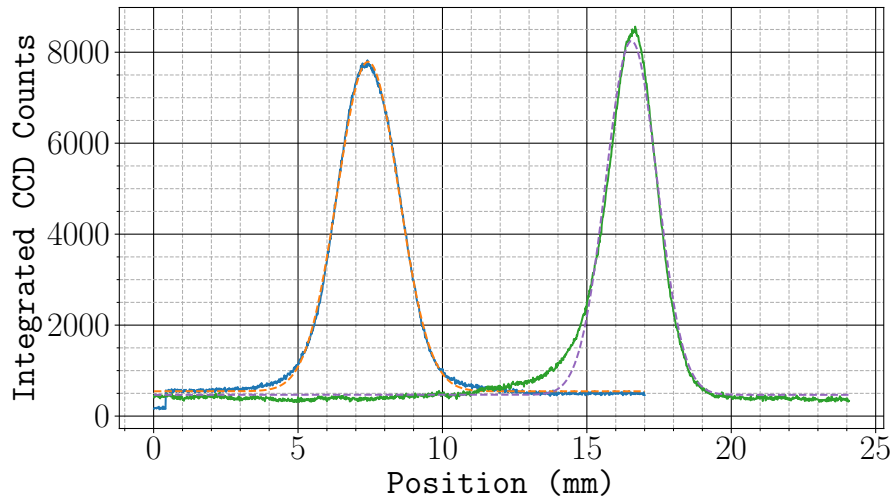


**Figure 5.4.:** Integrated pixel count for a single image during ballistic expansion. The dashed lines indicate non-linear least squares fits to a Gaussian function.

## Measuring the Launch Trajectory

The same method used to measure the temperature of the cloud can also be used to measure the position of the centre-of-mass. In this case, the quantity of interest is  $\langle x(t) \rangle$ . Since the cloud is in free-fall, the trajectory for the centre-of-mass is then given by the well-known equation-of-motion for a particle moving under constant acceleration

$$\langle x(t) \rangle = \langle x(0) \rangle + v_x t + \frac{1}{2} a_x t^2 \quad (5.5)$$

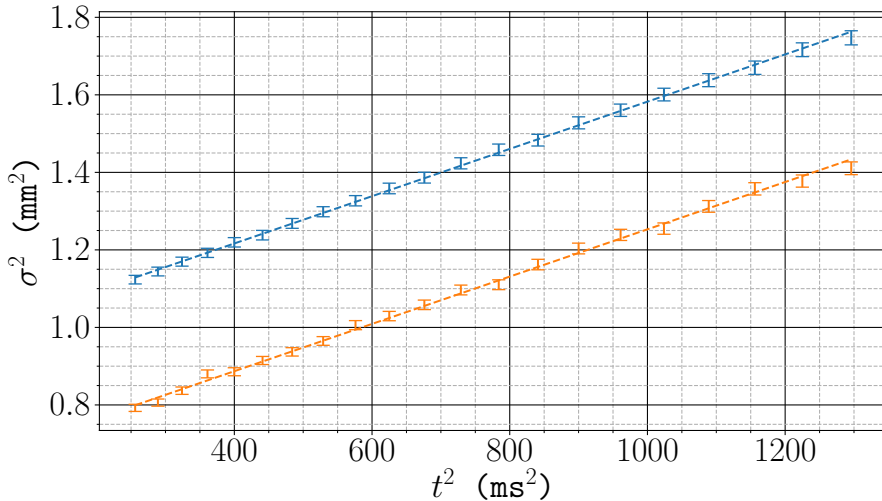


**Figure 5.5.:** Atom cloud temperature using a ballistic expansion measurement. After molasses, the cloud is left to expand in the dark and in a region of close to zero magnetic field. A least-squares linear fit of  $\sigma(t)^2$  is used to estimate the temperature using equation (5.4). The gradient from the fits for the horizontal (blue) and vertical (orange) axes are  $T_x = 6.38(11) \mu\text{K}$  and  $T_y = 6.38(9) \mu\text{K}$ .

where  $v_i$  is the initial velocity along the given axis and  $a_i$  is the acceleration.

To launch the atoms both vertically and horizontally (along the axis parallel with the Raman light), the  $(z_+, z_-)$  AOMs were ramped so that the relative frequency difference between each beam was  $2 \times 320 \text{ kHz}$  and the  $x$  and  $y$  AOM frequencies were ramped to give a frequency difference of  $2 \times 75 \text{ kHz}$  between the horizontal MOT beams. Figure 5.3 is a plot of the measured centre-of-mass position along the horizontal and vertical camera axes over time. A linear least-squares fit to equation (5.5) gives a vertical launch quantities of  $v_v = 25.00(24) \text{ cm s}^{-1}$  and  $a_v = -9.400(51) \text{ m s}^{-2}$  and  $v_h = 7.39(14) \text{ cm s}^{-1}$  and  $a_h = -0.320(36) \text{ m s}^{-2}$  along the horizontal axis.

When compared to the expected velocities from the detunings,  $v_v^{(l)} = 24.96 \text{ cm s}^{-1}$  and  $v_h^{(l)} = 5.85 \text{ cm s}^{-1}$ , the measured horizontal velocity is far greater than expected. This can be explained by a residual magnetic field, that is not cancelled using the bias coils. In the presence of a magnetic field, atoms cooled in an optical molasses are

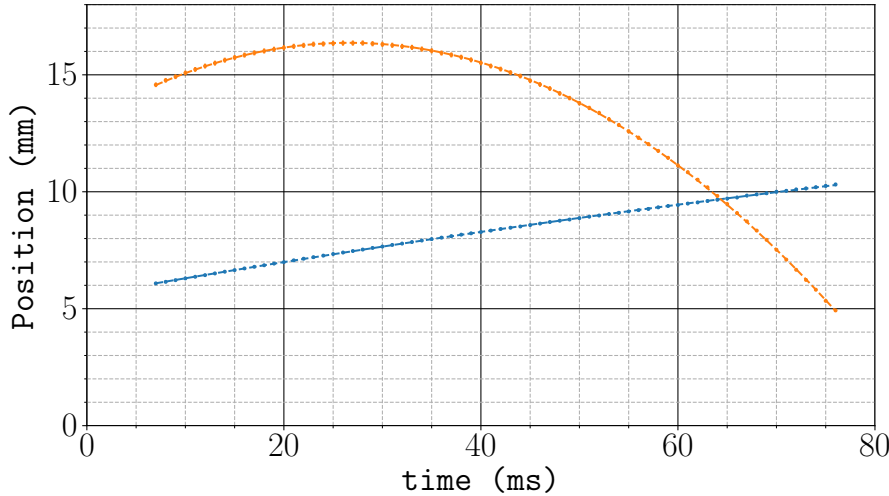


**Figure 5.6.:** Measured centre-of-mass position over time. The horizontal component of the position is shown in blue and the vertical in orange. Each trajectory is fit to equation (5.5) to estimate the launch velocity. The best-fit values are  $v_v = 25.00(24) \text{ cm s}^{-1}$  and  $a_v = -9.400(51) \text{ m s}^{-2}$  along the vertical axis and  $v_h = 7.39(14) \text{ cm s}^{-1}$  and  $a_h = -0.310(36) \text{ m s}^{-2}$  along the horizontal.

decelerated to a velocity at which the Zeeman shift is cancelled by the Doppler shift. This velocity-selective resonance depends on the orientation of the magnetic field to the polarisation of the light. In a one-dimensional optical molasses, a resonance occurs at  $v_{\text{res}}^{(1)} = -\mu_B g_F B / \hbar k$  when the magnetic field is aligned with the wavevector of the light [33]. When the field is aligned at an arbitrary angle an additional resonance at  $v_{\text{res}}^{(2)} = -\mu_B g_F B / 2\hbar k$  is present, due to additional  $(\sigma^\pm - \pi)$  transitions [34]. A residual field along the Raman axis of 20 mG would shift the resonance along  $\vec{x}$  and  $\vec{y}$  by  $1.09 \text{ cm s}^{-1}$  corresponding to a velocity of  $1.54 \text{ cm s}^{-1}$  along the Raman axis. The magnetic field inside the chamber is controlled using bias coils and no attempt was made to cancel magnetic field gradients. It is plausible that a residual field of this magnitude is a result of a magnetic field gradient.

## 5.3. State Preparation

After the atoms have been cooled in an optical molasses, the population will mostly be distributed across the  $|F = 2\rangle$  level, along with a small fraction distributed across the  $|F = 1\rangle$  level. The Raman transition only couples the  $|1, 0\rangle$  and  $|2, 0\rangle$  states, so atoms in the other hyperfine ground states cannot participate in the interferometer. In fact, since the individual Zeeman sub-levels are not resolved during detection, these background atoms result in a loss of fringe visibility. One way to overcome this is to apply a pulse of light resonant with the  $|F = 2\rangle \rightarrow |F' = 3\rangle$  transition to push the non-participating atoms out of the interferometer detection region. Of course, this must be done after applying a Raman pulse to transfer an ensemble of atoms from  $|2, 0\rangle$  into  $|1, 0\rangle$ . In this simple scheme a large fraction of the atoms are removed, which is undesirable since measurements of a low number of atoms are inherently more uncertain due to shot number fluctuations.

The following section discusses a method of preparing the atoms to increase the population in the  $|1, 0\rangle$  ground state. An overview of the scheme is given in Section 5.3.1. This is followed by a discussion of the initial steps which optically pump atoms into the  $|1, 0\rangle$  state in Section 5.3.2. A description of the microwave pulse used to drive atoms into the  $|F = 2\rangle$  level is given in Section 5.3.3. This section concludes with the method used to blow away the atoms which do not contribute to the interferometer in Section 5.3.4. A key step which has been omitted is the velocity-selective Raman pulse. This is described in more detail later, in Section 7.4.3.

### 5.3.1. Schemes for Preparation

The scheme used to prepare atoms in the  $|1, 0\rangle$  state is the following:

1. Light resonant with the  $|F = 2\rangle \rightarrow |F' = 2\rangle$  transition pumps atoms into the  $|F = 1\rangle$  level
2. Light resonant with the  $|F = 1\rangle \rightarrow |F' = 0\rangle$  transition drives ( $\sigma^\pm$ ) transitions to pump atoms into the  $|1, 0\rangle$  dark state
3. A microwave  $\pi$ -pulse transfers atoms to  $|2, 0\rangle$
4. A Raman  $\pi$ -pulse transfers atoms with a narrow velocity spread back to  $|1, 0\rangle$
5. The atoms which remain in  $|F = 2\rangle$  are blown away

A diagram of the population of each hyperfine ground state and the laser frequencies used to drive these transitions is given in Figure 5.7. With the exception of step 4, the light is provided by the  $\mu$ Quans laser using the **MOT** collimators aligned to the vertical  $\vec{z}$  axis. The frequency of the cooling laser and the repump sideband are set so that the relevant transitions for steps 1 and 2 are addressed. As the  $|F = 1\rangle$  light is a sideband of the  $|F = 2\rangle$  light, it is not possible to blow away atoms in  $|F = 1\rangle$  without also blowing away atoms in  $|F = 2\rangle$ . This problem is overcome by using microwave pulses to drive atoms up to  $|F = 2\rangle$  before velocity selection.

A timing diagram of the state preparation sequence is shown in Figure 5.8, which indicates the duration for which each optical or microwave pulse is applied, as well as the direction of the applied magnetic field. The field is switched slowly over 2 ms (which is omitted from the diagram) to preserve the spin state of each atom.

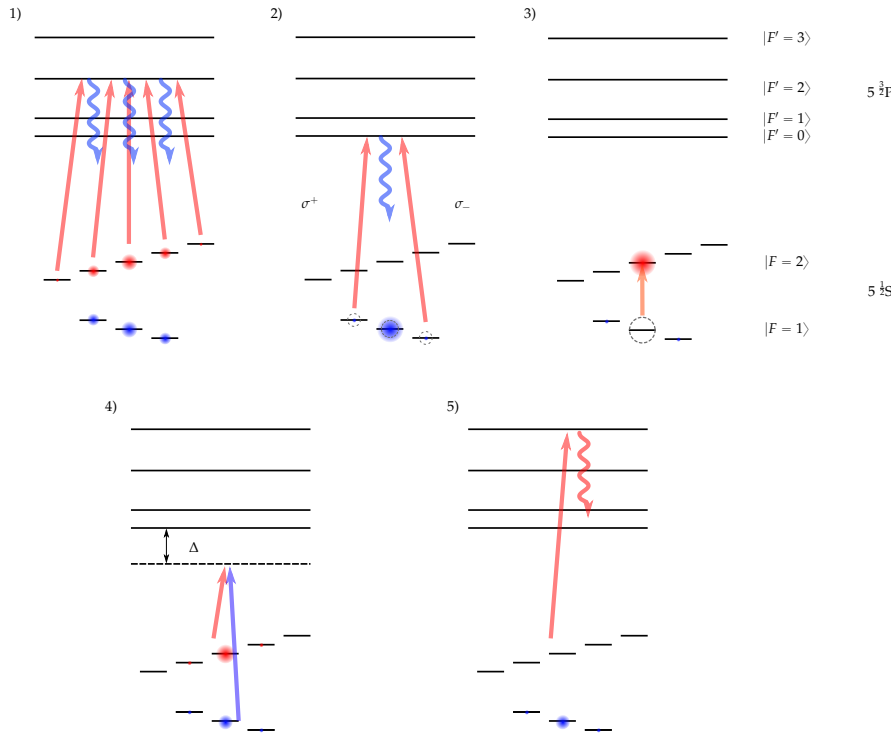


**Figure 5.7.:** Sequence of optical and microwave pulses used to prepare an ensemble of atoms in  $|1,0\rangle$ . The red arrows indicate optical transitions to and from  $|F = 2\rangle$  and equivalently for the blue arrows and  $|F = 1\rangle$ . A residual population in the  $|1,\pm 1\rangle$  states is present, which contributes to a background during the interferometer.

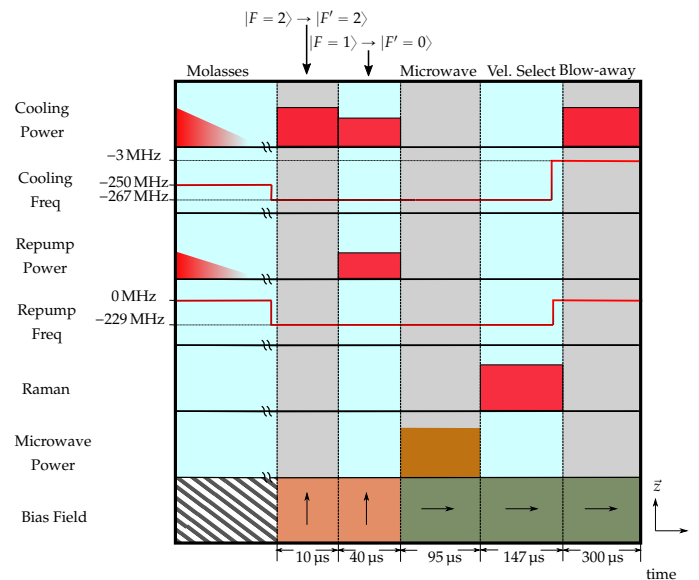


**Figure 5.8.:** Timing diagram for state selection sequence. The durations labelled are indicative of the time required to drive the atoms into the desired state at each step. After the  $|F = 1\rangle \rightarrow |F' = 0\rangle$  pumping, the magnetic field is re-oriented along the Raman axis  $\vec{r}$ . The 2 ms field switching time has been omitted.

### 5.3.2. Optically Pumping the Atoms

#### Driving the $|F = 2\rangle \rightarrow |F' = 2\rangle$ transition

After the molasses, the frequency of cooling light is 150 MHz below the  $|F = 2\rangle \rightarrow |F' = 3\rangle$  transition. This can off-resonantly excite an atom to the  $|F' = 2\rangle$  excited level, but the small scattering rate means that on average, an atom will need to scatter many photons before it is pumped into the  $|F = 1\rangle$  level. Therefore, to minimise the heating during this pumping process, the frequency of the cooling light is resonant with the  $|F = 2\rangle \rightarrow |F' = 2\rangle$  transition.

Figure 5.9 shows the population in the two hyperfine ground states as the duration of the  $|F = 2\rangle \rightarrow |F' = 2\rangle$  light is increased. The rate at which atoms are pumped into  $|F = 1\rangle$  increases with the strength of the applied magnetic field. At zero field, there exists a dark state which is a coherent superposition of the  $|2, m_F\rangle$  states [35]. Applying a magnetic field lifts the degeneracy between the Zeeman sub-levels so that this dark state is no longer stationary. The evolution rate of this dark state, and hence pumping rate, increases with an increasing Zeeman shift. At a field strength of 3 G, the atoms can be pumped into  $|F = 1\rangle$  in less than 5  $\mu$ s.

#### Driving the $|F = 1\rangle \rightarrow |F' = 0\rangle$ transition

After this first pumping step, the atoms are distributed across the Zeeman sub-levels in  $|F = 1\rangle$ . The next pulse of light is used to increase the population in  $|1, 0\rangle$  by driving  $|F = 1\rangle \rightarrow |F' = 0\rangle$  transitions. During this time, the  $|F = 2\rangle \rightarrow |F' = 2\rangle$  light remains on which helps to prevent atoms from populating the  $|F = 2\rangle$  level through off-resonant  $|F = 1\rangle \rightarrow |F' = 1\rangle$  excitations. The magnetic field present means that the circularly-polarised  $\vec{z}$  MOT beams only drive  $\sigma^\pm$  transitions, so the  $|1, 0\rangle$  state is in principle a dark state.

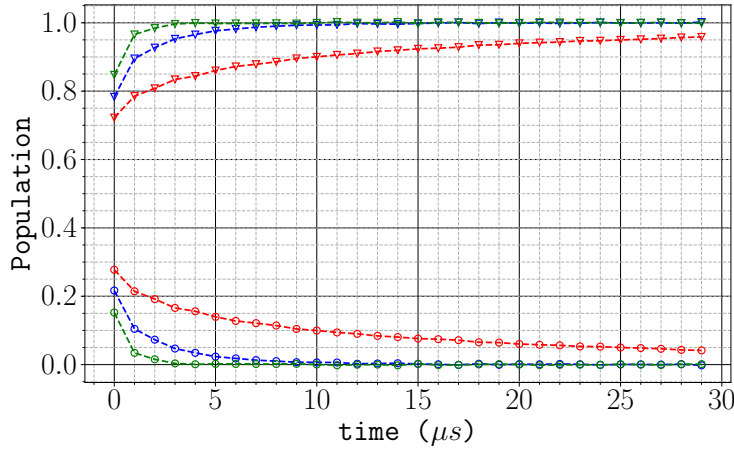


**Figure 5.9.:** Population across the two hyperfine ground states after  $|F = 2\rangle \rightarrow |F' = 2\rangle$  pumping under various magnetic field strengths. The  $\triangledown$  ( $\circ$ ) markers indicate the population in  $|F = 2\rangle$  ( $|F = 1\rangle$ ). The red, blue and green series correspond to field strengths of  $-0.16\text{ G}$ ,  $1.67\text{ G}$ , and  $3\text{ G}$ , respectively.

The distribution of atoms across the Zeeman sublevels was measured using a microwave pulse to drive atoms into the  $|F = 2\rangle$  level, which is described in Section 5.3.3. For each  $\pi$  microwave transition, the frequency of the microwave field was varied to find the resonant frequency. The resulting spectra for  $m_F = -1$  and  $m_F = 0$  are shown in Figure 5.10, both with and without applying light to pump into the  $|1, 0\rangle$  state. The  $0 \rightarrow 0$  clock transition is detuned from the hyperfine splitting frequency due to the applied magnetic field, giving a second-order Zeeman shift of  $515\text{ Hz G}^{-2}$ . The measured shift of  $5.6\text{ kHz}$  corresponds to a field strength of  $3.3\text{ G}$ .

A plot of the population in each Zeeman sub-level for increasing pumping times is given in Figure 5.11. In this instance, the optical pumping does not completely deplete the population from the  $m_F = \pm 1$  sub-levels. After pumping for  $30\text{ }\mu\text{s}$ , approximately 5% of the population remains in the  $m_F = \pm 1$  sub-levels. The  $|1, 0\rangle$  state can only be excited to  $|F' = 0\rangle$  by  $\pi$ -polarised light, which suggests that the magnetic field is mis-aligned with the  $\vec{z}$  MOT beams. The effect of these background atoms on the measured interferometer signal is discussed later, in Section 7.3.3.

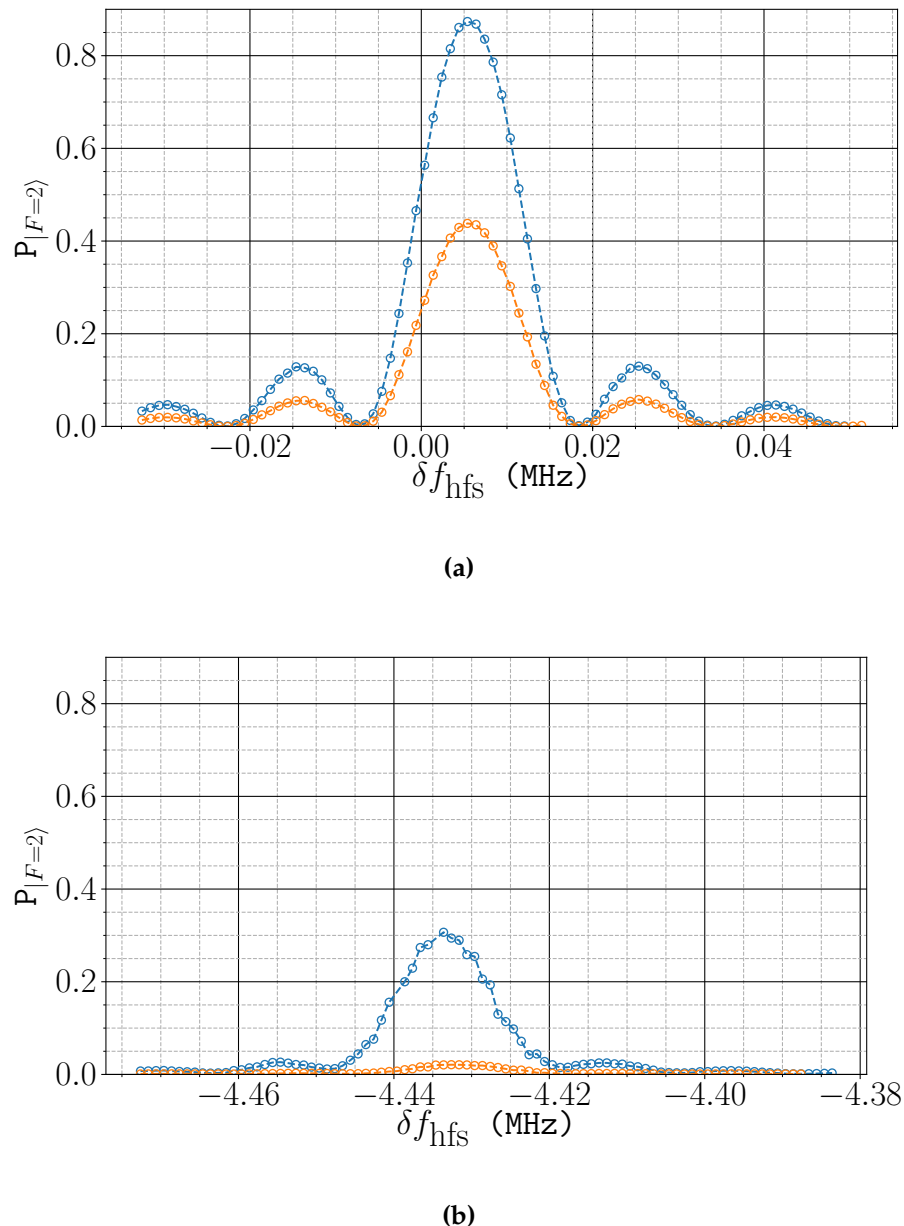


**Figure 5.10:** Population of atoms in (a)  $|1,0\rangle$  and (b)  $|1,-1\rangle$ , measured by applying a  $68\mu\text{s}$  microwave pulse to drive atoms into the  $|F=2\rangle$  level. The orange and blue points indicate the measured populations with and without  $|F=1\rangle \rightarrow |F'=0\rangle$  pumping. The microwave frequency is plotted as a detuning from the hyperfine splitting frequency  $f_{\text{hfs}}$ .

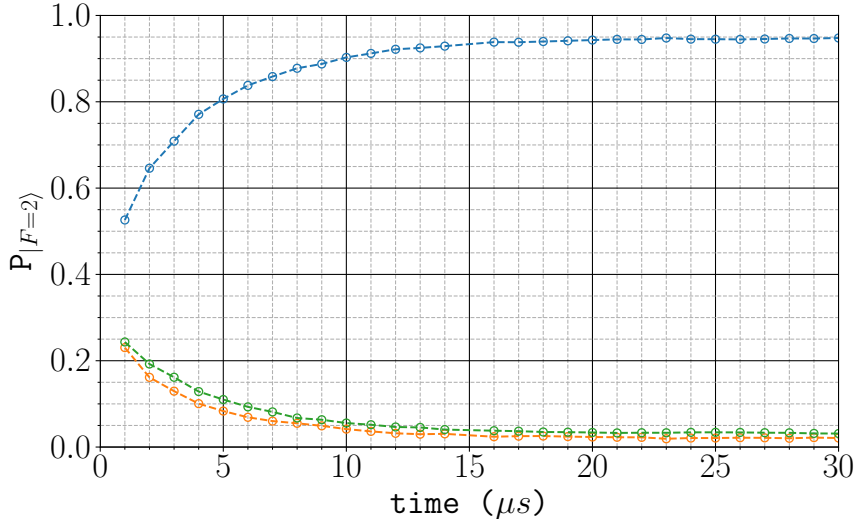


**Figure 5.11.**: Population in each Zeeman sub-level as the  $|F = 1\rangle \rightarrow |F' = 0\rangle$  pumping time is increased. The  $m_F = 0, -1, +1$  populations are shown in blue, orange and green, respectively. After 30  $\mu\text{s}$ , approximately 5% of the population remains in the  $m_F = \pm 1$  sub-levels.

### 5.3.3. Including Microwave Transitions

Without a dedicated laser to drive transitions from the  $|F = 1\rangle$  level, it was necessary to implement a scheme to use light resonant with the  $|F = 2\rangle$  level to remove background atoms. Therefore, we included a system for driving microwave frequency transitions from  $|1, 0\rangle$  to  $|2, 0\rangle$ .

#### Microwave Generation

A diagram of the setup for this is shown in Figure 5.12. The microwave radiation is generated using a *Wind-Freak* synthesiser to output a microwave field oscillating at a frequency close to the hyperfine splitting frequency,  $f_{\text{hfs}} = 6.838\,46\,\text{GHz}$ . This is amplified by *MiniCircuits MCL ZRON-8G+* amplifier and directed into the chamber using a *Pasternack PE9859/SF-10* microwave horn, which produces a linearly-polarised microwave field. The horn was aligned to the chamber at the position which max-

imised the population of atoms in the  $|2, 0\rangle$  state. The synthesiser is clocked using a stable 100 MHz signal from the  $\mu$ Quans laser. When the synthesiser was clocked using its internal 27 MHz reference clock, this produced a noticeable jitter in the output frequency, which led to a significant shot-to-shot fluctuation in the  $|2, 0\rangle$  population.

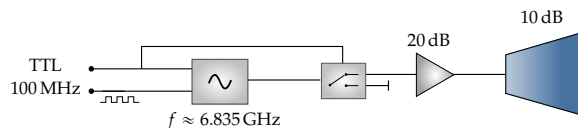
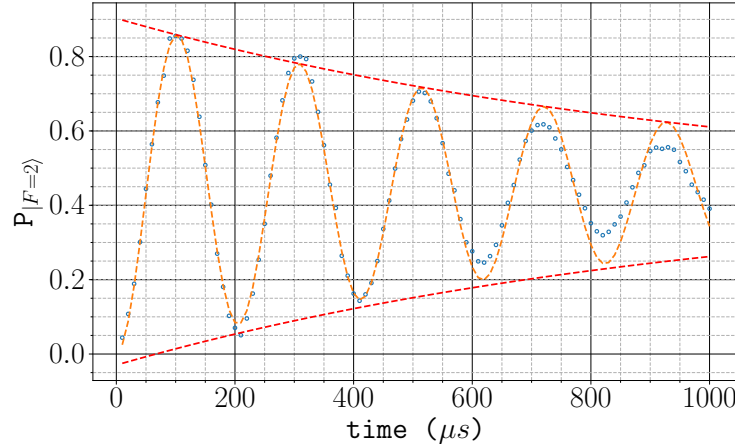


**Figure 5.12:** Schematic diagram of the microwave assembly. The frequency close to the hyperfine splitting frequency is generated by a *Wind-Freak* synthesiser. A 100 MHz clock signal acts as a stable reference frequency for the synthesiser. The generated microwave power is amplified twice, first by a low-power *Mini-Circuits* amplifier, then by a microwave horn, which produces a highly directional, linearly polarised wave. The output is controlled by a digital signal, both at the synthesiser and at a bi-directional microwave switch. The second port of this is blocked with a  $50\Omega$  terminator to prevent reflections.

## Pulse Characterisation

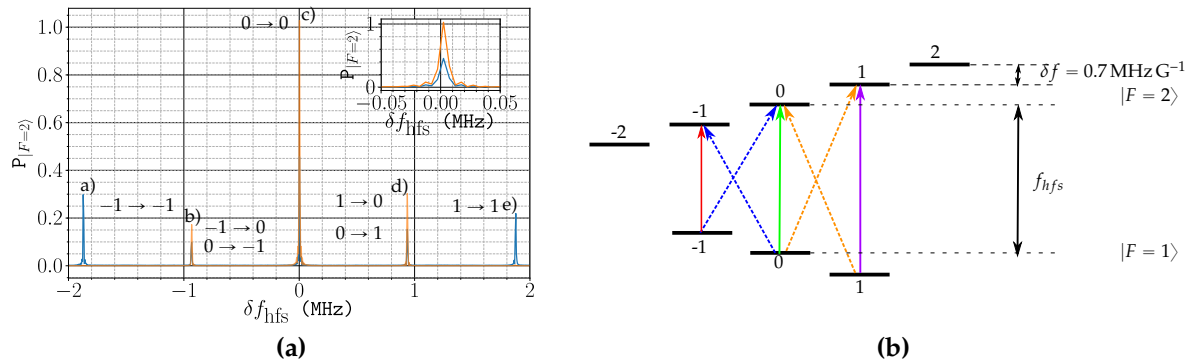
Figure 5.13 shows a measurement of the population in the  $|F = 2\rangle$  level for increasing durations duration of the applied microwave pulse. Rabi oscillations between the  $|1, 0\rangle$  and  $|2, 0\rangle$  states are clearly present. The loss of coherence between the states can be explained by an inhomogeneous driving field. Once inside the chamber, the microwaves reflect and scatter off the interior surfaces which results in a spatially-dependent Rabi frequency. This also leads to a depolarisation of the field, as  $\sigma^\pm$  transitions were also observed. Initially, around 85% of the population was driven into  $|F = 2\rangle$  using a microwave pulse of 100  $\mu$ s. After improving the alignment of the magnetic field during the microwave pulse, this fraction increased to 97% - the remaining 3% being distributed across the  $m_F = \pm 1$  states.

Figure 5.14a shows a spectrum obtained by varying the frequency of the microwave pulse. This shows the presence of  $\Delta m = \pm 1$  transitions from  $|1, 0\rangle$ , as well as the fact



**Figure 5.13.:** Damped Rabi oscillation between  $|1,0\rangle$  and  $|2,0\rangle$  using a microwave pulse of varying length. At longer pulse times, there is a loss of coherence due to a dephasing between the two states. The red dashed line is an envelope is a fit to a decaying exponential with a characteristic time of  $\tau = 1016\ \mu\text{s}$ .

that the population in  $|1, m_F = \pm 1\rangle$  decreases after the  $|F = 1\rangle \rightarrow |F' = 0\rangle$  pumping step is applied. The linewidth of the microwave transition is much narrower than the Zeeman splitting, so only the clock transition is driven when a pulse with a frequency close to  $f_{\text{hfs}}$  is applied.



**Figure 5.14.:** (a) shows the microwave transition spectrum before (blue) and after (orange)  $|F = 1\rangle \rightarrow |F' = 0\rangle$  pumping. (b) shows the transitions addressed as the microwave frequency is varied. Dashed and lines indicate  $\Delta m = \pm 1$  transitions and solid lines indicate  $\Delta m = 0$ . In order of increasing frequency, the transitions in (a) are highlighted in: a) red, b) blue, c) green, d) orange and e) purple.

### 5.3.4. Blow-Away

After the atoms populate  $|2, 0\rangle$ , a velocity-selective Raman  $\pi$ -pulse is applied to transfer a fraction of those back into  $|1, 0\rangle$ . This step is discussed in detail in Section 7.4.3. The velocity-selective Raman pulse transfers 4% the atoms back to  $|1, 0\rangle$ . The remaining need to be removed, otherwise they contribute to a large background signal.

The final pulse during the state preparation sequence is used to push these non-contributing atoms out of the interferometer region. A single MOT beam is used so that there is a net momentum transfer to the atoms as they absorb light and fluoresce. The frequency of this blow-away beam is detuned from the  $|F = 2\rangle \rightarrow |F' = 3\rangle$  transition by  $-3\text{ MHz}$ , which is the same frequency used for detection (see Section 7.3). A pulse of  $50\text{ }\mu\text{s}$  is enough to remove all atoms in  $|F = 2\rangle$ .

## 5.4. Conclusion

This chapter has presented the stages of the experiment which are used to prepare an ensemble of atoms for interferometry. This requires cooling the atoms to limit the thermal expansion of the cloud during interferometry. The atoms are also launched using a moving molasses so that only one pair of beams is resonant with the Raman transition. Finally, we then apply a sequence of optical and microwave pulses, to increase the population of atoms in  $|1, 0\rangle$ . A velocity-selective Raman pulse with a narrow linewidth is used to make the velocity spread along the Raman axis much smaller than the Doppler width. Aside from some residual population in  $|1, \pm 1\rangle$ , the remaining atoms are removed using a pulse of light close to resonance with the  $|F = 2\rangle \rightarrow |F' = 3\rangle$  transition. This results in an ensemble of which around 40% of the population contributes to the interferometer signal.

# **Chapter 6.**

## **Raman Optical System**

### **6.1. Chapter Outline**

This chapter presents in detail the optical system used to produce a large collimated beam for driving Raman transitions. It begins with a motivation of the need to minimise wavefront distortions and intensity gradients in Section 6.2. This is followed by a description of the components that form the collimator in Section 6.3. Section 6.4 presents an overview of the retro-reflection assembly.

### **6.2. Wavefront Requirements**

The sensitivity of an atom interferometer to inertial forces depends on the phase of the light during each pulse. Any component to this phase that does not result from the acceleration of the atoms along the Raman axis is a source of error. This section outlines the optical characteristics of the light which affect the sensitivity of the atom interferometer. These are discussed in the context of this experiment, where gravity

induces transverse motion across the light. For instance, a gradient of intensity across the atom cloud leads to a variation in the Rabi frequency that dephases the atoms and reduces the interferometer fringe contrast. This places requirements on the beam waist size, which are discussed in Section 6.2.1.

A further constraint on the optical system comes from sources of wavefront aberrations. These lead to a spatially-varying phase that results in a bias to the interferometer phase. This phase is not the same for each atom and therefore reduces the interferometer fringe contrast. This was a large motivating factor for mounting the optical system inside the vacuum chamber. The effect of wavefront distortions on the fringe contrast are quantitatively discussed in Section 6.2.2.

### 6.2.1. Gradients of Intensity

The effects of a gradient of intensity on the fringe contrast can be shown by considering an ensemble of atoms that are spatially distributed by a Gaussian distribution. Neglecting the effect of the ensemble's velocity distribution on the Raman detuning and for fixed pulse times, the pulse area  $\Omega\tau$  varies only as a function of the radial displacement from the optic axis. The total fringe contrast can be determined by a convolution of the contrast for a single atom with the atomic density

$$\mathcal{C} = \int \frac{1}{\sqrt{2\pi}\sigma_c} e^{-r^2/(2\sigma_c^2)} c(\Omega(r - r_1), \Omega(r - r_2), \Omega(r - r_3)) dr \quad (6.1)$$

where  $\sigma_c$  is the radial width of the atom cloud. The fringe contrast for a single atom is denoted by  $c$ . This is defined in equation (2.26). The arguments refer to the Rabi frequency during each pulse. The duration of each pulse is such that an atom at the centre-of-mass  $r_i$  has a  $\pi/2$  or  $\pi$  rotation. The atom cloud is initially at the centre of the laser and falling under gravity so that centre-of-mass coordinates are

$(0, -\frac{1}{2}gT^2, -2gT^2)$  respectively. It is assumed that the two lasers which drive the Raman transition have the same waist size and Rabi frequency, which is determined by the product of the electric fields (see equation (2.14)). Therefore, the position-dependent Rabi frequency is

$$\Omega(r) = \Omega_0 e^{-2r^2/w^2} \quad (6.2)$$

where  $\Omega_0$  is the Rabi frequency along the optic axis and  $w$  is the waist size – the distance at which the electric field falls to  $1/e$  of its peak value. The fringe contrast as a function as beam waist for an atom cloud of width a width  $\sigma_c = 5$  mm and a time between interferometer pulses of  $T = 25$  ms is plotted in Figure 6.1. For small beam waists, the intensity gradient across the cloud significantly reduces the fringe contrast. In fact, a beam waist much greater than the width of the cloud is necessary to achieve a large contrast between the two interferometer states. Relaxing the assumptions made on the ensemble's velocity distribution to include its influence on the detuning and spatial distribution of the atoms during the interferometer would strengthen this argument.

### 6.2.2. Wavefront Distortions

Another optical effect that influences the sensitivity is distortions of the laser wavefront. In an ideal case, the superposition of the counter-propagating spherical wavefronts of the two lasers results in a planar wavefront for the field that drives the Raman transition. However, propagation through rough optical elements distort these wavefronts and introduce a spatially varying component of the Raman phase that is independent of acceleration. If the atom cloud's trajectory is parallel with the Raman axis, then this additional phase is the same at each laser pulse and is therefore cancelled out.

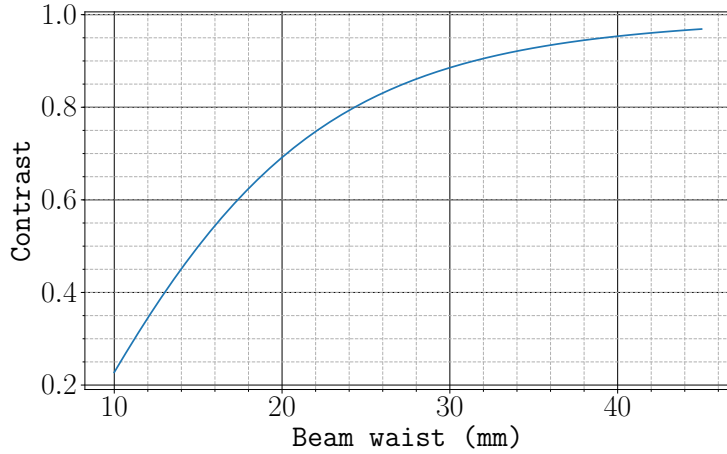


**Figure 6.1.:** Simulated fringe contrast as a function of waist size  $w$  for an atom cloud falling under gravity. This model assumes a Gaussian distributed atomic density with a width  $\sigma_c = 5$  mm and a time between interferometer pulses of  $T = 25$  ms. For smaller beam waists the subsequent interferometer pulses have a larger intensity gradient across the atom ensemble, which increases the dephasing of the two states and reduces the interferometer fringe contrast.

On the other hand, this phase is not cancelled when the cloud moves transverse to the Raman axis. It has the effect of reducing the fringe contrast. Starting with the assumption that this phase is Gaussian distributed around 0, with a standard deviation of  $\sigma_\phi$ , if this is uncorrelated at each interferometer pulse, then the interferometer phase  $\Delta\Phi$  will be distributed with a standard deviation of  $\sigma_\Phi = \sqrt{6}\sigma_\phi$ . Denoting this random phase as  $\delta\phi$ , the fringe contrast is then given by

$$\mathcal{C}(\delta\phi) = \cos(2\delta\phi) \quad (6.3)$$

Following from this, if  $\delta\phi$  is uncorrelated between each atom, the expected value of the contrast over the ensemble is given by

$$\langle \mathcal{C} \rangle = \frac{1}{\sqrt{2\pi}\sigma_\Phi} \int \mathcal{C}(\delta\phi) e^{-\delta\phi^2/2\sigma_\Phi^2} d\delta\phi \quad (6.4)$$

$$= e^{-2\sigma_\Phi^2} \quad (6.5)$$

Figure 6.2 shows the fringe contrast as a function of this random phase.

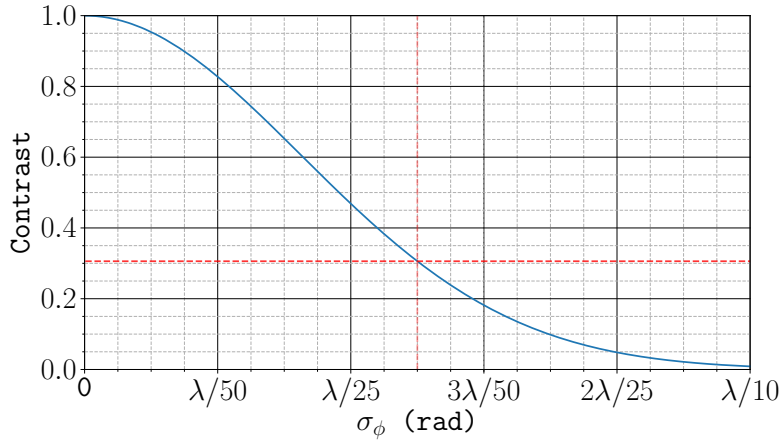


**Figure 6.2.:** Expected contrast as a function of random phase contributions. This assumes that the phase imprinted on an atom during each interferometer pulse has an additional random component that is Gaussian distributed around 0 with a standard deviation of  $\sigma_\phi$ . This random phase is also uncorrelated between each pulse so that the total can be obtained using Gaussian propagation of error. The dashed lines indicate the contrast for phase noise expected from conventional optics, which are usually engineered to a surface flatness of  $\lambda/20$ .

This effect is particularly apparent in the context of optical viewports. The process used to seal an optical viewport to a flange stresses the glass and distorts its thickness. In fact, commercially available viewports are specified to give thickness variations up to  $\lambda/20$ . At this level, the fringe contrast is severely reduced.

A method to systematically characterise this effect has been presented in [36]. This requires mapping the wavefront aberrations caused by each optical elements to numerically calculate their effect on the interferometer phase. This is able to reduce the uncertainty in their measurement of gravity by an order of magnitude. For this experiment, the optics for the Raman light were mounted inside the vacuum chamber to avoid the need for this precise characterisation.

## 6.3. Collimation Optics

The optical system used to produce the beams for driving Raman transitions, which will conventionally be referred to as the Raman optics, was designed to reduce the previously mentioned effects which result in poorer interferometric fringe visibility and sensitivity to accelerations. Principally, the entire optical system was mounted inside the optical chamber so that the Raman light does not pass through any optical viewports before interacting with the atoms. Typically, the stress placed on the glass during the bonding process will distort the flatness more than is acceptable for achieving a high contrast. For example the viewports used for the **MOT** optics have a specified flatness of  $\lambda/4$ , so mounting the entire optical system inside the chamber was the simplest way to avoid a large distortion.

### 6.3.1. Component Overview

Figure 6.3a presents a diagram of the components used to send Raman light into the chamber and produce a collimated beam in the centre of the chamber. The light is coupled into the chamber using a UHV compatible **PM** fibre, manufactured by Diamond photonics. This is a kapton-coated PM-780 HP fibre that is bonded on one end to a DN16 flange using an epoxy resin. The external side of this flange has an FC/APC connector for coupling light from another fibre. Inside the chamber, the ferrule is connected to an FC/APC fibre plate. This is clamped between a piece which bolts onto the inside of a DN63 flange and another stainless steel plate which bolts onto the rest of the optics assembly. Fine adjustment of the position of the fibre along the optic axis is achieved using shim plates with a thickness ranging from 200–300  $\mu\text{m}$ . The fibre plate is free to rotate so that the orientation of the fibre with respect to a **QWP** at the output of the collimator. This **QWP** is manufactured by Light Machinery, and

is described further in Section 6.4. When the fibre is correctly orientated (e.g. when the slow axis of the fibre is at 45deg to the slow axis of the waveplate), the two Raman light fields are orthogonally circularly polarised.

The original design for the optical system consisted of a triplet lens, as a system of three lenses is capable of correcting for the five types of Seidel aberrations that distort rays of monochromatic light. This was designed and manufactured by IC Optical Systems. Another specification for this lens system was that it had to produce a collimated beam with a waist size of around 35 mm so that the sensitivity of the interferometer was not limited by the effects of intensity gradients across the atoms. Unfortunately, the triplet was designed with an incorrect Numerical Aperture (NA). With a focal length of 123.4 mm and a diameter of 50 mm, the triplet lens has a NA of 0.194. However, the nominal NA for PM780-HP fibre used in the UHV compatible PM fibre is 0.12. Consequently, the light from this fibre did not fill the NA of the triplet lens and produced a beam with a waist of 13mm. To address this issue, a pair of aspheric lenses was included to increase the divergence angle of light from the fibre. These are manufactured by Thorlabs and have a focal length of 4.51 mm (352230-B) and 15.29 mm (352260-B), respectively, to give a magnification of 3.39.

### 6.3.2. Alignment and Collimation

As one of the main motivations for mounting the Raman optics inside the vacuum chamber was to reduce the effects of wavefront distortions, it is worth highlighting how inaccurate alignment of the optics can lead to aberrations. As previously discussed in Section 6.2.2, distortions of the wavefront leads to a dephasing and loss of interferometer fringe visibility. Here, the same figures of merit as before are used to consider what misalignment is acceptable to ensure that the phase of the Raman wavefront deviates by less than  $\lambda/100$  after a transverse distance of 12.5 mm.

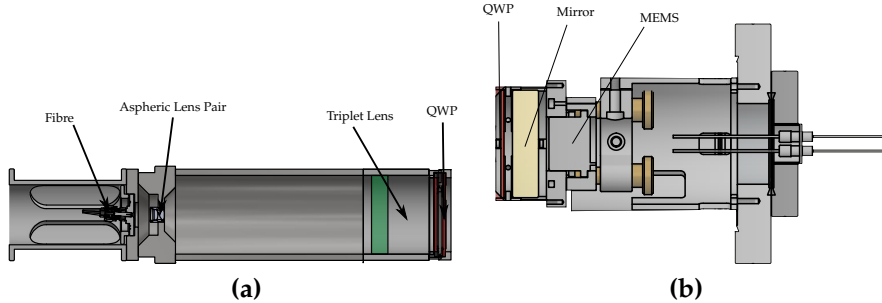


**Figure 6.3.:** Diagrams of the components used in the Raman optical assemblies. (a) shows the collimator setup. Light is coupled into the chamber using a UHV fibre feedthrough. A pair of aspheric lenses is used to increase the divergence angle of the fibre output, before the light is collimated by a triplet lens. Finally, a quarter-wave plate is aligned so that it circularly polarises the collimated light fields. (b) illustrates the other half of the setup, which is used to retro-reflect the light. A second quarter-wave plate is used so that the reflected beams have the same handedness to their respective incoming ones. A MEMS accelerometer is mounted on the back of the mirror to measure vibrations. These components are all mounted on a piezo-controlled mirror mount whose tilt can be controlled from outside the vacuum chamber.

Taking the fibre as a point source, misalignment can occur if it is displaced from the front focal point of the optical system longitudinally along or transversely to the optic axis. If it is transversely displaced, this manifests as an angular displacement of the collimated light after the triplet lens. A large angular displacement is undesirable due to the fact that since one of the Raman light fields propagates further, the two wavefronts that drive acceleration-sensitive Raman transitions are not parallel. Figure 6.4a shows a simulation of the wavefront distortion as a result of this transverse misalignment. This is obtained by simulating the propagation of rays corresponding to each Raman light field through the optical system. The wavefront is estimated using the slope of each ray at a distance of 43 mm from the output of the triplet lens, which corresponds to the position of the centre of the vacuum chamber. The mirror is mounted at the same distance from the centre, so the second beam propagates 129 mm. Close to the optic axis, this distortion is approximately linear (i.e. a tilt) and it can be seen that

a displacement of the fibre from the optic axis of  $<1$  mm is sufficient to achieve the desired wavefront flatness.

Aside from a transverse displacement, it is possible that the fibre could be misaligned along the optic axis. In which case, the output beam will not be collimated. Consequently, the counter-propagating reflected rays will not be antiparallel to incoming ones. The effect of this longitudinal displacement on the Raman wavefront is shown in Figure 6.4b. Further from the optic axis the deviation in the phase of the light is greater, giving a quadratic distortion which is characteristic of a defocus. Comparing the wavefront distortion in this case, a requirement on the longitudinal misalignment of  $< 0.6$  mm is needed for the previously specified flatness.

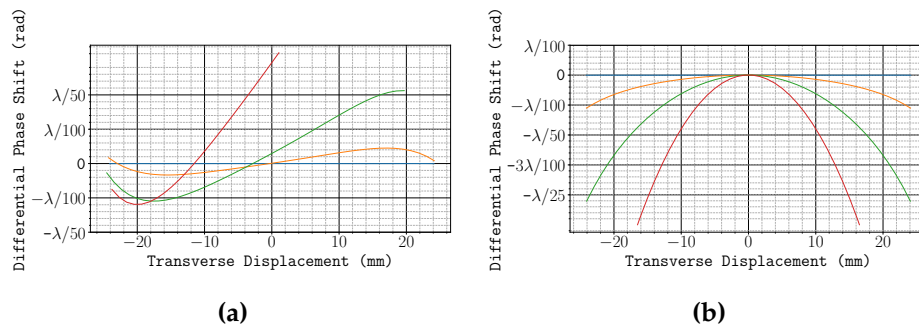


**Figure 6.4.: Simulated wavefront distortion for longitudinal and transverse fibre misalignment.**  
 Rays from a point source with a divergence angle corresponding to a NA of 0.12 are propagated through the Raman optical system. Rays corresponding to the reflected beam are propagated further with the assumption that the mirror is perpendicular to the optic axis. The first set of rays propagates 43 mm and the second propagates 129 mm. The wavefront for each beam is calculated by taking the slope of each ray and subtracting from the slope of the central ray. The wavefront of the effective field that drives the Raman transition is the difference of these two wavefronts. (a) shows the distortion of the wavefront for a transverse misalignment of the fibre for a displacement of 0 mm (blue), 0.5 mm (orange) 1 mm (green) and 1.5 mm (red) from the front focal point. (b) shows the wavefront for longitudinal displacements of 0 mm (blue), 0.3 mm (orange) 0.6 mm (green) and 1 mm (red).

### 6.3.3. Measuring the Beam Width

To measure the waist of the beam, its reflection from a flat surface was imaged using a CCD camera. The radius of the triplet lens is smaller than the beam waist, so the beam is apertured by this lens. To take account of this aperture, the beam waist was estimated using a Taylor expansion of a Gaussian to second order:

$$\begin{aligned} I(x) &= Ae^{-\frac{(x-x_0)^2}{2w^2}} \\ &\approx A - \frac{2Ax_0^2}{w^2} + \frac{4Axx_0}{w^2} - \frac{2Ax^2}{w^2} + \mathcal{O}(x^3) \end{aligned} \quad (6.6)$$

A typical intensity profile along the horizontal and vertical camera axes is shown in Figure 6.5b. A threshold intensity value excludes contributions from pixels outside of the spatial extent of the beam. The waist was estimated using a linear least-squares fit of the intensity profile to a second-order polynomial  $c_0 + c_1x + c_2x^2$ , where

$$w = \left| \frac{\sqrt{c_1^2 - 4c_0c_2}}{\sqrt{2}c_2} \right| \quad (6.7)$$

A plot of the estimated beam waist over a propagation distance of 1 m is shown in Figure 6.5a. Inside the chamber each Raman beam propagates 5.25 cm and 15.75 cm, where the beam is well collimated. Along the vertical axis, the beam has a waist of around 36.9 mm. The horizontal waist is smaller because the camera was horizontally tilted from the beam's optic axis. The projection of the beam onto this axis is consistent with a horizontal tilt of 16°.

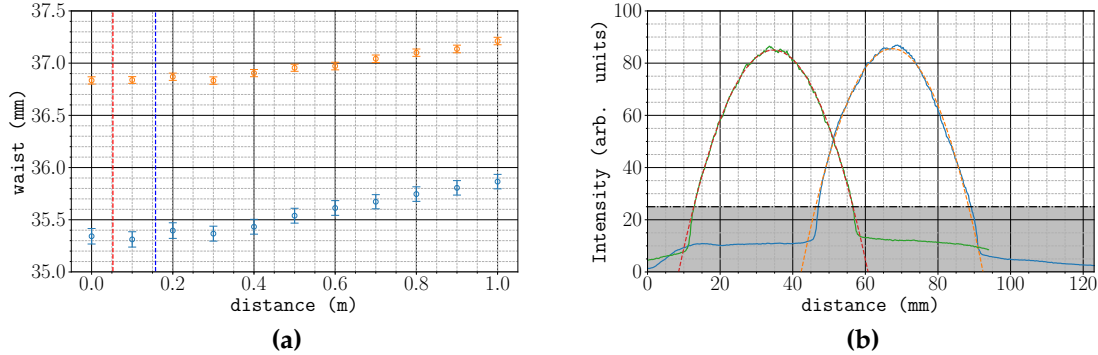


**Figure 6.5.:** Raman beam waist measured over a distance of 1 m, shown in (a). The waist along the horizontal and vertical axes are indicated in blue and orange respectively. The dashed lines indicate the approximate propagation distance of each beam at the position of the atoms. (b) shows the intensity profile along each axis, with the fitted parabola. The dot-dashed line is a threshold intensity value, which excludes pixels from outside the spatial extent of the beam.

## 6.4. Retro-Reflection Assembly

The Raman transitions used in the interferometer are driven by counter-propagating light fields to give a large momentum transfer of  $2\hbar k$  to the atoms. The two beams enter from the same fibre input, so a mirror is used to retro-reflect them. The retro-reflection assembly includes a **QWP** to ensure that the reflected beams have the same polarisation handedness as their circularly polarised incoming counterpart.

The mirror is also manufactured by Light Machinery, and the **QWP** is made to the same specifications as the one that circularly polarises the incoming beams. During the manufacturing process, the waveplates and mirror were polished to reduce irregularities in the thickness of each **QWP** and the surface of the mirror. Figure 6.6 shows the variation in the thickness of the waveplate in front of the triplet lens, measured by Light Machinery using a white light interferometer. This has a standard deviation of 4.62 nm and corresponds a standard deviation of the optical path length of  $8.6 \times 10^{-3}\lambda$ . The **QWP** and mirror are fixed onto the front plate of a UHV compatible MDI-HS mirror mount, manufactured by Radiant dye. The horizontal and vertical tilt of the

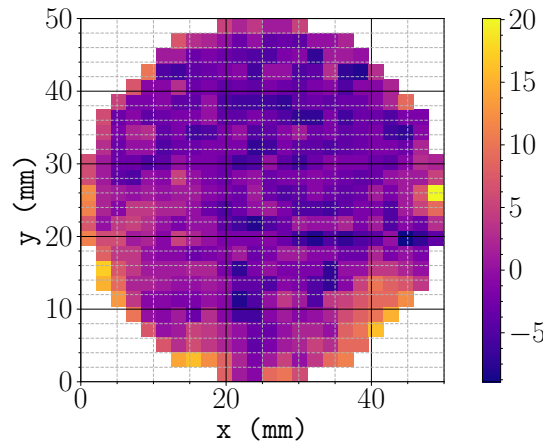


**Figure 6.6.:** Thickness of the first QWP, measured by a white light interferometer. The value is given in nm as a difference from the mean thickness. The standard deviation of this thickness is 4.62 nm and a peak-to-valley (PV) of need number here. Equivalent surface data for the other QWP and mirror were not provided by Light Machinery, but had a PV thickness variation of 19 nm and 9 nm respectively.

mirror can be adjusted using two thumbscrew actuators which cause the front plate to pivot around a ball bearing. This mount is designed for high stability, but of course the alignment will still drift over time. To avoid the need to periodically open the chamber to realign the mirror, a piezo-electric stack is placed between each actuator and the front plate so that the tilt of the mirror can be adjusted externally. Each piezo-stack is connected to a high-voltage feedthrough, so that their length (and hence mirror tilt) can be finely adjusted by controlling the voltage applied across them. A control voltage ranging between 0–10 V is amplified by a controller to give an applied voltage across the piezo stack between -10–150 V. This corresponds to a travel range of 23  $\mu\text{m}$ .

To understand the effect of misalignment, it is instructive to consider its effect on the effective wavevector  $\mathbf{k}_{\text{eff}}$ . If the mirror is misaligned from the incoming beam's wavevector by an angle  $\theta$ , the two counter-propagating fields that drive Raman transitions have wavevectors  $k_1(1, 0)$  and  $k_2(\cos(\theta), \sin(\theta))$ .  $\mathbf{k}_{\text{eff}} = \mathbf{k}_1 - \mathbf{k}_2 \cos(2\theta_i)$ . Fortunately, for small angular displacements, i.e.  $< 1 \text{ mrad}$ , this does not greatly reduce the sensitivity to accelerations. In short, this means that  $\mathbf{k}_{\text{eff}}$  will have a

spatially varying direction. Since an atom interacting via a Raman transition picks up a phase  $\phi = \mathbf{k}_{\text{eff}} \cdot \mathbf{x}$ , atoms travelling along different trajectories will accumulate different phases due to the spatial variation of  $\mathbf{k}_{\text{eff}}$ . Across the atom ensemble, this leads to a dephasing and consequently, a loss of interferometer fringe visibility [37]

#### 6.4.1. In-Situ Alignment and Optimisation

After mounting the Raman optical system inside the chamber, the mirror had to be aligned to retro-reflect the light. When the mirror is close to perpendicular to the light's wavevector, some of the power in the reflected beam couples back into the fibre. In principle, this power is maximised when the mirror is exactly perpendicular so maximising this power is a useful technique to align the mirror. A 99:1 fibre splitter was used to couple light into the chamber, which provided a means to measure the back-reflected power without needing any free-space optics. This was set up so that 99% of the incoming light entered the chamber, with the other 1% coupled into the corresponding output port. Due to the fact that a beam-splitter acts reversibly, 1% of the back-reflected light which couples into vacuum fibre exits the fibre-splitter on the other input port. Therefore, the power at this output was used to indirectly measure the alignment of the mirror.

The travel range of the piezo stacks does not cover the full motional range of the mirror mount. It was initially coarsely aligned using the thumbscrew actuators. Once installed, the lack of direct access to optical system meant that conventional methods to coarsely align the mirror, such as observing the location of the reflected beam's focus, were not feasible. Rather than carry out the somewhat tedious job of systematically adjusting each thumbscrew until the mirror was aligned, an automatic routine was devised to do this. This was carried out using a pair of bipolar stepper motors that each rotated a ball driver inserted into the head of each thumbscrew. The revolution of

these motors was controlled using an Arduino microcontroller, which communicated to the computer using a serial interface. The motors rotated by 0.9deg/step, which corresponds to a tilt of the mirror by  $18.1 \mu\text{rad}$ . This is smaller than the  $0.67 \text{ mrad}$  angular displacement that the piezo stack could provide, but the slow execution speed of the motor control meant that it was more practical to use a combination of the motors and piezos to systematically scan through the tilt of the mirror mount.

Using this method, the mirror mount was aligned so that the maximum of the back-reflected power was reachable with the piezo stacks. Of course, it was foreseeable that the mirror would need to be periodically realigned, which would require another systematic iteration through the voltages applied to each piezo stack. Given that this search was quite time consuming, it was not a practical way to maintain alignment. To improve upon this, an optimisation method using the Nelder-Mead simplex algorithm [38] was implemented. This method is suitable for optimising multidimensional functions and has been used to demonstrate the automatic alignment of a fibre with up to 6 degrees of freedom [39].

The Nelder-Mead algorithm aims to optimise the value of an objective function (in this instance, the optical power measured as a voltage by a photodiode) by sampling the function at various locations. For  $n$  parameters, a set of  $n - 1$  points distributed randomly across the parameter space are chosen as the initial simplex. These are sorted in decreasing order of the value of the objective function and the algorithm proceeds by performing geometric transformations on this simplex, by sequentially reflecting, expanding and contracting this simplex. Each step starts with a reflection about the line between the two greatest values. The coordinates of the simplex are updated if the function has a greater value at the location given by one of these transformations, until the algorithm converges on a maximum value. As with many optimisation algorithms, the Nelder-Mead method has the potential to converge on a local optimum, but this is

alleviated by expanding the simplex to look for more optimal values. The termination of the algorithm was decided by using the standard deviation of the last 5 values. Empirically, it was found that terminating when the standard deviation was less than  $10 \mu\text{V}$  resulted in stable performance of the algorithm, even when the signal-to-noise ratio of the measured voltage was poor. An example of this algorithm aligning the mirror mount is presented in Figure 6.7. To verify that the converged value was optimal, a systematic scan of the piezo stack control voltages in the region around this value was also carried out. In this case, the algorithm converged on a local maximum, but one that greatly enhanced the coupling efficiency of the reflected light back into the fibre. The difference in the piezo control voltages from their optimal values corresponds to a tilt of the mirror mount along the horizontal and vertical axis of less than  $13 \mu\text{rad}$ .

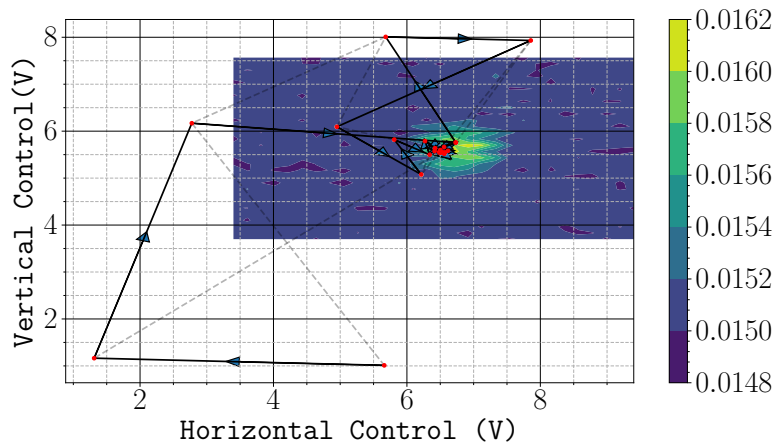


**Figure 6.7:** Automatic mirror alignment using the Nelder-Mead simplex algorithm. A sequence of geometric transformations on the initial simplex are used to converge on the optimum point, where the back-reflected power is maximised. The shaded lines indicate the simplex bounded by the three co-ordinates at each iteration. A raster scan of the piezo control voltages close to the optimum is also plotted. The irregular shape of the measured power is a result of a hysteresis effect when the horizontal control voltage was changed from its maximum value to the minimum.

### 6.4.2. The Mechanical Accelerometer

The periodic interferometer signal means that the interferometer phase is only proportional to acceleration over one fringe spacing  $\Delta a = \frac{\pi}{k_{\text{eff}} T^2}$ . Furthermore, the fringe spacing is inversely proportional to  $T^2$  so there is a trade-off between dynamic range and sensitivity. These problems can be addressed by making use of a mechanical accelerometer mounted onto the back of the retro-reflecting mirror to form a hybrid system [13]. The accelerometer determines the acceleration up to the fringe spacing and the interferometer measures the acceleration more precisely. The accelerometer also measures the vibrations of the retro-reflecting mirror, so it can be used to filter the effects of vibration noise on the interferometer signal. This is discussed in more detail in Section ???. This hybridisation scheme has been used in measurements of gravity in high noise environments such as the centre of Paris [12] and in parabolic aircraft flights [40, 41].

The accelerometer is a navigation-grade AI-Q-2010 manufactured by *Innalabs*. This particular device was chosen because its specified intrinsic noise was  $< 7 \mu\text{g}$  in the 0-100 Hz bandwidth. For a pulse separation  $T = 25 \text{ ms}$ , the fringe spacing is  $31.2 \mu\text{g}$  so it is sensitive enough to measure the acceleration to within one fringe. A schematic of this device is shown in Figure 6.8. It operates using a quartz pendulum which is free to move about one axis [42]. Under an acceleration, the deflection of the pendulum is capacitively detected. A servo loop circuit drives a current through the coils to restore the position of the pendulum. This current is directly proportional to the acceleration of the pendulum. This model has a nominal scale factor of  $1.235\,976 \text{ mA g}^{-1}$ . The acceleration is measured using a load resistance of  $6 \text{ k}\Omega$  to give an output voltage of  $7.56 \text{ V g}^{-1}$ .

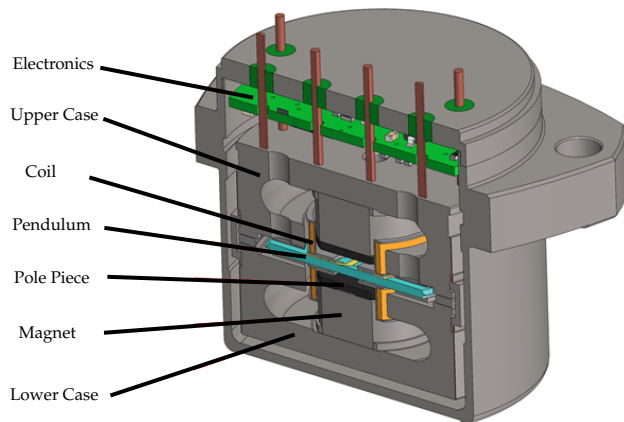


**Figure 6.8.:** Cross-section of the Innalabs AI-Q-2010 accelerometer.

## 6.5. Conclusion

This chapter has motivated the need for low wavefront distortions to achieve sensitive measurements of acceleration, particularly when there is significant transverse motion across the Raman beam. Following this, the in-vacuum optical system was introduced. This helps to reduce the effect of wavefront distortions by not transmitting the beam through an optical viewport. Finally, the retro-reflection assembly used to produce the counter-propagating beams has been presented.

# Chapter 7.

## Acceleration-Sensitive Interference

### 7.1. Chapter Outline

This chapter describes the aspects of the project aimed at observing matter-wave interference in  $^{87}\text{Rb}$  and its subsequent characterisation. The laser system used to drive the necessary Raman transitions is presented in Section 7.2. This is followed by a discussion of the methods used to detect the population in each internal state in Section 7.3. The Raman transition spectrum and dynamics of the atoms during each Raman pulse are discussed in Section 7.4. This chapter continues with an overview of identified sources of noise and their impact on the interferometer's sensitivity to accelerations in Section 7.5. Finally, a presentation of observed interference and an analysis of its sensitivity to accelerations is given in Section 7.6.

## 7.2. The M-Squared Laser System

This section describes the laser system manufactured by *M-Squared Lasers*, which is used to drive Raman transitions. An overview of the laser system can be found in Section 7.2.1, which includes the techniques used to externally communicate with the laser's ICE-BLOC control modules. The control of the frequency and phase-lock is then described in Section 7.2.2. Finally, this section concludes in Section 7.2.3 with a description of the DCS module which is used to control the amplitude, frequency and phase of the Raman laser beat-note during the experiment.

### 7.2.1. Laser System Overview

The Raman laser system contains two Solstis lasers which generate laser light by pumping a Ti-sapphire crystal housed inside a resonator. The output light is frequency-stabilised using piezo-electric stacks to adjust the resonator length [43]. A schematic diagram of this laser system is given in Figure 7.1. Each laser is seeded using a *Lighthouse Photonics Sprout* laser to generate light around 780 nm. The first laser acts as the master whose frequency is fixed to an absorption feature in the transition spectrum of  $^{87}\text{Rb}$ . The second is slaved to this using a phase-locked loop to keep their beat frequency and relative phase constant. The two beams are mixed on a **PBS**, so that they are orthogonally polarised. Two AOMs control the output power.

The system contains 4 ICE-BLOC modules which implement various types of control. The first two (one for each Solstis) are used to stabilise the output power of each laser by feeding back to the corresponding Sprout laser. They are also used to coarsely adjust the output frequency, which is measured using a *HighFinesse* wavemeter. The third is used for the Phase-Locked Loop (**PLL**) and feeds-back onto the slave laser to control both the frequency and phase of the optical beat-note between the two lasers.

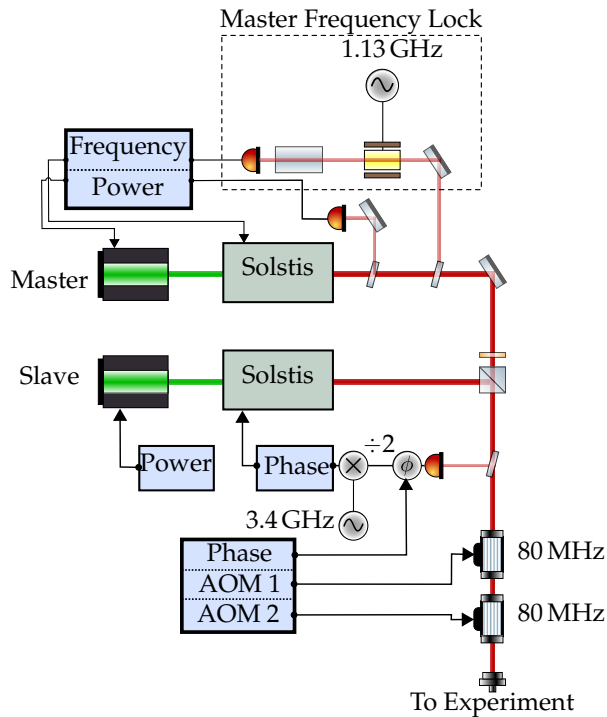


**Figure 7.1.:** Schematic Diagram of the M-Squared laser system. Two Solstis lasers provide the two Raman frequencies, which are fibre coupled onto the orthogonal axes of a PM fibre. Control of the power, frequency and phase as required to drive Raman transitions is handled by the four ICE-BLOC modules indicated in blue. Further detail of this control is given in the text.

The final ICE-BLOC, referred to as the DCS module, is used to control the lasers in real-time during the experiment.

### External ICE-BLOC Control

The ICE-BLOC modules are able to communicate with each other using an Ethernet hub. Another computer connected to this network is able to control them by accessing a web page that each module hosts. These web pages control the ICE-BLOCs by sending structured JSON messages. This graphical interface can be bypassed by directly communicating these messages. This is done using MOTMaster so that various parameters, such as the frequency and phase of the Raman beat-note, can be automatically varied between each experiment cycle.

### 7.2.2. Frequency and Phase Control

#### Master Lock

The frequency of the master laser is stabilised using saturated absorption spectroscopy in a Rubidium vapour cell. Part of the beam is picked off and modulated by an **EOM**. The positive frequency sideband is used to lock the master laser to the 2,3 crossover feature. In effect, this means that the modulation frequency of the **EOM** sets the one-photon detuning of the Raman transition. The modulation frequency is set so that the master laser frequency is 1.13 GHz below the  $|F = 2\rangle \rightarrow |F' = 3\rangle$  transition.

#### Frequency and Phase Lock

The optical beat-note between the two lasers is measured using a fast photodiode. The signal from this is used in a **PLL** to fix the relative phase between the two lasers. A frequency divider halves the frequency of the signal before comparing it to a **VCO** of around 3.4 GHz. This creates an error signal which used to control both the frequency and phase of the beat-note by feeding back to the slave laser Solstis. The relative phase between the two lasers is adjusted using an analogue phase shifter and the frequency difference is controlled by tuning the **VCO** frequency.

The beat-frequency of the Raman lasers can be chirped by triggering a ramp of the control voltage to the **VCO**. For chirp rates of lower than  $24\text{ MHz s}^{-1}$ , the phase-lock is able to keep the beat-note phase-coherent during the chirp.

### 7.2.3. The DCS Module

The DCS module is used to control the output of the lasers during the experiment. It uses an on-board **DDS** to synthesise the 80 MHz driving frequencies for each **AOM**.

The majority of the control is done using an Field-Programmable Gate Array ([FPGA](#)) that synthesises a timed sequence of analogue and digital voltage waveforms. An example of a sequence created using the DCS web interface is shown in Figure 7.2. The sequence is segmented into individual steps and each channel can be separately configured, much like the MOTMaster user interface.

This module is used to control the amplitude, frequency and phase of each Raman pulse. The pulse amplitude is shaped using an analogue voltage to control the power of the RF frequency. The voltage output has been calibrated so that the pulse can be shaped to produce a square, Gaussian or Blackman amplitude envelope. A frequency chirp of the beat-note is optionally triggered by sending a digital pulse to the [PLL](#) ICE-BLOC.

The synthesiser can be configured to run continuously, or to wait at a chosen timestep for an external trigger. It can also iterate through a set number of parameters, such as timestep duration or phase shift by re-building the sequence after each cycle.

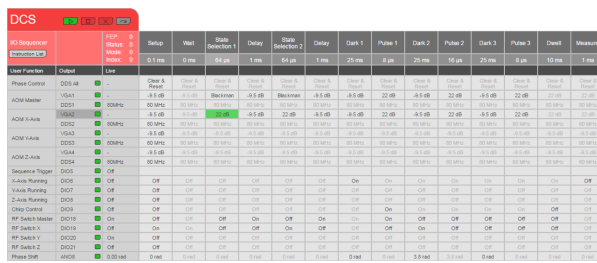


**Figure 7.2.:** DCS module user interface. The sequence is synthesised from individual steps. The parameters of each Raman laser pulse can be configured independently.

### 7.3. Atom Detection

This section describes the methods used to measure the number of atoms in each hyperfine ground state and infer the interferometer phase. It begins with a presentation

the optical setup used to collect fluorescent light on a photodiode in Section 7.3.1. The scheme used to detect the atoms by driving  $\sigma^+$  transitions is then described in Section 7.3.1. This concludes with a discussion on converting the measured photodiode signals into atom number and interferometer phase in Section 7.3.3.

### 7.3.1. Optical Setup

A precise measurement of the number of atoms requires that the atom shot noise is the dominant source of uncertainty. The CCD used in previous stages of the experiment is not sensitive enough for this as there is a significant amount of noise in reading out the charge collected at each pixel. Instead, a more sensitive photodiode is used to detect the atoms. With a suitably high bandwidth, the readout time is much faster than the CCD as well, so that the atoms can be detected well before they fall out of the field of view.

A diagram of the setup used to detect the atoms is given in Figure 7.3. It is a triplet system which uses lenses with focal lengths 150 mm, 75 mm and 60 mm in order from the atoms to the photodiode. A ray-tracing simulation of the optical system indicates spherical aberrations on the image. This is caused by the third lens, which was added to shorten the back focal length. The front lens has a diameter of 50.4 mm, so the solid angle subtended by the optics is  $4\pi \times 7.056 \times 10^{-3} \text{ sr}$ .

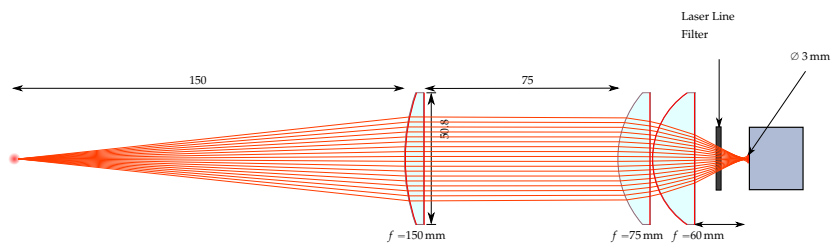


**Figure 7.3.:** Optical setup for photodiode detection. A triplet lens system focuses light from radiated from the atoms onto a photodiode. This is mounted using a translation stage to position the photodiode at the back focal point.

## Photodiode Calibration

The photodiode used is a *Femto LCA-S-400K-SI*, which has a trans-impedance amplifier with a bandwidth of 400 kHz and a photo-sensitive area with a diameter of 3 mm. The scaling factor from incident optical power to output voltage was measured as  $1.84 \times 10^6 \text{ V W}^{-1}$ .

### 7.3.2. Detection using $\sigma^+$ transitions

The atoms are detected using resonance fluorescence from the two vertically aligned MOT beams. A bias field polarises the atoms along the  $\vec{z}$  axis, so the light drives both  $\sigma^+$  and  $\sigma^-$  transitions. The Zeeman shift means that each magnetic sub-level has a different scattering rate, which must be accounted for to calculate the number of atoms. This can be simplified by inverting the handedness of one of the  $\vec{z}$  MOT beams using a liquid-crystal HWP. Now, both beams drive  $\sigma^+$  transitions. The atoms are optically pumped into  $|2, 2\rangle$  and cycle on the  $|2, 2\rangle \rightarrow |3, 3\rangle$  transition. Therefore, only one scattering rate is needed to calculate the number of atoms.

Figure 7.4 shows the setup used to invert the polarisation of one MOT beam prior to detection. The liquid-crystal waveplate is an electro-optical device whose birefringence changes when an ac voltage is applied across it. The waveplate is placed at the output of the downward-propagating ( $\vec{z}_-$ ) collimator. The liquid-crystal waveplate is triggered to rotate the incoming linearly polarised light by  $\pi/2\text{rad}$ .

## Detection Sequence

The sequence used to detect the atoms is shown in Figure 7.5. Shortly before the sequence starts, the bias field is aligned to the  $\vec{z}$  axis and the liquid-crystal waveplate

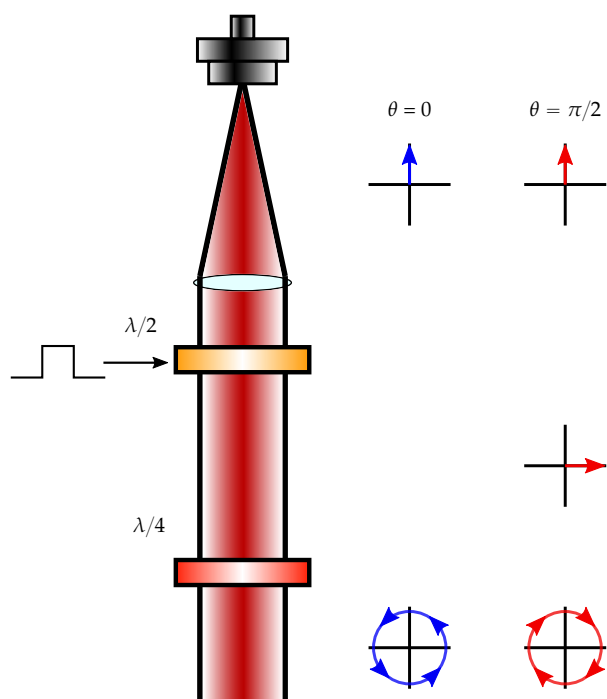


**Figure 7.4.:** Scheme to invert beam polarisation. In the **MOT** loading phase of the experiment, the liquid crystal **HWP** is oriented to give a right-hand circular polarised beam shown in blue. Prior to detection, a digital pulse triggers a re-orientation of its slow axis. This results in a left-hand circular polarised beam, shown in red.

is triggered to change the handedness of the  $\vec{z}_-$  beam. The cooling laser frequency is set so it is detuned by  $\delta_D = 3\text{ MHz}$  below the  $|F = 2\rangle \rightarrow |F' = 3\rangle$  transition and the repump laser is set to resonance with the  $|F = 1\rangle \rightarrow |F' = 2\rangle$  transition. This creates an optical molasses which avoids heating the atoms so that they remain in the detection volume for a longer period of time. The intensity of the light is reduced to around  $3I_{\text{sat}}$ . As shown below, this intensity was empirically found to minimise the variance in output voltage. The acquisition of the photodiode voltage is triggered to start at the first Dwell time. The cooling light is first switched on, so that only atoms in  $|F = 2\rangle$  scatter light. After this, the repump is switched on, so that atoms in  $|F = 1\rangle$  are optically pumped into  $|F = 2\rangle$  and all the atoms scatter light. This repump light is a sideband of the cooling laser, so the total output is increased to ensure that the intensity of the cooling light remains constant. Each detection step lasts 250  $\mu\text{s}$ , but the first 50  $\mu\text{s}$  is discarded to allow time for the intensity to stabilise and for optical pumping into  $|F = 2\rangle$ . The atoms are then blown away by switching off one of the detection beams before the sequence is repeated to collect a background signal.

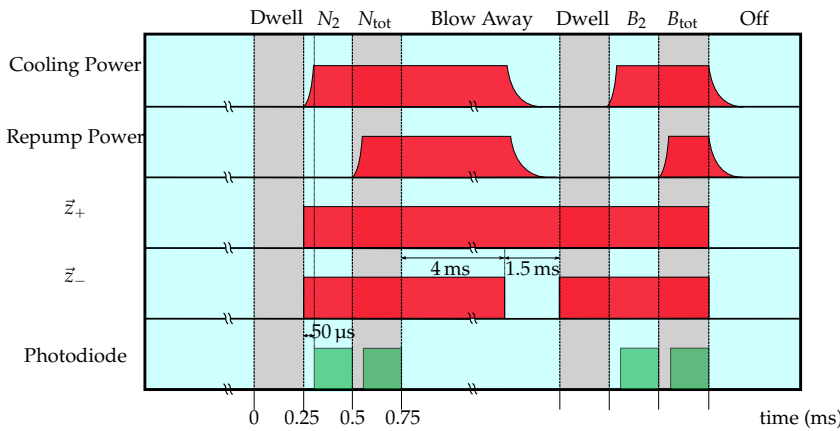


**Figure 7.5.:** Timing diagram for state detection. Atoms in  $|F = 2\rangle$  are detected before the repump light pumps those in  $|F = 1\rangle$ , so they are detected as well. A background light measurement for each step is also taken.

## Maximum Detection Time

As the atoms scatter light during detection, the cloud will be heated and expand due to the momentum exchanged from absorption and spontaneous emission. The atoms are only cooled along the axis of the detection beams, so the heating rate is greatest along the other two axes. It is necessary to ensure that the heating rate is low enough that the atoms remain within the detection beam for the entire detection time. A requirement on the maximum detection time can be obtained as follows. The momentum of an atom scattering photons follows a random walk, so the variance of the momentum along one axis after a time  $t$  is  $\langle \Delta p \rangle^2 = 2Dt$ . The scattered photon is equally likely to be emitted in any direction, so the diffusion coefficient is

$$D = \frac{1}{3}(\hbar k)^2 R_{\text{sc}} \quad (7.1)$$

If the cloud has a Gaussian spatial distribution with an initial width of  $\sigma_0$ , the width at a later time of is given by

$$\sigma_x^2(t) = \sigma_0^2 + \frac{2n_p v_r^2 t^2}{3} \quad (7.2)$$

where  $v_r = \frac{\hbar k}{m_{\text{rb}}} = 6 \text{ mm s}^{-1}$  is the recoil velocity and  $n_p$  is the number of photons scattered. To remain within the detection region, the width of the cloud must be smaller than the detection beam waist  $w$ , so the detection time must satisfy

$$t_D \ll \sqrt{\frac{3(w^2 - \sigma_0^2)}{2(nv_r^2)}} \quad (7.3)$$

For a beam waist of 7.5 mm, initial cloud size of 5 mm and a maximum scattering rate of  $2 \times 10^7 \text{ s}^{-1}$  the detection time must be much less than 4.7 ms.

## Optimal Intensity

The optimal intensity was empirically found by varying the total power in the detection beams and recording the photodiode voltage for a fixed detection time of  $200\text{ }\mu\text{s}$ . Figure 7.6 shows the average voltage measured by detecting atoms in the  $|F = 2\rangle$  state as the intensity of the light increases. The saturation parameter  $s$  is defined using the peak intensity and by the time they are detected, the atoms have moved from this region. A non-linear least squares fit to the function

$$v = a \frac{bs}{1 + bs + 4(\delta_D/\Gamma)^2} \quad (7.4)$$

gives a scaling for the intensity of  $b = 0.83$ . The variance in the measured voltage (for a constant mean number of atoms) is minimised when the intensity is around  $3I_{\text{sat}}$ . Above this intensity, there is a significant depopulation into  $|F = 1\rangle$  caused by off-resonant excitations to the  $|F' = 2\rangle$  state. This is evident in the voltage signal over time, which is shown in Figure 7.7 for various intensities. At an intensity of  $3I_{\text{sat}}$ , around 5% of the population is pumped out of  $|F = 2\rangle$ .

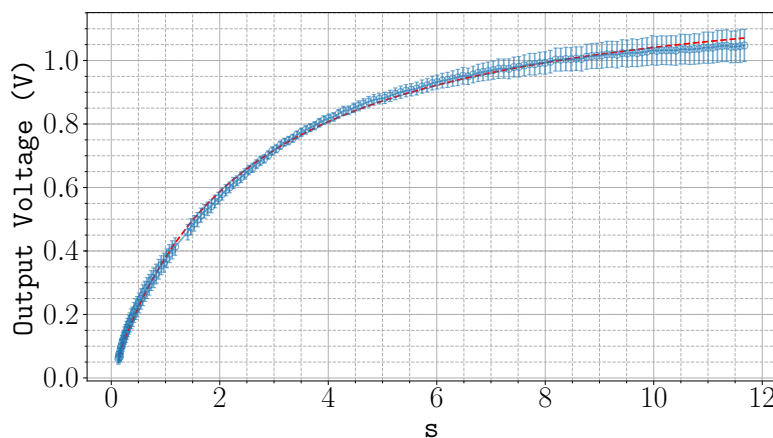


**Figure 7.6.:** Photodiode output voltage for increasing detection beam intensity. The red dashed line indicates a fit to equation (7.4) to estimate the scaling factor for the saturation parameter  $s$ .

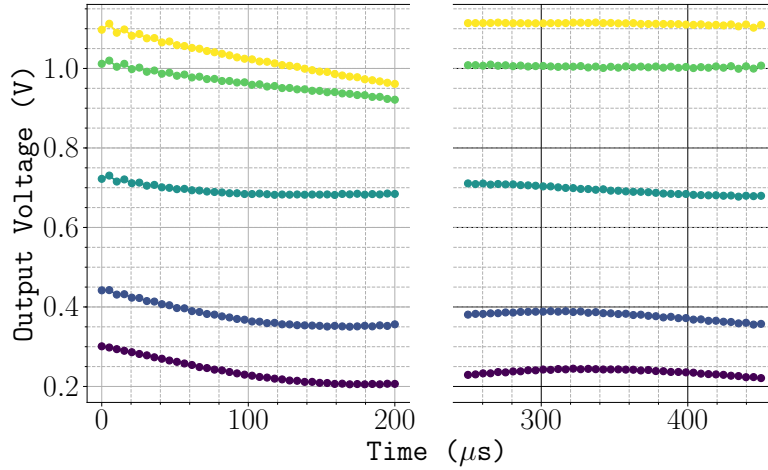


**Figure 7.7.**: Photodiode voltage over time during detection for  $s = 0.5, 1, 3, 7, 10$  in order from purple to yellow.

### 7.3.3. Measuring the Occupation Probability

The occupation probability of the  $|F = 2\rangle$  state is obtained by measuring the proportion of atoms in each hyperfine ground state. The number of atoms  $n_{\text{at}}$  that scatter light on the cycling transition is proportional to the photodiode voltage  $U_{\text{pd}}$  as follows

$$\begin{aligned} U_{\text{pd}} &= \eta R_{\text{sc}}(I, \Delta) n_{\text{at}} \hbar \omega G \\ &= \alpha \eta R_{\text{sc}}(I, \Delta) n_{\text{at}} \end{aligned} \quad (7.5)$$

where  $\eta = \Omega/4\pi$  is the fractional solid angle subtended by the collection optics,  $\hbar \omega = 1.6 \text{ eV}$  is the photon energy,  $R_{\text{sc}}$  is the scattering rate defined in equation (4.2) and  $G$  is the photodiode conversion gain. At the saturation intensity and a detuning of 3 MHz, the voltage measured per atom is around 30 nV per atom. The probability of an atom occupying  $|F = 2\rangle$  is estimated as follows

$$P_{|F=2\rangle} = \frac{N_2 - B_2}{N_{\text{Tot}} - B_{\text{Tot}}} \quad (7.6)$$

where  $N$  and  $B$  denote the average voltage during signal and background measurements, respectively. Subtracting the background signal from each measurement removes the bias that arises from detecting light not scattered by the atoms. The interferometer phase  $\Phi$  is determined from equation (7.6) using

$$P_{|F=2\rangle} = P_0 + \frac{C}{2} \cos(\Phi) \quad (7.7)$$

where  $P_0$  is the mean probability of detecting atoms in  $|F = 2\rangle$  and  $C$  is the interferometer fringe contrast. These are experimentally determined by varying  $\Phi$  as described in Section 7.6.1.

### Atom Number Bias

If is worth describing the voltages measured by the photodiode in more detail. The expression for the population in equation (7.6) assumes that the voltage measured in the  $N_2$  and  $N_{\text{Tot}}$  detection steps are directly proportional to the number of atoms present in  $|F = 2\rangle$  and the total number in the interferometer, respectively. In actual fact, there is a bias in  $N_2$  from the previously mentioned de-population and a bias in  $N_{\text{Tot}}$  from a residual population in the  $|F = 1, m_F = \pm 1\rangle$  states. These contribute to an error in  $P_{|F=2\rangle}$ , which reduces the maximum population that can be detected in  $|F = 2\rangle$ . This causes a reduction in the interferometer fringe contrast and hence, sensitivity. In the following discussion, these systematic errors are addressed emphasise their effect. It is shown that for an increasing fraction of atoms in the  $|1, \pm 1\rangle$  states, this dominates over the depopulation from the  $|F = 2\rangle$  level.

If atoms are pumped out of  $|F = 2\rangle$  at a rate  $\gamma$ , then the number of atoms in the number of atoms in both hyperfine ground states is given by

$$n_2(t) = n_2^i e^{-\gamma t} \quad (7.8)$$

where  $n_2^i$  is the initial number in  $|F = 2\rangle$ . After averaging over a time  $\tau$ , this gives

$$\bar{n}_2 = \frac{n_2^i(1 - e^{-\gamma\tau})}{\gamma\tau} \quad (7.9)$$

Consequently, the number of atoms in  $|F = 1\rangle$  increases. This is expressed as

$$\bar{n}_1 = n_1^i + (1 - e^{-\gamma\tau})n_2^i + n_{\pm 1} \quad (7.10)$$

where  $n_{\pm 1}$  is the background population in  $|1, \pm 1\rangle$ . The bias is the occupation probability is then

$$\delta P = \frac{\bar{n}_2}{\bar{n}_2 + \bar{n}_1} - \frac{n_2^i}{n_1^i + n_2^i} \quad (7.11)$$

This bias has the effect of reducing the interferometer contrast. The residual atoms in  $m_F = \pm 1$  and the depopulation means it is not possible to ever detect the total population in  $|F = 2\rangle$ . The contrast is given by

$$\begin{aligned} C &= P_{\max} - P_{\min} \\ &= 1 - \frac{(1 - e^{-\gamma\tau})}{1 - \alpha} \end{aligned} \quad (7.12)$$

where  $\alpha = \frac{n_{\pm 1}}{n_1 + n_2}$  is the ratio of the number of residual atoms to the number in the interferometer. A plot of the contrast for an increasing proportion of  $m_F = \pm 1$  atoms is shown in Figure 7.8, taking the loss rate of the photodiode signal measured in Figure 7.7

for  $s = 3$ . For an  $m_F = \pm 1$  population of at least 4% of that in  $m_F = 0$ , the reduction in contrast is dominated by the residual atoms.

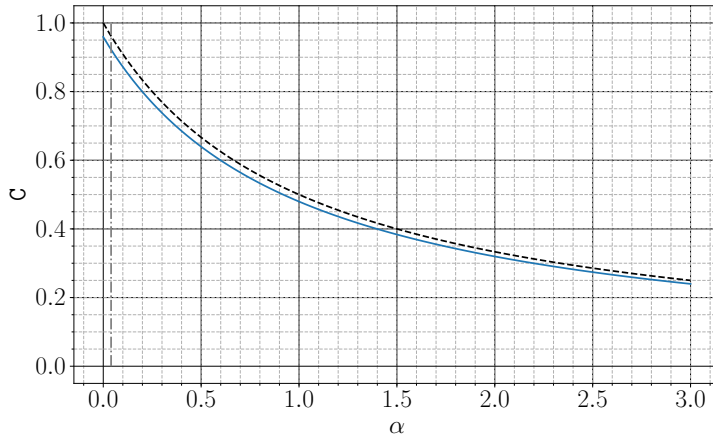


**Figure 7.8.:** Interferometer contrast for an increasing residual atom ratio. The black dashed line indicates the reduction expected when no atoms are lost from  $|F = 2\rangle$ . The dot-dashed line indicates the ratio at which the loss in contrast from the residual atom number dominates over the depopulation.

## 7.4. Individual Pulse Characterisation

This section presents a characterisation of the pulses used to drive Raman transitions between the two hyperfine ground states. First, the properties of the Raman transition spectrum are presented in Section 7.4.1. Following this, a discussion of cancelling the systematic phase from a differential ac Stark Shift is given in Section 7.4.2. Finally, this section concludes with specific details about the individual pulses used in the experiment. The first Raman pulse, which is used to select a subset of atoms with a narrow velocity spread, is presented in Section 7.4.3. This section concludes with a presentation of the dynamics of the three pulses used to coherently control the atoms during the interferometer in Section 7.4.4

### 7.4.1. Raman Transition Spectrum

The state preparation sequence optically pumps the majority of the atoms into the  $|1, 0\rangle$  state. Ideally, each Raman beam is perfectly circularly polarised and can only drive  $|1, 0\rangle \leftrightarrow |2, 0\rangle$  transitions using either of the counter-propagating pairs of beams. More generally, the selection rules of the Raman transition allow for transitions between other states, depending on the polarisation of the light. The allowed transitions between the different Zeeman states are presented in Table 7.2. The laser polarisation configurations are given in Table 7.1. These are defined for an atom being excited from  $|F = 1\rangle$  and stimulated into  $|F = 2\rangle$ , so that the  $\vec{k}_2$  beam *decreases* the angular momentum when it drives a  $\sigma^+$  transition.

Figure 7.9 shows an example of the Raman transition spectrum. The beat frequency between the two Raman lasers is scanned and the light is pulsed for 160  $\mu\text{s}$  to drive atoms into the  $|F = 2\rangle$  state. There is a large peak close to the hyperfine splitting frequency. This peak is a result of Doppler-insensitive co-propagating transitions<sup>1</sup>. This indicates that the two Raman beams are not orthogonally circularly polarised, as that cannot drive co-propagating transitions. This is further supported by the fact that there are  $\Delta m = \pm 1$  transitions, which can only occur if one of the lasers drives a  $\pi$  transition. The Zeeman shift on the co-propagating transitions between  $|F = 1, 0\rangle \rightarrow |F = 2, 1\rangle$  and  $|F = 1, 1\rangle \rightarrow |F = 2, 1\rangle$  are 95 kHz and 189.5 kHz, which correspond to a bias field of 1.35 G.

Each co-propagating transition from  $|1, 0\rangle$  has two smaller peaks which are the Doppler-sensitive counter-propagating transitions. The central peak is shown in more detail in Figure 7.10. The counter-propagating transitions are shifted by -185 kHz and +215 kHz respectively, which correspond to velocities of  $7.2 \text{ cm s}^{-1}$  and  $8.4 \text{ cm s}^{-1}$ . The

---

<sup>1</sup>When the two light fields are co-propagating, the Doppler resonance term  $\delta_D \propto \vec{k}_1 - \vec{k}_2$  is close to zero

$\vec{k}_2$			
	$\sigma^-$	$\pi$	$\sigma^+$
$\vec{k}_1$	$\sigma^-$	$c_1$	$c_2$
	$\pi$	$c_3$	—
	$\sigma^+$	—	$c_4$
		$c_5$	$c_6$

**Table 7.1.:** Labels for Raman transitions excited from  $|F = 1\rangle$  by  $\vec{k}_1$  and stimulated into  $|F = 2\rangle$  by  $\vec{k}_2$ .

$ F = 2, m\rangle$						
	-2	-1	0	1	2	
-1	( $c_2, c_4$ )	( $c_1, c_6$ )	( $c_3, c_6$ )	—	—	—
$ F = 1, m\rangle$	0	—	( $c_2, c_4$ )	( $c_1, c_6$ )	( $c_3, c_6$ )	—
	1	—	—	( $c_2, c_4$ )	( $c_1, c_6$ )	( $c_3, c_6$ )

**Table 7.2.:** Allowed polarisation configurations between each hyperfine ground state Zeeman sub-levels.

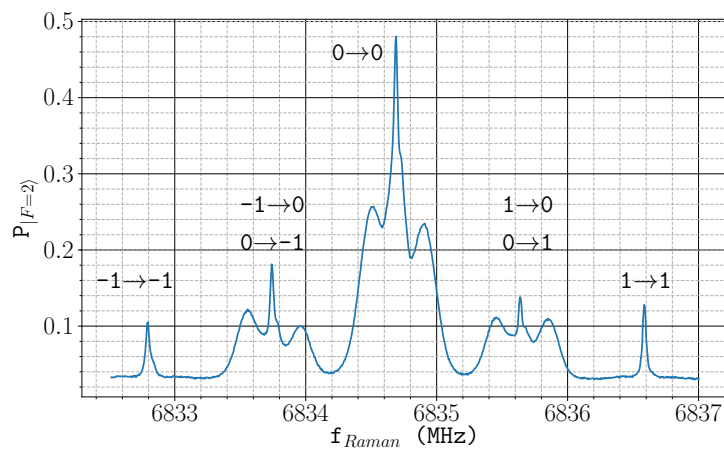


**Figure 7.9.:** Raman transition spectrum, obtained by scanning the beat frequency of the two Raman lasers. The transitions  $|1, m_F\rangle \rightarrow |2, m'_F\rangle$  are indicated at each observed peak.

same Doppler shifts are also observed in the peaks corresponding to the  $|F = 1, m_F = 0\rangle \rightarrow |F = 2, m_F = \pm 1\rangle$  transitions. The counter-propagating transitions are Doppler-broadened by the thermal velocity of the atoms along the direction of the Raman beams. Fitting the transition to the lineshape expected from a thermal distribution of atoms gives a temperature of  $15\text{ }\mu\text{K}$  and  $13.5\text{ }\mu\text{K}$  from each counter-propagating transition. At the time this spectrum was measured, the molasses was not optimised to give the lowest temperature.

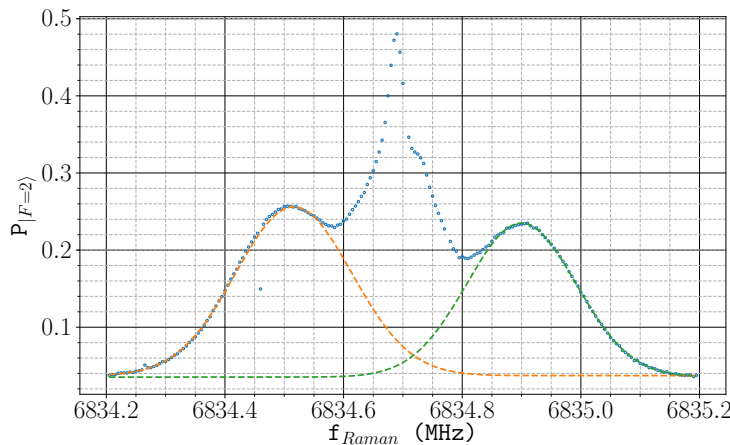


**Figure 7.10.:** Transition spectrum showing the  $\Delta m = 0$  transition from  $|1,0\rangle$ . The orange and green dashed lines are fits to a Doppler-broadened lineshape for each of the counter-propagating profiles.

#### 7.4.2. Cancelling the Differential ac Stark Shift

It is worth considering the effects of ac Stark shifts on the atom interferometer. Firstly, they are intrinsically related to the effective Rabi frequency and as such, cannot be avoided. The average ac Stark shift  $\Omega_{\text{avg}}^{\text{ac}} = (\Omega_1^{\text{ac}} + \Omega_2^{\text{ac}})/2$  (see Section 2.3 for more details) is the same along both paths of the interferometer, provided that the intensity variation of the Raman beams over the path separation can be neglected. Therefore, this should not lead to an observable phase shift.

On the other hand, the differential ac Stark shift  $\delta^{\text{ac}} = \Omega_1^{\text{ac}} - \Omega_2^{\text{ac}}$  can lead to an observable phase shift. Using the results from Ref. [19] for  $\pi$  and  $\frac{\pi}{2}$  pulses, the phase shift to a Mach-Zender type interferometer is

$$\Delta\Phi^{\text{ac}} = \frac{\delta_3^{\text{ac}}}{\Omega_{\text{eff}}} - \frac{\delta_1^{\text{ac}}}{\Omega_{\text{eff}}} \quad (7.13)$$

where  $\delta_3^{\text{ac}}$  and  $\delta_1^{\text{ac}}$  are the ac Stark shifts of the last and first  $\frac{\pi}{2}$  pulses, respectively. Therefore, the interferometer is sensitive to the difference in the ac Stark shift of these pulses.

As the atoms fall under gravity, it is likely that the intensity of the Raman beams during these pulses will not be the same. Fortunately, it is possible to eliminate this differential phase shift using an appropriate choice of intensity and detuning of the Raman lasers. This can be seen by first writing out the differential ac Stark shift

$$\delta^{\text{ac}} = \Omega_1^{\text{ac}} - \Omega_2^{\text{ac}} = \sum_k \frac{|\Omega_{1k}|^2}{4\Delta_{1k}} - \sum_k \frac{|\Omega_{2k}|^2}{4\Delta_{2k}} \quad (7.14)$$

in terms of the one-photon Rabi frequencies  $\Omega_{ik}$  and detunings  $\Delta_{ik}$ . When both Raman beams are red-detuned from all the one-photon transitions, both terms in equation (7.14) are strictly negative. Therefore,  $\delta^{\text{ac}}$  can be cancelled by choosing the correct intensities for each Raman beam. A plot of  $\delta^{\text{ac}}$  for various Raman beam intensities as a function of the ratio between the two Raman beams is shown in Figure 7.11a. There is a ratio at which the differential ac Stark shift cancels and is independent of the total intensity. The ratio that cancels  $\delta^{\text{ac}}$  for increasing two-photon detuning  $\Delta_R$  is shown in Figure 7.11b. When  $\Delta_R$  is 1.13 GHz below the  $|F = 2\rangle \rightarrow |F' = 3\rangle$  transition, this ratio is maximised. The differential ac Stark shift is cancelled when the intensity ratio of light driving  $|1, 0\rangle$  transitions to  $|2, 0\rangle$  transitions is  $\mathcal{R} = 0.583$ .

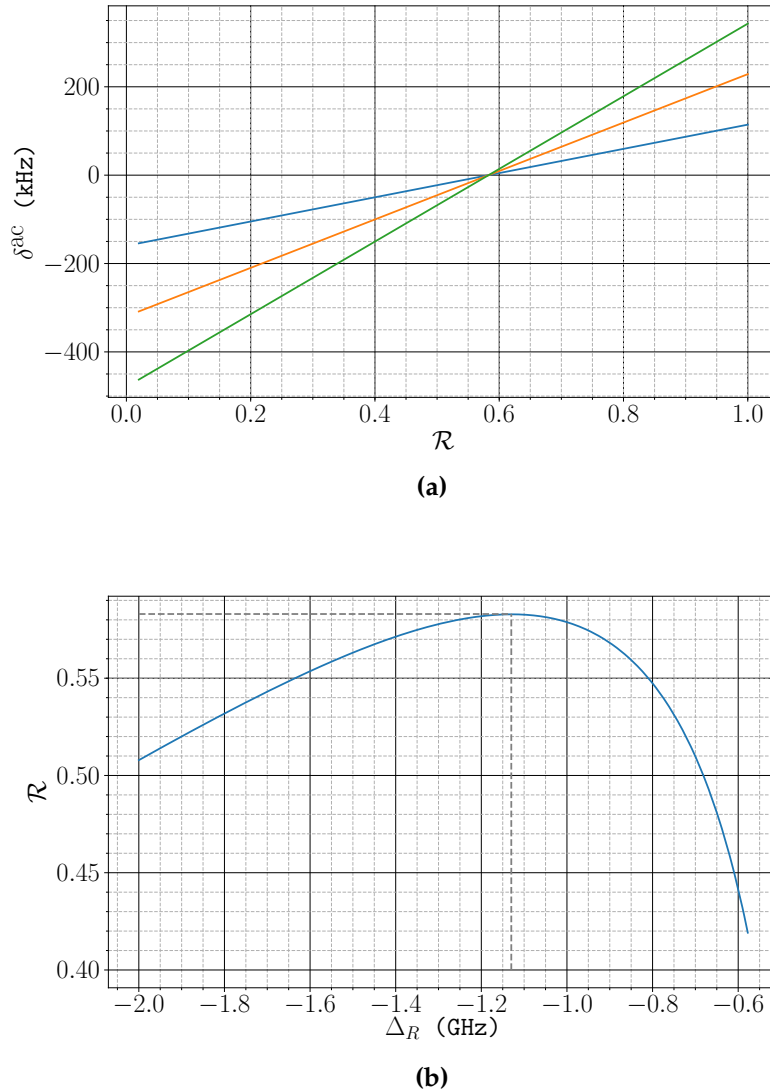


**Figure 7.11.**: The effects of the Raman beam intensities and detuning on the differential ac Stark shift  $\delta^{ac}$ . **(a)** shows  $\delta^{ac}$  as a function of the intensity ratio  $R$  between the light which drives transitions from  $|1,0\rangle$  to the light that couples to  $|2,0\rangle$  for the two-photon detuning of  $\Delta_R = -1.13$  GHz used in the experiment. Example intensities for the  $|2,0\rangle$  light are 100 W m<sup>-2</sup> (blue), 200 W m<sup>-2</sup> (orange) and 300 W m<sup>-2</sup> (green). **(b)** shows how the ratio for which  $\delta^{ac} = 0$  varies as  $\Delta_R$  increases. The dashed lines indicate the value of  $\Delta_R$  used in the experiment and its corresponding ratio of 0.583.

Since it is not straight-forward to directly measure the intensity of each Raman beam on the atoms, a better method to cancel the differential ac Stark shift is to use the transition spectrum to determine when the intensity of the lasers are set to the appropriate ratio. Experimentally, this was done by adjusting the power of the pump lasers for the master and slave Solstis lasers. When the master is seeded with 10 W and the slave with 6.5 W, the differential ac Stark shift is eliminated. Figure 7.12 shows the transition spectrum using two different effective Rabi frequencies, corresponding to  $\pi$  pulse times of 22.5  $\mu$ s and 45  $\mu$ s. In this instance, the frequency difference of the two co-propagating peaks is less than 1 kHz. There is also a shift of 1.4 MHz from  $f_{\text{hfs}}$ . This is

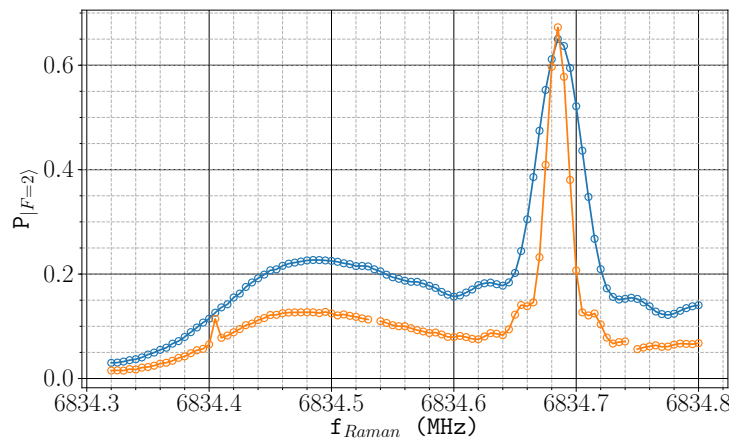


**Figure 7.12.:** Raman transition spectrum after cancelling the differential ac Stark shift. The blue (orange) curve shows a pulse with a  $\pi$  pulse time of 22.5  $\mu$ s (45  $\mu$ s).

a result of a second-order Zeeman shift and corresponds to a field strength of 1.56 G.

### 7.4.3. Velocity-Selective Pulse

The Raman transition is Doppler-sensitive, so the velocity spread of atoms contributes to their dynamics. At a temperature of 6  $\mu$ K, the Doppler width is  $\sigma_f = \frac{2}{\lambda} \sqrt{\frac{k_b T}{m}} \approx 60$  kHz. Coherent control of the atomic state during the interferometer requires that the linewidth of the Raman transition must be much broader than the Doppler width. This

ensures that each atom is driven at approximately the same Rabi frequency, reducing the dephasing rate of the atomic coherence. The linewidth of a Raman transition is determined solely by the pulse intensity and duration. A pulse duration of 7  $\mu\text{s}$  has a linewidth close to the Doppler width, but the intensities required for this are above what is attainable with our Raman laser.

It is possible to reduce the Doppler width of the participating atoms by first applying a Raman pulse to select a subset of the population with a narrower velocity spread [18]. This velocity-selective pulse has a narrower linewidth than the subsequent interferometer pulses. This ensures that the Doppler width of atoms in the interferometer is small compared with the Raman transition linewidth.

Starting with a velocity distribution of atoms described by a 1-D Maxwell-Boltzmann distribution all occupying the  $|1, 0\rangle$  state, the population in  $|2, 0\rangle$  after applying a Raman pulse is distributed according to

$$P_{|2,0\rangle}(v) = \frac{\Omega_{\text{eff}}^2}{\Omega_{\text{eff}}^2 + \delta^2} \sin^2 \left( \sqrt{\Omega_{\text{eff}}^2 + \delta^2} \tau \right) p(v) \quad (7.15)$$

where  $\delta$  is the Raman detuning defined in equation (2.16),  $p(v) = \sqrt{\frac{m}{2\pi k_B T}} e^{-\frac{mv^2}{2k_B T}}$  is the velocity distribution and  $\Omega_{\text{eff}}$  is the effective Rabi frequency defined in equation (2.28). Figure 7.13 shows a simulation of the distribution of atoms driven by a  $\pi$  pulse with a duration of 40  $\mu\text{s}$  and a temperature of 6  $\mu\text{K}$ . The population that is stimulated has a mean velocity shifted by twice the recoil velocity. In this instance, the rms frequency is  $\sigma_f = 19.7 \text{ kHz}$ .

### Velocity-Selected Distribution

The velocity distribution of atoms after the velocity selective pulse can be measured using a second Raman pulse as a probe. In contrast to the interferometer pulses, this

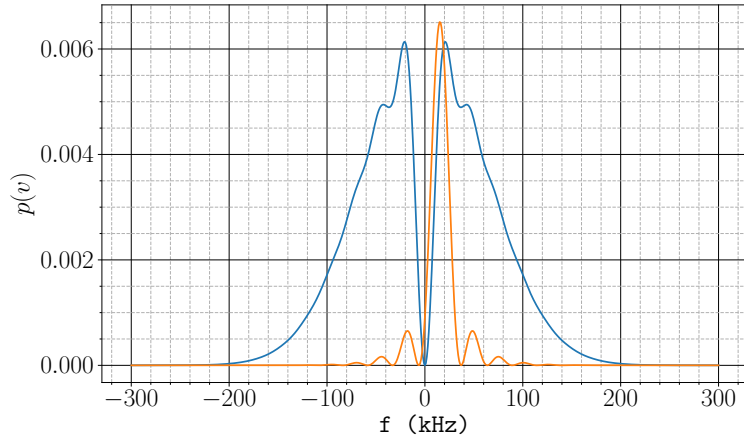


**Figure 7.13.:** Velocity distribution of a  $6 \mu\text{K}$  ensemble of atoms after a  $40 \mu\text{s}$  Raman  $\pi$  pulse. The mean velocity of the stimulated distribution, shown in orange, is increased due to the recoil during the transition.

probe must be much lower power than the velocity-selective pulse so that its linewidth is comparatively narrow. A measurement of the velocity distribution of the atoms is shown in Figure 7.14. An initial  $40 \mu\text{s}$   $\pi$  pulse with a Raman beat frequency  $f_v = 6834.51 \text{ MHz}$  prepares atoms in  $|1, 0\rangle$ , before blowing away the atoms which remain in  $|F = 2\rangle$ . After  $10 \text{ ms}$ , a  $80 \mu\text{s}$   $\pi$  pulse transfers some of the remaining population back into  $|2, 0\rangle$ . The frequency of the probe pulse is varied by chirping the Raman laser beat frequency. In this instance, the power of the pulse was not tuned to give a  $\pi$  pulse area so the measured population is not indicative of the maximum driven by the Raman transition. It is clear that the velocity distribution of the selected atoms is narrower than the initial thermal distribution. Fitting to a 1D Maxwell-Boltzmann distribution gives an effective temperature of around  $1 \mu\text{K}$ .

#### 7.4.4. Interferometer Pulses

The atoms are coherently controlled by pulsing the Raman light to drive Rabi oscillations between the two  $m_F = 0$  hyperfine ground states. The appropriate pulses areas

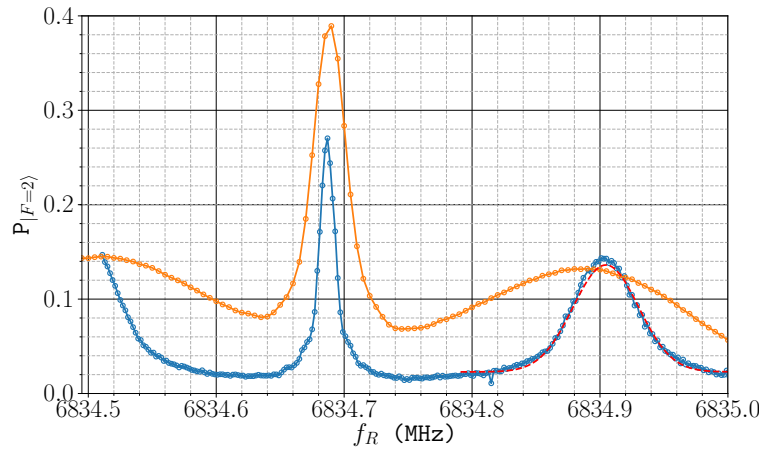


**Figure 7.14.**:  $|F = 2\rangle$  population after a Raman pulse at a frequency  $f_v = 6834.51$  MHz transfers atoms to  $|1, 0\rangle$ . This distribution is probed by applying a narrow pulse at a frequency  $f_R$ . The population measured in  $|F = 2\rangle$  is shown in blue. The red dashed line is a fit to a 1D Maxwell-Boltzmann distribution of the Doppler-broadened transition peak. For comparison, the transition spectrum of a single  $\tau = 40 \mu\text{s}$   $\pi$  pulse is shown in orange.

were empirically determined by observing Rabi oscillations at the corresponding time for each interferometer pulse. These are shown in Figure 7.15. The power in each Raman laser was set so that a  $\pi$  pulse was achieved with a pulse duration of  $\tau = 15 \mu\text{s}$ . It is clear that the oscillations are rapidly damped. This dephasing rate depends on the time at which the pulse is applied. Since the atoms are at different positions in the beam, this suggests that the dephasing is caused by a spatial variation of the Rabi frequency. This is largely a result of irregularities in the Raman beam wavefront from defects in the aspheric lenses. The Gaussian intensity distribution of each beam is unlikely to cause such a fast dephasing, since the atoms remain close to the centre of the beam. At longer pulse durations, spontaneous decay from the intermediate states of the Raman transition becomes apparent.

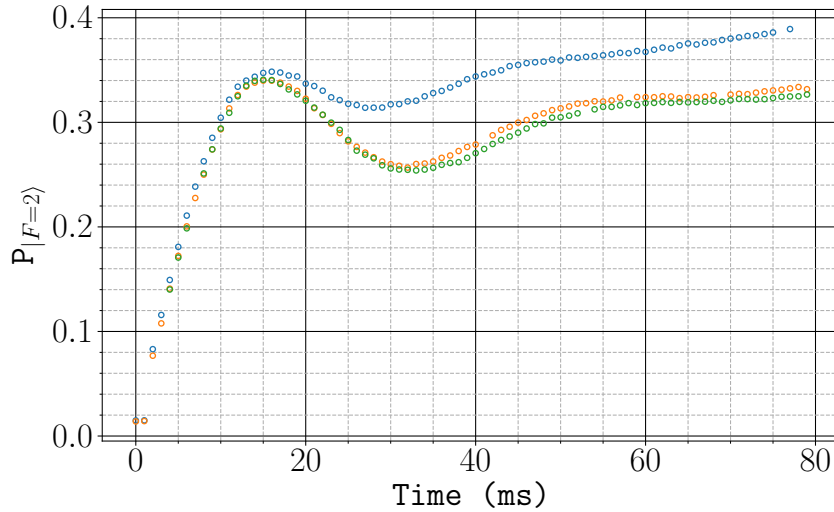


**Figure 7.15.**: Rabi oscillations between the  $|1,0\rangle$  and  $|2,0\rangle$  states. Each pulse occurs at different times after the MOT is released. The times shown are 13 ms (blue), 23 ms (orange) and 33 ms (green). Full population transfer is not observed due to the atoms in  $|1,\pm 1\rangle$  which have not been removed.

## 7.5. Sensitivity

This section presents a discussion of the identified sources of noise in the interferometer and their effects on the sensitivity to accelerations. The Allan variance used to characterise the stability of the interferometer signal is defined in Section 7.5.1. This is followed by an overview of the noise sources in Section 7.5.2. Section 7.5.3 discusses the noise that arises from detecting atoms. The sensitivity function and an analytic method for calculating the influence of random phase fluctuations is given in Section 7.5.4. This is applied to phase noise from the Raman laser in Section 7.5.5 and external vibrations in Section 7.5.6.

### 7.5.1. The Allan Variance

For the purposes of this experiment, the sensitivity of the interferometer relates to the minimum value of uncertainty that can be placed on a measurement of acceleration.

As such, the limit to the sensitivity is given by the measurement noise. One possible way to characterise this is to use the variance. However with a finite sequence of measurements, this depends on the number of samples and might not converge as the number of samples increases. On the other hand, the two-sample variance

$$\sigma_a^2(2, \tau) = \frac{1}{2} \left\langle (a_{n+1} - a_n)^2 \right\rangle \quad (7.16)$$

does not depend on the number of samples. This can be generalized to longer time separations  $t = N\tau$  by taking the mean of  $N$  consecutive measurements

$$\sigma_a^2(2, t) = \frac{1}{2} \left\langle \left( \frac{1}{N} \sum_{k=0}^{N-1} a_{n+1} - \frac{1}{N} \sum_{k=N}^{2N-1} a_n \right)^2 \right\rangle \quad (7.17)$$

which is referred to as the Allan variance [45]. If the noise in each measurement is uncorrelated, then this becomes

$$\sigma_a(2, t) = \frac{1}{\sqrt{N}} \sigma_a(2, \tau) \quad (7.18)$$

The variance is also related to the signal-to-noise ratio of the observed interferometer fringes. From the interferometer signal defined in equation (7.7), the variance at the mid-point of the fringe  $\Delta\phi = \pi/2$  is given by

$$\sigma_P^2 = \sigma_{P_0}^2 + \frac{C^2}{4} \sigma_{\Delta\phi}^2 \quad (7.19)$$

The signal-to-noise ratio

$$\left( \frac{S}{N} \right) = \frac{C}{2\sigma_P} \quad (7.20)$$

is the ratio of the fringe amplitude to the standard deviation of the interferometer signal. Under the assumption that  $P_0$  and  $C$  do not fluctuate, the signal-to-noise ratio is related to the interferometer phase and acceleration uncertainties by

$$\left(\frac{S}{N}\right)^{-1} = \sigma_{\Delta\phi} = \mathbf{k}_{\text{eff}} T^2 \sigma_a \quad (7.21)$$

### 7.5.2. Sources of Noise

Some potential sources of noise have been investigated to determine their magnitude. These are not a complete list of the effects which reduce the sensitivity to accelerations, but are the most dominant. The identified sources and their estimated effects on acceleration measurements are shown in Table 7.3. The largest contributor comes from vibrations of the retro-reflecting mirror. Other noise sources, such as magnetic field gradients, laser intensity noise and rotations have not yet been characterised.

Noise Source	Signal/Noise	$\sigma_a (\mu\text{m s}^{-2})$
Atom shot noise ( $5 \times 10^6$ atoms)	2200	0.07
Laser phase noise	157	1
Detection noise	15	10.5
Vibrations	5.8	26

**Table 7.3.:** Comparison of known noise sources and their effects on acceleration measurements. These values are estimated assuming a separation between pulses of  $T = 25$  ms and a  $\pi/2$  pulse time of  $\tau = 20\ \mu\text{s}$ .

### 7.5.3. Detection Noise

Each measurement of the number of atoms has an uncertainty due to random processes that influence the voltage measured by the detector. These errors combine to

give an uncertainty in the interferometer phase and hence, acceleration. It is worth distinguishing between the different sources of noise in measuring the number of atoms. Uncertainties due to fluctuations in the number of atoms and detected photons per measurement cannot be reduced below their shot-noise levels. In particular, the phase noise corresponding to the atom shot noise is the minimum value attainable. Therefore, it is essential that the photo-detector used is sensitive enough to ensure that this does not limit the sensitivity [46].

### Atom and Photon Shot Noise

The discrete nature and the fact that atoms are loaded into the experiment and scatter photons at a constant rate mean that the statistics on the number of atoms and photons are well-described by Poisson distributions. It follows that the number of atoms in the interferometer as well as the number of photons arriving at the detector during each measurement have shot noise fluctuations. From equation (7.5), these are related to an equivalent output voltage as follows

$$\sigma_{\text{at},v}^2 = \alpha^2 \eta^2 R_{\text{sc}}^2 n_{\text{at}} \quad (7.22)$$

$$\sigma_{\text{p},v}^2 = \alpha^2 \eta R_{\text{sc}} n_{\text{at}} \quad (7.23)$$

where  $\sigma_{\text{at},v}$  dominates, provided at least one photon per atom is detected. Hereafter, no attention will be paid to the photon shot noise. For the detection parameters previously defined, the shot noise is equal to around 46.5 nV per atom.

In order for the uncertainty in the atom number to be dominated by the atom shot noise, the detector must be sensitive enough that it has a noise-equivalent power (**NEP**) much lower than the noise in the optical power detected. The **NEP** of a detector is defined as the equivalent optical power which gives a signal-to-noise ratio of 0 after

an integration time of 0.5 s. It is convenient to express this as a voltage density, by multiplying it by the photodiode gain. Hence, the voltage density of a detector whose sensitivity is at the atom shot noise level for an integration time  $\tau u_D$  is given by

$$V_{\text{at}} = \frac{\sigma_{\text{at},v}}{\sqrt{1/2\tau_D}} \quad (7.24)$$

### Photodiode Technical Noise

Technical noise in the detector typically arises from multiple electronic processes – such as Johnson noise and shot noise in the current – but it is not necessary to consider them independently in the following discussion. The technical noise of the detector can be estimated by measuring the output voltage when no light is collected. A plot of the power spectral density of the photodiode is shown in Figure ?? taken with a sampling frequency of 200 kHz. The photodiode was covered and the output voltage was sampled for 2 s. The power spectral density has been calculated using Welch's method [47]. The data are partitioned before calculating the Fourier transform of each subset and taking the average. This has the effect of reducing the variance in the estimated power spectrum at the expense of reducing the frequency resolution. Below 10 kHz the power spectral density is close to uniform with a value of around  $5 \times 10^{-13} \text{ V}^2 \text{ Hz}^{-1}$ , which corresponds to a noise-equivalent power of  $391 \text{ fW Hz}^{-1/2}$ . For higher frequencies, the power spectral density starts to increase. The plot also indicates the corresponding voltage noise density to reach the atom shot noise limit for atom numbers of  $n_{\text{at}} = 5 \times 10^6$  and  $1 \times 10^6$  with the previously defined output voltage per atom. Averaging the detection signal over a time  $\tau$  has the effect of filtering the signal above the Nyquist frequency  $f_n = 1/(2\tau)$ . The variance in the averaged voltage over successive shots i.e. the Allan variance, is related to the power

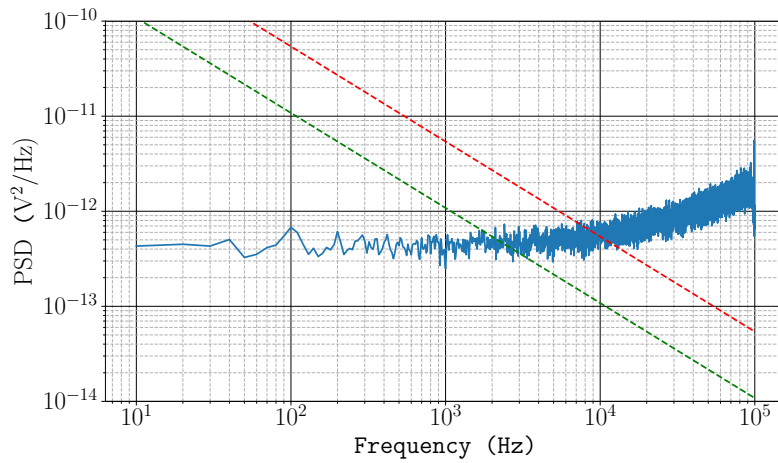


**Figure 7.16.**: Power spectral density of the photodiode output voltage sampled for 2 s at a rate of 200 kHz. The red and green dashed lines indicate the required voltage noise density to equal the atom shot noise level after integrating for  $\tau = 2/f$  for atom numbers of  $5 \times 10^6$  and  $1 \times 10^6$ , respectively.

spectral density as follows

$$\sigma_{\text{av}}^2(\tau) = 2 \int_0^\infty \frac{\sin(\pi\tau f)^4}{(\pi\tau f)^2} S(f) \, d f \quad (7.25)$$

Using equation (7.25), it is possible to determine the detection time required to reduce the shot-to-shot variance below the atom shot noise level. Figure 7.17 shows the Allan deviation for increasing integration time, along with the rms voltage expected for the same numbers of atoms used in Figure 7.16. At the integration time of 200  $\mu$ s, the detector noise is close to 5  $\mu$ V – well below the level of the atom shot noise.

#### 7.5.4. The Sensitivity Function

The sources of noise presented thus far arise from statistical uncertainties in measuring the number of atoms and are not present in the ideal case of perfect interferometer contrast. However, there are still other sources which introduce interferometer phase noise. Generally speaking, these add a random component to the interferometer phase

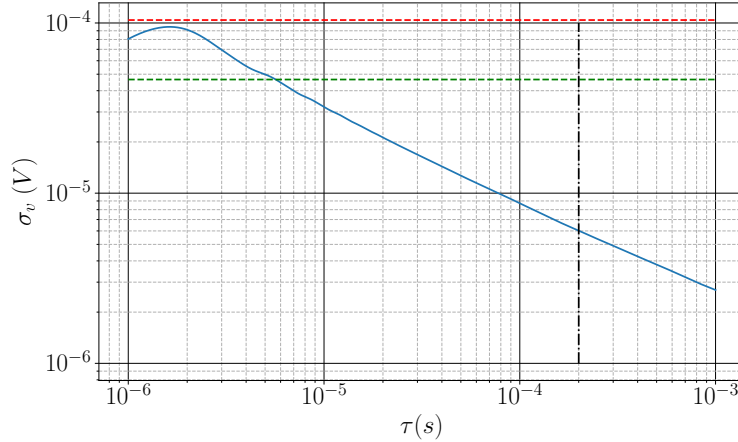


**Figure 7.17.:** Allan variance of the Photodiode voltage for increasing integration time  $\tau$ . The red and green dashed lines are the atom shot noise rms voltages for the values used in Figure 7.16. The black dot-dashed line indicates the integration time of 200  $\mu\text{s}$  used in the experiment.

which is independent of the forces acting on the atoms. Two dominant sources of phase noise are vibrations of the retro-reflecting mirror and laser phase noise, i.e. fluctuations in the relative phase between the two Raman light fields.

The sensitivity function [48] defines the instantaneous shift of the interferometer phase  $\delta\Phi$  at a time  $t$  due to a phase shift of the Raman laser phase  $\delta\phi$

$$g(t) = \lim_{\delta\phi \rightarrow 0} \frac{\delta\Phi(\delta\phi, t)}{\delta(\phi)} \quad (7.26)$$

so the interferometer phase shift induced by fluctuations of  $\phi$  is given by

$$\begin{aligned} \Phi &= \int_{-\infty}^{\infty} g(t)\delta\phi \, d\phi(t) \\ &= \int_{-\infty}^{\infty} g(t) \frac{d\phi}{dt} \, dt \end{aligned} \quad (7.27)$$

In the case of a  $\pi/2 - \pi - \pi/2$  interferometer pulse sequence of durations  $\tau_R - 2\tau_R - \tau_R$  and where  $t = 0$  is defined at the centre of the  $\pi$  pulse, the sensitivity function is

$$g(t) = \begin{cases} \sin(\Omega t) & 0 < t < \tau_R \\ 1 & \tau_R < t < \tau_R + T \\ \sin(\Omega(t - T)) & \tau_R + T < t < 2\tau_R + T \end{cases} \quad (7.28)$$

for a pulse separation time  $T$ .

### 7.5.5. Influence of Laser Phase Noise

The response of the interferometer phase to laser phase noise is best understood in the frequency domain. In particular, the inverse of the interferometer pulse separation time. The effects of  $\phi$  are best thought of in terms of its Fourier components. Writing  $\phi(t) = A \cos(\omega t + \psi)$ , equation (7.27) becomes

$$\Phi = -A\omega \cos(\psi) \int_{-\infty}^{\infty} g(t) \sin(\omega t) dt \quad (7.29)$$

where the term proportional to  $\cos(\omega t)$  has been dropped, since  $g(t)$  is an odd function. The integrand in equation (7.29) is proportional to the Fourier transform of  $g(t)$

$$G(\omega) = -i \int_{-\infty}^{\infty} g(t) \sin(\omega t) dt \quad (7.30)$$

which using equation (7.28) becomes [49]

$$G(\omega) = \frac{4i\Omega}{\omega^2 - \Omega^2} \sin\left(\frac{\omega(T + 2\tau)}{2}\right) \left( \cos\left(\frac{\omega(T + 2\tau)}{2}\right) + \frac{\omega T}{2} \sin\left(\frac{\omega T}{2}\right) \right) \quad (7.31)$$

so equation (7.27) becomes

$$\begin{aligned}\Phi &= -iA \cos(\psi) \omega G(\omega) \\ &= -A \cos(\psi) |H(\omega)|\end{aligned}\quad (7.32)$$

A plot of the transfer function  $|H(\omega)|^2$  is presented in Figure 7.18 for  $T = 20\text{ ms}$  and  $\tau = 20\mu\text{s}$ . The asymptotic properties of the transfer function can be summarised as follows:

- At low frequencies  $\omega \ll \Omega$ , the transfer function is approximated by

$$|H(\omega)|^2 \approx 16 \sin\left(\frac{\omega T}{2}\right)^4 \quad (7.33)$$

which is a periodic function that is zero at frequency multiples of  $1/\pi T$

- At frequencies  $\omega \gg \Omega$ , the transfer function is

$$|H(\omega)|^2 \approx 4 \frac{\Omega^2}{\omega^2} \sin(\omega T)^2 \quad (7.34)$$

which is zero at multiples of  $1/2\pi T$  and is a low-pass first-order filter.

The variance of  $\Phi$  is obtained by averaging over  $\psi$

$$\sigma_\Phi^2 = \langle \Phi^2 \rangle_\psi = \frac{1}{2} A^2 |H(\omega)|^2 \quad (7.35)$$

which is related to the phase noise power spectral density  $S_\phi(\omega)$  by

$$\sigma_\Phi^2 = \frac{1}{2} \int_{-\infty}^{\infty} S_\Phi(\omega) |H(\omega)|^2 \frac{d\omega}{2\pi} = \int_0^{\infty} S_\Phi(\omega) |H(\omega)|^2 \frac{d\omega}{2\pi} \quad (7.36)$$

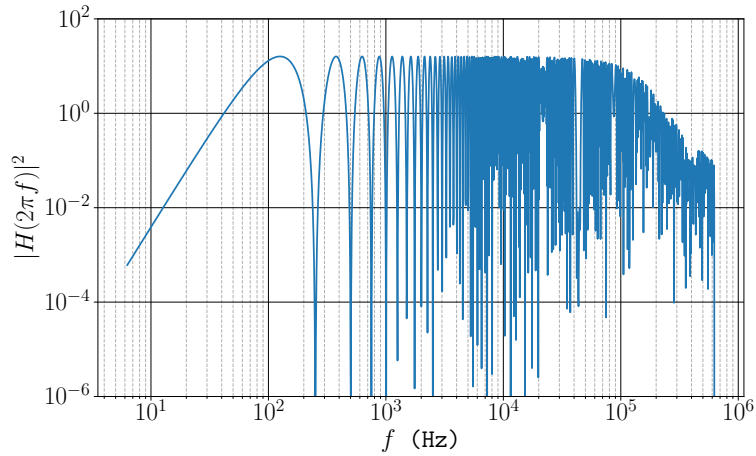


**Figure 7.18.**: Transfer function for laser phase noise. Here, the separation between pulses is  $T = 20\text{ ms}$  and the  $\pi/2$  pulse time is  $\tau = 20\text{ }\mu\text{s}$ .

Similarly, the Allan variance can be expressed using the transfer function and the phase noise power spectral density [50]. The integration time  $\tau_{\text{av}} = mT_c$  is expressed in multiples of the experiment cycling time  $T_c$ . In the frequency domain, the phase noise power spectral density is sampled at frequency multiples of  $f_c = 1/T_c$ , so the Allan variance becomes

$$\sigma_\Phi^2(\tau_{\text{av}}) = \frac{1}{\tau_{\text{av}}} \sum_{k=1}^{\infty} |H(2\pi kf_c)|^2 S_\phi(2\pi kf_c) \quad (7.37)$$

The laser phase noise originates from the reference oscillator used in the phase-locked loop for the M-Squared laser. The phase noise spectral density and corresponding Allan deviation for increasing integration time was measured by M-Squared during installation of the laser system. A plot of the Allan deviation is shown in Figure 7.19. At an interferometer pulse separation of  $T = 25\text{ ms}$ , the phase noise in the Raman laser results in an uncertainty in the interferometer phase of 10 mrad.

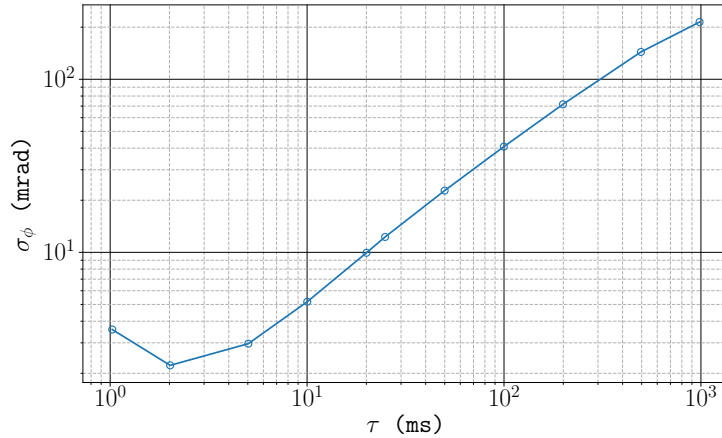


**Figure 7.19.:** Allan deviation of the Raman laser phase difference for increasing integration time. Data reproduced from [?].

### 7.5.6. Vibrations

The phase difference between the two Raman beams depends on the position of the retro-reflecting mirror. Consequently, this defines a frame of reference for the position of the atoms during the interferometer. Any random motion of the mirror, for instance from mechanical vibrations, introduces a random component to the laser phase [51]. An acceleration of the mirror modifies the laser phase as follows

$$\frac{d^2\Phi(t)}{dt^2} = \mathbf{k}_{\text{eff}} \cdot \mathbf{a}(t) \quad (7.38)$$

and the sensitivity to accelerations  $g_a$  is given by

$$\frac{1}{k_{\text{eff}}} \frac{d^2 g_a(t)}{dt^2} = g(t) \quad (7.39)$$

$$(7.40)$$

Assuming that the pulse time  $\tau$  is much shorter than the interferometer pulse separation,  $T$ , the acceleration sensitivity function is approximated by

$$g_a(t) = \begin{cases} -1 & -T < t < 0 \\ 1 & 0 < t < T \end{cases} \quad (7.41)$$

From this, the acceleration transfer function is

$$|H_a(\omega)|^2 = \frac{k_{\text{eff}}^2}{\omega^2} |H(\omega)|^2 \quad (7.42)$$

which in the low frequency limit  $\omega \ll \Omega$  is

$$|H_a(\omega)|^2 = \frac{16k_{\text{eff}}^2}{\omega^4} \sin^2\left(\frac{\omega T}{2}\right)^4 \quad (7.43)$$

Equivalent definitions for the variance and Allan variance are obtained using this and the acceleration noise spectral density  $S_a(2\pi f)$  as the respective definitions in equation (7.36) and equation (7.37). The transfer function for acceleration noise is shown in Figure 7.20. The gain is largest at low frequencies and approximates a second-order filter at higher frequencies.

### Measuring the Acceleration Noise Power Spectral Density

The interferometer phase is most sensitive to low-frequency vibrations. Acceleration noise at frequencies greater than  $1/2T$  will mostly average out, contributing little to an overall phase. Precise measurements of the interferometer phase rely on reducing the low frequency noise. The vibration of the retro-reflecting mirror is reduced by passively isolating it from its environment. The chamber is mounted on a layer of

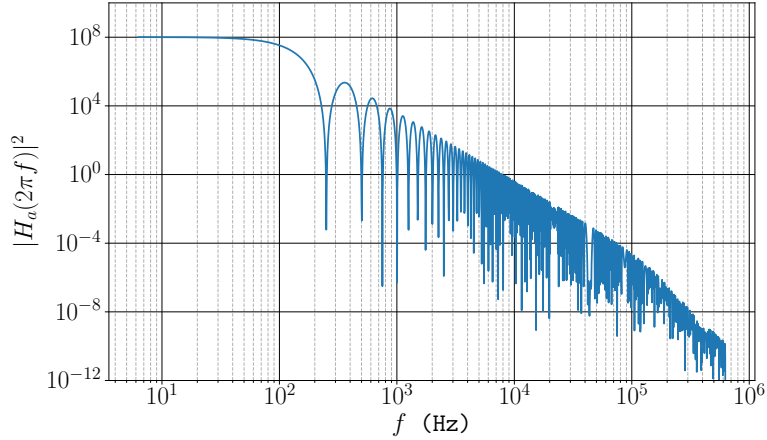


**Figure 7.20.:** Acceleration noise transfer function. The parameters used here are the same as those previously defined for Figure 7.18.

Sorbothane to dissipate the vibrations from the ground. This isolation is enhanced by a pneumatic suspension system between the optical table and its supporting legs.

A comparison of the acceleration noise spectral density with and without the pneumatic suspension, measured using the accelerometer mounted behind the retro-reflecting mirror, is shown in Figure 7.21. The suspension acts as a low-pass filter and reduces the power within the 10-200 Hz bandwidth, which is aliased into the lower frequency band. For an interferometer pulse separation of  $T = 25$  ms, the vibration phase noise using equation (7.37) is  $\sigma_\Phi = 270$  mrad. Without floating the table, this becomes 7 rad. With the vibration isolation systems currently used, this remains the dominant source of phase noise. More sophisticated methods of damping low-frequency vibrations are required to improve the interferometer's acceleration sensitivity.

## 7.6. Measuring Accelerations

This section presents the techniques used to characterise the atom interferometer and its sensitivity to accelerations. It begins with a calibration of the fringe pattern

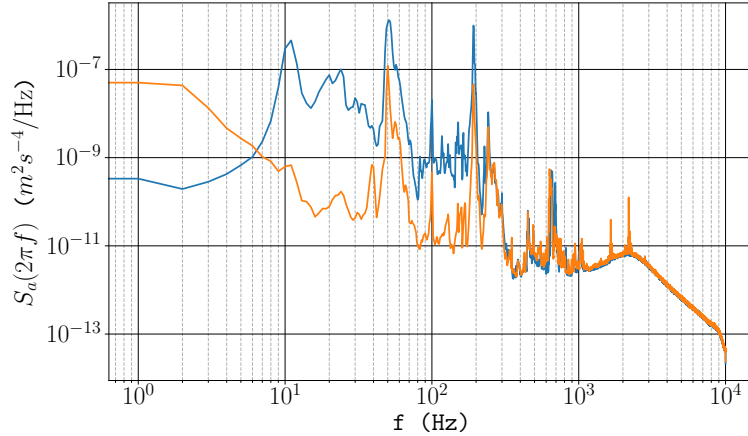


**Figure 7.21.:** Acceleration noise power spectral density sampled at a rate of 20 kHz. The orange curve shows the acceleration power spectral density using pneumatic suspension to decrease the coupling of vibrations from the ground to the experiment. For comparison, the blue curve shows the power spectral density without this isolation.

in Section 7.6.1. Following this, a method for filtering the effects of vibrations is given in Section 7.6.2. This section concludes with a measurement of the Allan variance to determine the long-term stability in Section 7.6.3.

### 7.6.1. Fringe Calibration

Without perfect fringe visibility, the interferometer signal must first be calibrated to infer the phase difference [52]. This is done by varying the phase difference between the two Raman lasers for the middle  $\pi$  pulse. Since the interferometer phase is  $\Delta\Phi = \phi_1 - 2\phi_2 + \phi_3$ , varying  $\phi_2$  induces the largest change in  $\Delta\Phi$ . Figure 7.22 shows an interference fringe obtained in this manner. In this instance, the contrast is  $C = 0.055$  and the mean probability of detecting in  $|F = 2\rangle$  is  $P_0 = 0.39$ .

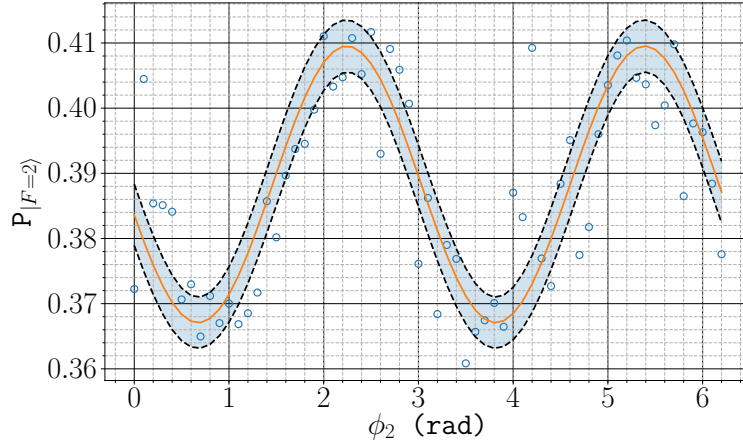


**Figure 7.22.:** Interference fringe obtained by varying the phase difference of the two Raman lasers during the middle  $\pi$  pulse for a pulse separation time of  $T = 25$  ms. The orange curve is a non-linear least squares fit to the data, giving a contrast of  $C = 0.055$  and a mean value of  $P_0 = 0.39$ . The shaded region indicates the 95% confidence band.

### 7.6.2. Correcting for Vibration Noise

Vibrations of the retro-reflecting mirror are a significant source of phase noise, which limits the sensitivity of the interferometer to accelerations. This is particularly apparent when the vibration noise induces a phase shift of greater than  $2\pi$  radians. If the interferometer signal spans multiple fringes, it is not possible to accurately determine acceleration from the phase shift.

One method to filter the effects of vibration noise, described in [12], uses the MEMS accelerometer to measure the vibration of the retro-reflecting mirror between the first and last interferometer pulse. After this time, the phase shift due to vibrations is given by the following convolution

$$\phi_{\text{vib}} = \mathbf{k}_{\text{eff}} T^2 K \int_{-T}^T g_a(t) V(t) dt = \mathbf{k}_{\text{eff}} T^2 K \tilde{V}_{\text{vib}} \quad (7.44)$$

where  $V(t)$  is the voltage measured across the output of the MEMS accelerometer,  $K = 0.793 \text{ m s}^2 \text{ V}^{-1}$  is the scaling factor from voltage to acceleration and  $g_a(t)$  is the acceleration sensitivity function, defined in equation (7.41). Leaving the scaling factor as a free parameter  $\alpha$ , the interferometer signal is fit to the function

$$P_{|F=2\rangle} = P_0 + \frac{C}{2} \sin(\alpha \tilde{V}_{\text{vib}} + \phi_0) \quad (7.45)$$

Common-mode suppression of the vibration phase noise is achieved by estimating the interferometer phase from the residuals of the fit to equation (7.45). If the interferometer phase as estimated from equation (7.7) is denoted  $\phi_{\text{int}}$ , then the fit residuals are  $\phi_{\text{res}} = \phi_{\text{int}} - \phi_{\text{vib}}$ . The correlation of the acceleration measured by the MEMS accelerometer and the interferometer signal is shown in Figure 7.23. The Raman laser phase difference was initially set so that the interferometer signal was at the mid-point of the fringe  $\Delta\phi = \pi/2$  before continuously running the experiment. The vibration noise was increased by removing the pneumatic suspension of the optical table, which helps to passively isolate the experiment from external vibrations that are coupled through the table legs. Without this additional suppression, the vibration noise is large enough to shift the interferometer phase by more than  $2\pi$ , as indicated in Figure 7.23a. When the table is suspended, the vibration noise is small enough that the interferometer signal remains on one side of the fringe.

The suppression of the vibration noise can be seen in the distribution of the estimated acceleration. Figure 7.24 shows histograms of the acceleration measured by the MEMS and the interferometer in the low vibration instance of Figure 7.23b. Figure 7.24a compares the distribution of the accelerations measured by the MEMS with that of the interferometer. The noise in the MEMS signal is larger than in the interferometer – their respective standard deviations are  $\sigma_a^{(m)} = 66.8 \mu\text{m s}^{-2}$  and  $\sigma_a^{(i)} = 20.8 \mu\text{m s}^{-2}$ . The MEMS accelerometer has a higher acceleration bandwidth (20 kHz) than the

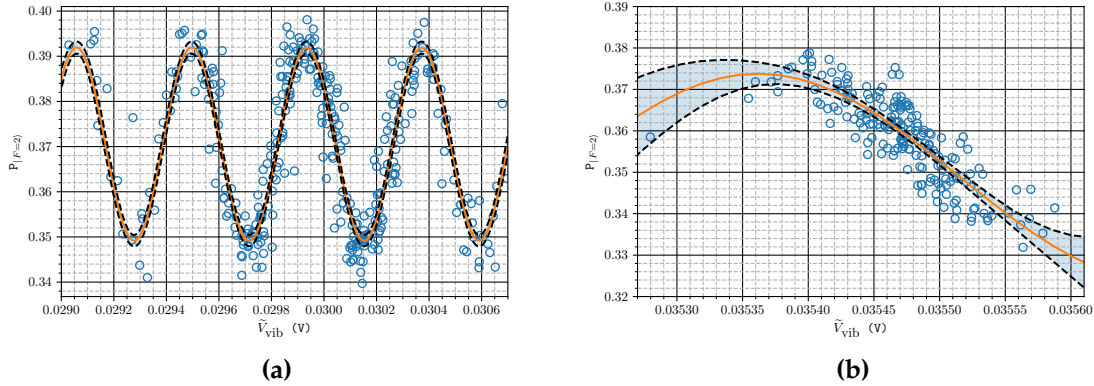


**Figure 7.23.:** Correlation between acceleration measured by the MEMS accelerometer and the interferometer signal. **(a)** shows the correlation measured in high vibration environment, when the optical table was not pneumatically suspended. **(b)** shows the reduction in phase noise with this additional vibration isolation.

interferometer (20 Hz). Consequently, the interferometer is not sensitive to the high-frequency noise measured by the MEMS accelerometer. Figure 7.24b compares the acceleration noise from the interferometer with the acceleration inferred from the fit residuals  $\phi_{\text{res}}$ . The latter has a standard deviation of  $\sigma_a^{(r)} = 10.4 \mu\text{m s}^{-2}$ . This method is able to filter the effects of vibration from the interferometer signal. However, the non-linear least squares method assumes that there is no error in the independent variable  $\tilde{V}_{\text{vib}}$ . This introduces a random error to  $\phi_{\text{res}}$  from the noise intrinsic to the MEMS accelerometer. A weighted least-squares fit [53] is able to account for errors in both variables. This requires an accurate estimate of the weights for each measurement of  $\tilde{V}_{\text{vib}}$  and  $P_{|F=2\rangle}$  to avoid inaccurate parameter estimates.

### 7.6.3. Signal Stability

The stability of the interferometer's sensitivity to accelerations can be determined from the Allan deviation. A comparison of the Allan deviation in the presence of high and low vibrations is shown in Figure 7.25. In both instances, the sensitivity

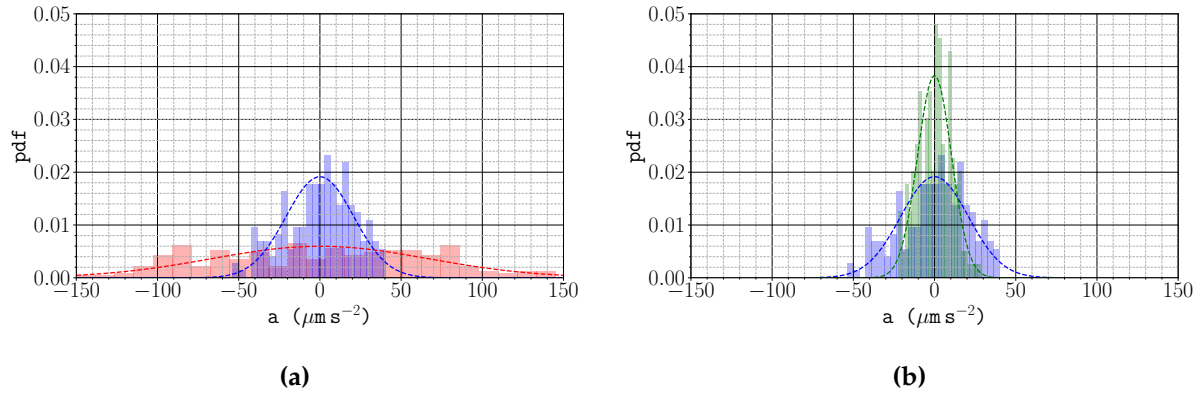


**Figure 7.24.**: Histograms of the acceleration measured in Figure 7.23b. **(a)** shows the distribution of the acceleration measured by the MEMS accelerometer (red) and the interferometer (blue). **(b)** shows the distribution after filtering the vibration noise from the interferometer signal (green). The dashed lines indicate the fitted normal distributions.

to accelerations is improved by correcting for the vibration-induced phase. Under high vibration (Figure 7.25a), the Allan deviation has a minimum value of around  $3 \times 10^{-6} \text{ m s}^{-2}$  after integrating for 35 s. This is a bias instability, i.e. fluctuations in the bias. This value is obtained by subtracting the vibration phase, estimated from the MEMS accelerometer, from the interferometer phase. There is additional noise in the MEMS accelerometer which leads to this bias instability. At short integration times, the Allan deviation has a  $\tau^{-1}$  dependence. This is characteristic of Flicker noise [54] which exhibits stronger correlations than other random processes, such as white noise.

Figure 7.25b shows the Allan deviation in the case of smaller vibrations. In contrast to the previous case, the signal remains stable for a longer period of time. The Allan deviation is proportional to  $\tau^{-1/2}$ , which is characteristic of uncorrelated white phase noise. At longer integration times, the small number of samples introduces a large uncertainty on the Allan deviation. For times up to 100 s, the sensitivity of the signal is not limited by bias instability.

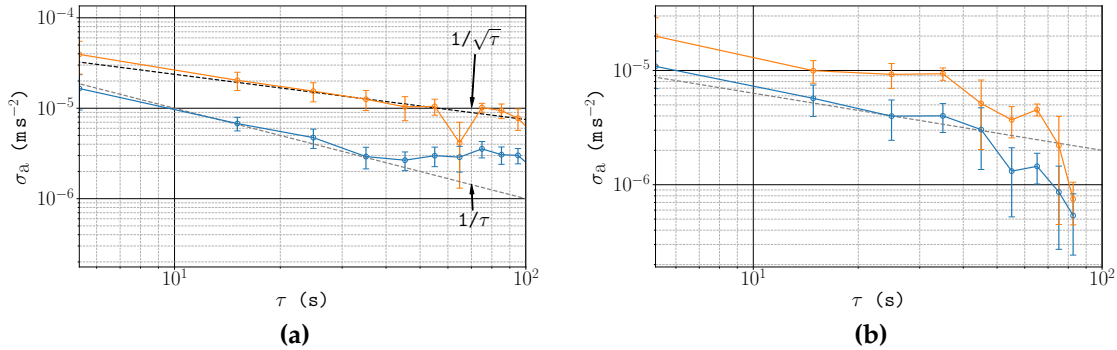


**Figure 7.25.**: Allan deviation of the estimated acceleration using the interferometer signal. In each plot the orange curve represents the sensitivity to accelerations without subtracting the vibration induced phase, and the blue curve shows the sensitivity after subtracting this. As in Figure 7.23, (a) shows the sensitivity in a high vibration environment, and (b) shows it after reducing the level of vibration.

## 7.7. Conclusion

This chapter has described the methods used to observe matter-wave interference. It has presented a description of the Raman laser system and the scheme used to infer the population in each internal state. The light pulses used to drive Raman transitions were subsequently presented, to emphasise the effect of a light shift and background atoms on the interferometer. A further discussion of identified noise sources showed that vibrations are the largest contributor. The interference between two states was characterised

# **Chapter 8.**

## **Outlook**

### **8.1. Conclusions**

This project set out to explore the use of atom interferometry for inertial navigation. The specific aim was to demonstrate sensitivity to horizontal accelerations where gravitational acceleration acts perpendicularly to the sensitive axis. Requirements for a high measurement bandwidth and low dead time influenced the development of the experiment.

The dead time between measurements is reduced by loading the atoms from a 2D MOT and through an improved design of the control software. Using a 2D MOT reduces the time required to load a sufficient number of atoms when compared to loading from a background vapour. The hardware that controls the experiment regenerates the necessary voltage patterns, removing the need for additional time to re-calculate the experimental sequence. This enables the loading of  $10^8$  atoms into the 3D MOT after 100 ms. With a maximal interrogation time of  $2T = 50$  ms, the interferometer can be operated up to a rate of 4 Hz, which corresponds to a duty cycle of 20%. With

further optimisation of the 2D MOT system, such as increased cooling beam power, it is possible to increase the atomic flux and hence increase the experiment cycling rate.

The design of the in-vacuum optical system for the interferometer light pulses ensures that the fringe visibility is not lost due to transverse motion of the atoms. Wavefront distortions of the interferometer light pulses are minimised by not requiring optical viewports between the Raman laser and the atoms. The beams are also collimated to a large waist size to reduce dephasing of the atoms from an intensity gradient. A beam waist of at least 34 mm necessitated an aspheric lens pair in the collimation optics train. These lenses are not manufactured to the same optical quality as the triplet lens. It was found that they introduced an irregular intensity distribution of the laser which led to dephasing of the atomic states. An improved optical system has been designed by Shane de Souza, the latest student on this experiment. It is anticipated that this will improve the wavefront quality for the interferometer light pulses.

The sequence of optical and microwave pulses that prepares atoms in the  $|1, 0\rangle$  state is very effective at increasing the population in the  $m_F = 0$  state beyond the fraction expected after an optical molasses. Despite this, there remains a residual population in the  $|1, \pm 1\rangle$  states. These are detected as a background, which reduces the interferometer fringe contrast. Since preparing this thesis, the state preparation sequence has been improved by increasing the polarisation purity of the light driving the  $|F = 1\rangle \rightarrow |F' = 0\rangle$  transition. There is now less de-population of the  $|1, 0\rangle$  state due to  $\pi$ -transitions.

It has been possible to observe interference with a fringe contrast of around 5%. This admittedly low value is likely due to the reasons stated above. In fact, since reducing the  $|1, \pm 1\rangle$  population, the fringe contrast has increased to around 20%. Further details of this can be found in Xiaxi Cheng's PhD thesis [55].

The sensitivity to horizontal accelerations was demonstrated by comparing the interferometer signal in differing levels of vibration noise. This also highlighted the importance of vibration isolation for accurate acceleration measurements. When the phase noise is larger than  $2\pi$  rad, it is not possible to accurately estimate acceleration using the interferometer signal. An auxiliary measurement from a classical sensor is needed to filter the vibration noise. After correcting for this phase noise, it was found that the stability of the interferometer signal improved, particularly when the noise was smaller than  $\pi$  rad - a half-side of a fringe.

## 8.2. Avenues of Further Research

Although this work represents the first step towards inertial navigation using atom interferometry, there is still more to be done. Further work is planned to extend this system measure accelerations along 3 axes. This requires a modification of the Raman laser system so that it can provide enough power from three outputs. This configuration will need to account for the orientation of the accelerometer. If the direction of gravity is not accurately known, it will bias the acceleration measured by the accelerometer, depending on its orientation. This is a known problem in inertial navigation. An error in orientation leads to a position error that oscillates periodically, known as a Schuler oscillation [56]. Orienting the accelerometer using a gyroscope will help to improve the position accuracy, particularly over durations longer than the Schuler period  $2\pi\sqrt{R_{\text{Earth}}/g} \approx 84.4$  min.

A comparison of the interferometer's performance to conventional accelerometers will greatly benefit research aimed towards practical applications of atom interferometry. This has already been demonstrated in the context of gravimeters [57, 58], where a mobile atomic system has demonstrated greater insensitivity to vibration noise and

better short-term stability than the state-of-the-art classical counterpart. Additionally, this interferometer has yet to be tested outside of a laboratory environment. A recent experiment has investigated the bias stability of a hybrid sensor in a simulated harsh environment [59]. An extension of this work to measuring a range of accelerations would further support the viability of cold atom inertial sensors.

### 8.3. Concluding Remarks

The application of newly understood physics has often led to the development of more advanced technology. In turn, this has contributed to further progress in scientific disciplines, and society in general. This philosophy can be applied to the application of matter-wave interferometry to inertial sensing. There already exists a significant body of research that demonstrates the technical feasibility of measuring inertial forces using cold atomic systems. In addition, the practical requirements for navigation have served to identify a need for the unique benefits of atom interferometers. This work presented in this thesis has helped to address this need. It is anticipated that the application of quantum mechanics to technology will bring practical benefits as well as enable a deeper understanding of physical phenomena.



## **Appendix A.**

### **$\mu$ Quans Laser Serial Commands**



# Bibliography

- [1] L. ESSEN and J. V. L. PARRY, "An Atomic Standard of Frequency and Time Interval: A Cæsium Resonator", *Nature* **176** (aug, 1955) 280–282, [doi:10.1038/176280a0](https://doi.org/10.1038/176280a0).
- [2] J. Levine and T. Parker, "The algorithm used to realize UTC(NIST)", in *Proceedings of the 2002 IEEE International Frequency Control Symposium and PDA Exhibition (Cat. No.02CH37234)*, pp. 537–542. IEEE. [doi:10.1109/FREQ.2002.1075941](https://doi.org/10.1109/FREQ.2002.1075941).
- [3] C. Bordé, "Atomic interferometry with internal state labelling", *Physics Letters A* **140** (sep, 1989) 10–12, [doi:10.1016/0375-9601\(89\)90537-9](https://doi.org/10.1016/0375-9601(89)90537-9).
- [4] M. Kasevich and S. Chu, "Atomic Interferometry Using Stimulated Raman Transistions", *Physical Review Letters* **67** (mar, 1991) 181–184, [doi:10.1103/PhysRevLett.67.181](https://doi.org/10.1103/PhysRevLett.67.181).
- [5] M. Kasevich and S. Chu, "Measurement of the Gravitational Acceleration of an Atom with a Light-Pulse Atom Interferometer", *Applied Physics B* **332** (1992) 321–332.
- [6] D. S. Durfee, Y. K. Shaham, and M. A. Kasevich, "Long-Term Stability of an Area-Reversible Atom-Interferometer Sagnac Gyroscope", *Physical Review Letters* **97** (dec, 2006) 240801, [doi:10.1103/PhysRevLett.97.240801](https://doi.org/10.1103/PhysRevLett.97.240801).
- [7] F. A. Faruqi and K. J. Turner, "Extended Kalman filter synthesis for integrated global positioning/inertial navigation systems", *Applied Mathematics and Computation* **115** (oct, 2000) 213–227, [doi:10.1016/S0096-3003\(98\)10068-1](https://doi.org/10.1016/S0096-3003(98)10068-1).
- [8] A. V. Rakholia, H. J. McGuinness, and G. W. Biedermann, "Dual-axis, high data-rate atom interferometer via cold ensemble exchange", [arXiv:1407.3847](https://arxiv.org/abs/1407.3847).
- [9] G. W. Biedermann, H. J. McGuinness, A. V. Rakholia et al., "Atom

- Interferometry in a Warm Vapor”, *Physical Review Letters* **118** (apr, 2017) 163601, [doi:10.1103/PhysRevLett.118.163601](https://doi.org/10.1103/PhysRevLett.118.163601).
- [10] C. JEKELI, “Navigation Error Analysis of Atom Interferometer Inertial Sensor”, *Navigation* **52** (mar, 2005) 1–14, [doi:10.1002/j.2161-4296.2005.tb01726.x](https://doi.org/10.1002/j.2161-4296.2005.tb01726.x).
- [11] I. Dutta, D. Savoie, B. Fang et al., “Continuous Cold-Atom Inertial Sensor with 1 nrad/sec Rotation Stability”, *Physical Review Letters* **116** (may, 2016) 183003, [doi:10.1103/PhysRevLett.116.183003](https://doi.org/10.1103/PhysRevLett.116.183003).
- [12] S. Merlet, J. Le Gouët, Q. Bodart et al., “Operating an atom interferometer beyond its linear range”, *Metrologia* **46** (feb, 2009) 87–94, [doi:10.1088/0026-1394/46/1/011](https://doi.org/10.1088/0026-1394/46/1/011).
- [13] J. Lautier, L. Volodimer, T. Hardin et al., “Hybridizing matter-wave and classical accelerometers”, *Applied Physics Letters* **105** (oct, 2014) 144102, [doi:10.1063/1.4897358](https://doi.org/10.1063/1.4897358).
- [14] G. Grynberg, A. Aspect, and C. Fabre, “Introduction to Quantum Optics: From the Semi-Classical Approach to Quantized Light”, *Contemporary Physics* (nov, 2011) 45–106, [doi:10.1080/00107514.2011.604134](https://doi.org/10.1080/00107514.2011.604134).
- [15] H. Metcalf and P. V. D. Straten, “Laser cooling and trapping of atoms”, *JOSA B* (2003).
- [16] Y. Wu, “Effective Raman theory for a three-level atom in the  $\Lambda$  configuration”, *Physical Review A - Atomic, Molecular, and Optical Physics* **54** (1996), no. 2, 1586–1592, [doi:10.1103/PhysRevA.54.1586](https://doi.org/10.1103/PhysRevA.54.1586).
- [17] P. Storey and C. Cohen-Tannoudji, “The Feynman path integral approach to atomic interferometry. A tutorial”, *Journal de Physique II* (1994).
- [18] K. Moler, D. Weiss, M. Kasevich et al., “Theoretical Analysis of Velocity-Selective Raman Transitions”, *Physical Review A* **45** (1992), no. 1, 342–348.
- [19] D. S. Weiss, B. C. Young, and S. Chu, “Precision measurement of  $\hbar/m$  Cs based on photon recoil using laser-cooled atoms and atomic interferometry”, *Applied Physics B Lasers and Optics* **59** (sep, 1994) 217–256, [doi:10.1007/BF01081393](https://doi.org/10.1007/BF01081393).
- [20] D. M. Brink and S. G. R., “Matrix Elements of Tensor Operators”, in *Angular Momentum*, pp. 56–60. 1968.

- [21] D. Steck, "Rubidium 87 D Line Data",
- [22] "IEEE Standard Specification Format Guide and Test Procedure for Linear, Single-Axis, Non-Gyroscopic Accelerometers", *IEEE Std 1293-1998 (R2008)* (2011) 1–249, doi:[10.1109/IEEESTD.2011.5960745](https://doi.org/10.1109/IEEESTD.2011.5960745).
- [23] A. Gauguet, B. Canuel, T. Lévèque et al., "Characterization and limits of a cold-atom Sagnac interferometer", *Physical Review A* **80** (dec, 2009) 063604, doi:[10.1103/PhysRevA.80.063604](https://doi.org/10.1103/PhysRevA.80.063604).
- [24] B. Dubetsky and M. Kasevich, "Atom interferometer as a selective sensor of rotation or gravity", *Physical Review A* **74** (aug, 2006) 023615, doi:[10.1103/PhysRevA.74.023615](https://doi.org/10.1103/PhysRevA.74.023615).
- [25] A. Keshet and W. Ketterle, "A Distributed GUI-based Computer Control System for Atomic Physics Experiments", doi:[10.1063/1.4773536](https://doi.org/10.1063/1.4773536), arXiv:[1208.2607](https://arxiv.org/abs/1208.2607).
- [26] K. Dieckmann, R. J. C. Spreeuw, M. Weidemüller et al., "Two-dimensional magneto-optical trap as a source of slow atoms", *Physical Review A* **58** (nov, 1998) 3891–3895, doi:[10.1103/PhysRevA.58.3891](https://doi.org/10.1103/PhysRevA.58.3891).
- [27] M. Walhout, J. Dalibard, S. L. Rolston et al., " $\sigma_{+-}\sigma_-$  Optical molasses in a longitudinal magnetic field", *Journal of the Optical Society of America B* **9** (nov, 1992) 1997, doi:[10.1364/JOSAB.9.001997](https://doi.org/10.1364/JOSAB.9.001997).
- [28] " $\mu$ Quans Laser System Specifications".
- [29] A. M. A. Steane, M. Chowdhury, and C. J. Foot, "Radiation force in the magneto-optical trap", *Journal of the Optical Society of America B* **9** (dec, 1992) 2142, doi:[10.1364/JOSAB.9.002142](https://doi.org/10.1364/JOSAB.9.002142).
- [30] M. Prentiss, E. L. Raab, D. E. Pritchard et al., "Atomic-density-dependent losses in an optical trap", *Optics Letters* **13** (jun, 1988) 452, doi:[10.1364/OL.13.000452](https://doi.org/10.1364/OL.13.000452).
- [31] J. Schoser, A. Batär, R. Löw et al., "Intense source of cold Rb atoms from a pure two-dimensional magneto-optical trap", *Physical Review A* **66** (aug, 2002) 023410, doi:[10.1103/PhysRevA.66.023410](https://doi.org/10.1103/PhysRevA.66.023410), arXiv:[0201034](https://arxiv.org/abs/0201034).
- [32] S.-i. Ohshima, T. Kurosu, T. Ikegami et al., "Cesium Atomic Fountain with Two-Dimensional Moving Molasses", *Japanese Journal of Applied Physics* **34** (sep, 1995) L1170–L1173, doi:[10.1143/JJAP.34.L1170](https://doi.org/10.1143/JJAP.34.L1170).

- [33] P. van der Straten, S.-Q. Shang, B. Sheehy et al., "Laser cooling at low intensity in a strong magnetic field", *Phys. Rev. A* **47** (1993), no. 5, 4160–4175, [doi:10.1103/PhysRevA.47.4160](https://doi.org/10.1103/PhysRevA.47.4160).
- [34] S. Chang, T. Y. Kwon, H. S. Lee et al., "Laser sub-Doppler cooling of atoms in an arbitrarily directed magnetic field", *Physical Review A - Atomic, Molecular, and Optical Physics* **66** (2002), no. 4, 23, [doi:10.1103/PhysRevA.66.043404](https://doi.org/10.1103/PhysRevA.66.043404).
- [35] D. J. Berkeland and M. G. Boshier, "Destabilization of dark states and optical spectroscopy in Zeeman-degenerate atomic systems", *Physical Review A* **65** (feb, 2002) 033413, [doi:10.1103/PhysRevA.65.033413](https://doi.org/10.1103/PhysRevA.65.033413).
- [36] V. Schkolnik, B. Leykauf, M. Hauth et al., "The effect of wavefront aberrations in atom interferometry", *Applied Physics B* **120** (aug, 2015) 311–316, [doi:10.1007/s00340-015-6138-5](https://doi.org/10.1007/s00340-015-6138-5).
- [37] G. Tackmann, P. Berg, C. Schubert et al., "Self-alignment of a compact large-area atomic Sagnac interferometer", *New Journal of Physics* **14** (jan, 2012) 015002, [doi:10.1088/1367-2630/14/1/015002](https://doi.org/10.1088/1367-2630/14/1/015002).
- [38] J. A. Nelder and R. Mead, "A Simplex Method for Function Minimization", *The Computer Journal* **7** (jan, 1965) 308–313, [doi:10.1093/comjnl/7.4.308](https://doi.org/10.1093/comjnl/7.4.308).
- [39] R. Zhang and F. Shi, "A Novel Algorithm for Fiber-Optic Alignment Automation", *IEEE Transactions on Advanced Packaging* **27** (feb, 2004) 173–178, [doi:10.1109/TADVP.2004.825434](https://doi.org/10.1109/TADVP.2004.825434).
- [40] R. Geiger, V. Ménoret, G. Stern et al., "Detecting inertial effects with airborne matter-wave interferometry.", *Nature communications* **2** (jan, 2011) 474, [doi:10.1038/ncomms1479](https://doi.org/10.1038/ncomms1479).
- [41] B. Barrett, L. Antoni-Micollier, L. Chichet et al., "Dual matter-wave inertial sensors in weightlessness", *Nature Communications* **7** (2016) [doi:10.1038/ncomms13786](https://doi.org/10.1038/ncomms13786), [arXiv:1609.03598](https://arxiv.org/abs/1609.03598).
- [42] S. Foote and D. Grindeland, "Model QA3000 Q-Flex accelerometer high performance test results", *IEEE Aerospace and Electronic Systems Magazine* **7** (jun, 1992) 59–67, [doi:10.1109/62.145120](https://doi.org/10.1109/62.145120).
- [43] R. W. P. Drever, J. L. Hall, F. V. Kowalski et al., "Laser phase and frequency stabilization using an optical resonator", *Applied Physics B Photophysics and Laser*

- Chemistry* **31** (jun, 1983) 97–105, doi:10.1007/BF00702605.
- [44] A. Gauguet, T. E. Mehlstäubler, T. Lévèque et al., “Off-resonant Raman transition impact in an atom interferometer”, *Physical Review A* **78** (oct, 2008) 043615, doi:10.1103/PhysRevA.78.043615, arXiv:0809.0149.
- [45] D. Allan, “Statistics of atomic frequency standards”, *Proceedings of the IEEE* **54** (1966), no. 2, 221–230, doi:10.1109/PROC.1966.4634.
- [46] E. Rocco, R. N. Palmer, T. Valenzuela et al., “Fluorescence detection at the atom shot noise limit for atom interferometry”, *New Journal of Physics* **16** (sep, 2014) 093046, doi:10.1088/1367-2630/16/9/093046.
- [47] P. Welch, “The use of fast Fourier transform for the estimation of power spectra: A method based on time averaging over short, modified periodograms”, *IEEE Transactions on Audio and Electroacoustics* **15** (jun, 1967) 70–73, doi:10.1109/TAU.1967.1161901.
- [48] G. Dick, “Local oscillator induced instabilities in trapped ion frequency standards”,
- [49] B. Canuel, “Étude d’un gyromètre à atomes froids”. PhD thesis, Université Paris Sud - Paris XI, 2007. doi:tel-00193288.
- [50] J. L. Gouët, T. Mehlstäubler, and J. Kim, “Limits to the sensitivity of a low noise compact atomic gravimeter”, *Applied Physics B* (2008) 1–30, arXiv:arXiv:0801.1270v1.
- [51] M. J. Vigué, A. Miffre, M. Büchner et al., “Phase noise due to vibrations in Mach-Zehnder atom interferometers”, *EPL (Europhysics Letters)* **75** (2006), no. 5, 688, doi:10.1209/epl/i2006-10177-6, arXiv:0604028.
- [52] A. Peters, K. Y. Chung, and S. Chu, “High-precision gravity measurements using atom interferometry”, *Metrologia* **38** (feb, 2001) 25–61, doi:10.1088/0026-1394/38/1/4.
- [53] J. R. Macdonald and W. J. Thompson, “Least-squares fitting when both variables contain errors: Pitfalls and possibilities”, *American Journal of Physics* **60** (jan, 1992) 66–73, doi:10.1119/1.17046.
- [54] E. Masry, “Flicker noise and the estimation of the Allan variance”, *IEEE Transactions on Information Theory* **37** (jul, 1991) 1173–1177,

- [doi:10.1109/18.86968](https://doi.org/10.1109/18.86968).
- [55] X. Cheng, "No Title". PhD thesis, Imperial College London, 2018.
  - [56] M. Schuler, "Die Störung von Pendel und Kreiselapparaten durch die Beschleunigung des Fahrzeuges", *Physikalische Zeitschrift* **24** (1923), no. 16.,
  - [57] T. Farah, C. Guerlin, A. Landragin et al., "Underground operation at best sensitivity of the mobile LNE-SYRTE Cold Atom Gravimeter",  
[doi:10.1134/S2075108714040051](https://doi.org/10.1134/S2075108714040051), [arXiv:1404.6722](https://arxiv.org/abs/1404.6722).
  - [58] P. Gillot, O. Francis, A. Landragin et al., "Stability comparison of two absolute gravimeters: Optical versus atomic interferometers", *Metrologia* **51** (2014), no. 5, L15–L17, [doi:10.1088/0026-1394/51/5/L15](https://doi.org/10.1088/0026-1394/51/5/L15), [arXiv:1406.5134](https://arxiv.org/abs/1406.5134).
  - [59] P. Cheiney, L. Fouché, S. Templier et al., "Navigation-Compatible Hybrid Quantum Accelerometer Using a Kalman Filter", *Physical Review Applied* **10** (sep, 2018) 034030, [doi:10.1103/PhysRevApplied.10.034030](https://doi.org/10.1103/PhysRevApplied.10.034030).
  - [60] V. Schkolnik, B. Leykauf, M. Hauth et al., "The effect of wavefront aberrations in atom interferometry", *Applied Physics B* **120** (aug, 2015) 311–316,  
[doi:10.1007/s00340-015-6138-5](https://doi.org/10.1007/s00340-015-6138-5).
  - [61] C. J. Borde, "Atomic clocks and inertial sensors", *Metrologia* **39** (2002), no. 5, 435–463, [doi:10.1088/0026-1394/39/5/5](https://doi.org/10.1088/0026-1394/39/5/5).
  - [62] J. Hogan, D. Johnson, and M. Kasevich, "Light-pulse atom interferometry", *arXiv preprint arXiv:0806.3261* (2008) 1–38, [arXiv:arXiv:0806.3261v1](https://arxiv.org/abs/arXiv:0806.3261v1).
  - [63] A. Lawrence, "Modern Inertial Technology". Mechanical Engineering Series. Springer New York, New York, NY, 1998.
  - [64] C. Salomon, J. Dalibard, W. D. Phillips et al., "Laser Cooling of Cesium Atoms Below 3  $\mu$ K", *Europhysics Letters (EPL)* **12** (aug, 1990) 683–688,  
[doi:10.1209/0295-5075/12/8/003](https://doi.org/10.1209/0295-5075/12/8/003).
  - [65] S. Y. Lan, P. C. Kuan, B. Estey et al., "Influence of the coriolis force in atom interferometry", *Physical Review Letters* **108** (2012), no. 9, 1–5,  
[doi:10.1103/PhysRevLett.108.090402](https://doi.org/10.1103/PhysRevLett.108.090402), [arXiv:1110.6910](https://arxiv.org/abs/1110.6910).
  - [66] S. Chu, L. Hollberg, J. Bjorkholm et al., "Three-Dimensional Viscous Confinement and Cooling of Atoms by Resonance Radiation Pressure", *Physical*

- Review Letters* **55** (1985), no. 1.,
- [67] T. H. Kim, S. H. Yim, K. M. Shim et al., “Spatial-contrast analysis in a cold-atom Sagnac interferometer with a single large Raman beam”, *Physical Review A* **95** (2017), no. 3, 1–6, [doi:10.1103/PhysRevA.95.033632](https://doi.org/10.1103/PhysRevA.95.033632).
- [68] J. M. Supplee, E. A. Whittaker, and W. Lenth, “Theoretical description of frequency modulation and wavelength modulation spectroscopy”, *Applied Optics* **33** (sep, 1994) 6294, [doi:10.1364/AO.33.006294](https://doi.org/10.1364/AO.33.006294).
- [69] T. Lévèque, L. Antoni-Micollier, B. Faure et al., “A laser setup for rubidium cooling dedicated to space applications”, *Applied Physics B* **116** (sep, 2014) 997–1004, [doi:10.1007/s00340-014-5788-z](https://doi.org/10.1007/s00340-014-5788-z), [arXiv:1309.2075](https://arxiv.org/abs/1309.2075).
- [70] J. Clauser, “Ultra-High Sensitivity Accelerometers And Gyroscopes Using Neutral Atom Matter-Wave Interferometry”, *Physica B+C* **151** (1988) 262–272.
- [71] E. L. Raab, M. Prentiss, A. Cable et al., “Trapping of Neutral Sodium Atoms with Radiation Pressure”, *Physical Review Letters* **59** (dec, 1987) 2631–2634, [doi:10.1103/PhysRevLett.59.2631](https://doi.org/10.1103/PhysRevLett.59.2631).
- [72] P. Dussarrat, M. Perrier, A. Imanaliev et al., “Two-Particle Four-Mode Interferometer for Atoms”, *Physical Review Letters* **119** (2017), no. 17, 1–8, [doi:10.1103/PhysRevLett.119.173202](https://doi.org/10.1103/PhysRevLett.119.173202), [arXiv:1707.01279](https://arxiv.org/abs/1707.01279).
- [73] A. Lawrence, “The Pendulous Accelerometer”, pp. 57–71. 1998.
- [74] V. Ménoret, R. Geiger, G. Stern et al., “Dual-wavelength laser source for onboard atom interferometry”, *Optics Letters* **36** (nov, 2011) 4128, [doi:10.1364/OL.36.004128](https://doi.org/10.1364/OL.36.004128).
- [75] A. Miffre, M. Jacquay, M. Büchner et al., “Atom interferometry”, [doi:10.1088/0031-8949/74/2/N01](https://doi.org/10.1088/0031-8949/74/2/N01), [arXiv:0605055](https://arxiv.org/abs/0605055).
- [76] C. J. Dedman, K. G. H. Baldwin, and M. Colla, “Fast switching of magnetic fields in a magneto-optic trap”, *Review of Scientific Instruments* **72** (2001), no. 11, 4055–4058, [doi:10.1063/1.1408935](https://doi.org/10.1063/1.1408935).
- [77] J. Lautier, M. Lours, and a. Landragin, “A compact micro-wave synthesizer for transportable cold-atom interferometers”, *Review of Scientific Instruments* **85** (2014), no. 6, [doi:10.1063/1.4884338](https://doi.org/10.1063/1.4884338), [arXiv:1406.2911](https://arxiv.org/abs/1406.2911).

- [78] A. L. Schawlow and C. H. Townes, "Infrared and Optical Masers", *Physical Review* **112** (dec, 1958) 1940–1949, [doi:10.1103/PhysRev.112.1940](https://doi.org/10.1103/PhysRev.112.1940).
- [79] S. Dimopoulos, P. Graham, J. Hogan et al., "Atomic gravitational wave interferometric sensor", *Physical Review D* **78** (dec, 2008) 122002, [doi:10.1103/PhysRevD.78.122002](https://doi.org/10.1103/PhysRevD.78.122002).
- [80] B. Leykauf, "The effect of wavefront aberrations in light-pulse atom interferometry", *Applied Physics B* (2014), no. May, 1–13, [doi:10.1007/s00340-015-6138-5](https://doi.org/10.1007/s00340-015-6138-5), [arXiv:arXiv:1411.7914v1](https://arxiv.org/abs/arXiv:1411.7914v1).
- [81] A. Sugarbaker and S. Dickerson, "Enhanced atom interferometer readout through the application of phase shear", *Physical review ...* **94** 305 (2013) [arXiv:arXiv:1305.3298v1](https://arxiv.org/abs/arXiv:1305.3298v1).
- [82] T. Müller, T. Wendrich, M. Gilowski et al., "Versatile compact atomic source for high-resolution dual atom interferometry", *Physical Review A* **76** (dec, 2007) 063611, [doi:10.1103/PhysRevA.76.063611](https://doi.org/10.1103/PhysRevA.76.063611).
- [83] M. Haw, N. Evetts, W. Gunton et al., "Magneto-optical trap loading rate dependence on trap depth and vapor density", *Journal of the Optical Society of America B* **29** (feb, 2012) 475, [doi:10.1364/JOSAB.29.000475](https://doi.org/10.1364/JOSAB.29.000475).
- [84] J. Hogan, "Towards precision tests of general relativity using an atom interferometer",.
- [85] K. Wen, C. K. Seow, and S. Y. Tan, "Inertial navigation system positioning error analysis and Cramér-Rao lower bound", in *2016 IEEE/ION Position, Location and Navigation Symposium (PLANS)*, pp. 213–218. IEEE, apr, 2016. [doi:10.1109/PLANS.2016.7479704](https://doi.org/10.1109/PLANS.2016.7479704).
- [86] C. Roos, P. Cren, J. Dalibard et al., "A Source of Cold Atoms for a Continuously Loaded Magnetic Guide", *Physica Scripta* **T105** (2003), no. 1, 19, [doi:10.1238/Physica.Topical.105a00019](https://doi.org/10.1238/Physica.Topical.105a00019).
- [87] R. Nyman, G. Varoquaux, F. Lienhart et al., "I.C.E.: a transportable atomic inertial sensor for test in microgravity", *Applied Physics B* **84** (aug, 2006) 673–681, [doi:10.1007/s00340-006-2395-7](https://doi.org/10.1007/s00340-006-2395-7).
- [88] M. Pappa, P. C. Condylis, G. O. Konstantinidis et al., "Ultra-sensitive atom imaging for matter-wave optics", *New Journal of Physics* **13** (nov, 2011) 115012,

- [doi:10.1088/1367-2630/13/11/115012](https://doi.org/10.1088/1367-2630/13/11/115012).
- [89] M. Kasevich, "Atom Interferometry in an atomic fountain", 1992.
  - [90] P. R Berman, "Atom Interferometry". 1997.
  - [91] M. Kasevich, D. S. Weiss, E. Riis et al., "Atomic velocity selection using stimulated Raman transitions", *Physical Review Letters* **66** (may, 1991) 2297–2300, [doi:10.1103/PhysRevLett.66.2297](https://doi.org/10.1103/PhysRevLett.66.2297).
  - [92] A. M. Marino and C. R. Stroud, "Phase-locked laser system for use in atomic coherence experiments.", *The Review of scientific instruments* **79** (jan, 2008) 013104, [doi:10.1063/1.2823330](https://doi.org/10.1063/1.2823330).
  - [93] P. Cheinet, B. Canuel, F. Pereira Dos Santos et al., "Measurement of the sensitivity function in a time-domain atomic interferometer", *IEEE Transactions on Instrumentation and Measurement* **57** (jun, 2008) 1141–1148, [doi:10.1109/TIM.2007.915148](https://doi.org/10.1109/TIM.2007.915148), [arXiv:0510197](https://arxiv.org/abs/0510197).
  - [94] R. M. Howard, "Principles of Random Signal Analysis and Low Noise Design". 2002.
  - [95] K. Berg-Sørensen, Y. Castin, E. Bonderup et al., "Momentum Diffusion of Atoms Moving in Laser Fields", *Journal of Physics B: Atomic, Molecular and Optical Physics* **25** (1992), no. 20, 4195–4215, [doi:10.1088/0953-4075/25/20/016](https://doi.org/10.1088/0953-4075/25/20/016).
  - [96] N. Wiebe and C. Granade, "Efficient Bayesian Phase Estimation", *Physical Review Letters* **117** (2016), no. 1, 1–12, [doi:10.1103/PhysRevLett.117.010503](https://doi.org/10.1103/PhysRevLett.117.010503), [arXiv:1508.00869](https://arxiv.org/abs/1508.00869).
  - [97] K. Molmer, "Atomic momentum diffusion in a  $\sigma^+ - \sigma^-$  laser configuration: influence of an internal sublevel structure", *Journal of Physics B: Atomic, Molecular and Optical Physics* **23** (1990), no. 22, 4101–4110, [doi:10.1088/0953-4075/23/22/012](https://doi.org/10.1088/0953-4075/23/22/012).
  - [98] R. Han, H. K. Ng, and B.-G. Englert, "Raman transitions without adiabatic elimination: A simple and accurate treatment", *Journal of Modern Optics* **60** (sep, 2012) 17, [arXiv:1209.6569](https://arxiv.org/abs/1209.6569).
  - [99] U. Schunemann, H. Engler, R. Grimm et al., "Simple scheme for tunable frequency offset locking of two lasers", *Review of Scientific Instruments* **70** (1999),

no. 1, 242, [doi:10.1063/1.1149573](https://doi.org/10.1063/1.1149573).

- [100] B. Barrett, P. a. Gominet, E. Cantin et al., “Mobile and remote inertial sensing with atom interferometers”, *Proceedings of the International School of Physics "Enrico Fermi"*, Vol 188 (2013) [doi:10.3254/978-1-61499-448-0-493](https://doi.org/10.3254/978-1-61499-448-0-493), [arXiv:1311.7033](https://arxiv.org/abs/1311.7033).
- [101] K. Bongs, R. Launay, and M. Kasevich, “High-order inertial phase shifts for time-domain atom interferometers”, *Applied Physics B* **84** (aug, 2006) 599–602, [doi:10.1007/s00340-006-2397-5](https://doi.org/10.1007/s00340-006-2397-5).
- [102] J. Dalibard and C. Cohen-Tannoudji, “Laser cooling below the Doppler limit by polarization gradients: simple theoretical models”, *Journal of the Optical Society of America B* **6** (nov, 1989) 2023, [doi:10.1364/JOSAB.6.002023](https://doi.org/10.1364/JOSAB.6.002023).

# Acronyms

**ADC** Analogue-to-Digital Converter

**AOM** Acousto-optic Modulator

**CCM** Centre for Cold Matter

**DAC** Digital-to-Analogue Converter

**DAQ** Data Acquisition

**DDS** Direct Digital Synthesiser

**ECDL** External-Cavity Diode Laser

**EDFA** Erbium-Doped Fibre Amplifier

**EOM** Electro-optic Modulator

**FPGA** Field-Programmable Gate Array

**GNSS** Global Navigation Satellite System

**HWP** Half-wave Plate

**MOT** Magneto-optical Trap

**NA** Numerical Aperture

**NEG** Non-evaporative Getter

**NEP** noise-equivalent power

**PBS** Polarising beam-splitter

**PLL** Phase-Locked Loop

**PM** Polarisation-Maintaining

**PPLN** Periodically-Poled Lithium Niobate

**QWP** Quarter-wave Plate

**SPI** Serial Programming Interface

**UHV** Ultra-high Vacuum

**VCA** Voltage-Controlled Attenuator

**VCO** Voltage-Controlled Oscillator

**<sup>87</sup>Rb** Rubidium-87

**ADC** Analogue-to-Digital Converter

**AOM** Acousto-optic Modulator

**CCM** Centre for Cold Matter

**DAC** Digital-to-Analogue Converter

**DAQ** Data Acquisition

**DDS** Direct Digital Synthesiser

**ECDL** External-Cavity Diode Laser

**EDFA** Erbium-Doped Fibre Amplifier

**EOM** Electro-optic Modulator

**FPGA** Field-Programmable Gate Array

**GNSS** Global Navigation Satellite System

**HWP** Half-wave Plate

**MOT** Magneto-optical Trap

**NA** Numerical Aperture

**NEG** Non-evaporative Getter

**NEP** noise-equivalent power

**PBS** Polarising beam-splitter

**PLL** Phase-Locked Loop

**PM** Polarisation-Maintaining

**PPLN** Periodically-Poled Lithium Niobate

**QWP** Quarter-wave Plate

**SPI** Serial Programming Interface

**UHV** Ultra-high Vacuum

**VCA** Voltage-Controlled Attenuator

**VCO** Voltage-Controlled Oscillator

**<sup>87</sup>Rb** Rubidium-87